UC Riverside

UC Riverside Electronic Theses and Dissertations

Title

Electronic Properties of Suspended Few-Layer Graphene Membranes

Permalink

https://escholarship.org/uc/item/6hk8j9fd

Author

Myhro, Kevin Scott

Publication Date

2017

Peer reviewed|Thesis/dissertation

UNIVERSITY OF CALIFORNIA
RIVERSIDE

Electronic Properties of Suspended Few-Layer Graphene Membranes

A Dissertation submitted in partial satisfaction
of the requirements for the degree of

Doctor of Philosophy

in

Physics

by

Kevin Scott Myhro

September 2017

Dissertation Committee:
Dr. Chun Ning (Jeanie) Lau, Chairperson
Dr. Vivek Aji
Dr. Nathaniel Gabor

The Dissertation of Kevin Scott Myhro is approved:

_____

_____

_____
Committee Chairperson

University of California, Riverside

Acknowledgments

The work presented in this thesis is the cumulation of six years of experimental condensed matter research in Professor Chun Ning (Jeanie) Lau's research group at the University of California, Riverside (UCR). In that time, I have developed from a graduate student to a Ph.D. candidate and independent researcher. I received invaluable help from various people whom I would like to acknowledge below.

Firstly, I acknowledge my advisor Prof. Jeanie Lau, without whom, my entire Ph.D. would not have been possible. I first met Jeanie in the Summer of 2010, and joined her group as an undergraduate researcher. After I graduated from UCR with a BS in Physics with highest honors, I returned to UCR to join the Physics Ph.D. program because I was impressed with its Physics department and Jeanie Lau's proven record as a well-established Physicist. Jeanie, for instance, is the only professor at UCR to receive the Presidential Early Career Award for Scientists and Engineers (PECASE), which was presented by President Obama in 2008. In the seven years that I have known Jeanie, she has been immensely helpful and instrumental in giving me research advice, direction, and troubleshooting of both experiments and data analysis. Jeanie has given me countless hours of her time to help me grow as a physicist and contribute to our research group, the condensed matter physics community, and in turn, the entire world. Of the many ways Jeanie has been instrumental in my research, she has helped me by brainstorming research projects and funding my research, both at UCR and at the National High Magnetic Field Laboratory (NHMFL). Furthermore, Jeanie went above and beyond the typical expectations of a research advisor by giving me the opportunity to present my

research in oral and poster form at various science conferences in places like San Francisco, CA, Long Beach, CA, Denver, CO, Panama City Beach, FL, Baltimore, MD and Chemnitz, Germany.

The second most important person for me to acknowledge and thank for my success in the UCR Physics Ph.D. program is Dr. Yongjin Lee. Yongjin acted as a mentor to me, and I worked with him for a several years on similar few-layer graphene projects. Yongjin taught me electron beam lithography from the ground up and how to use various tools in the cleanroom. His advice was extremely helpful in several areas: sample preparation, device fabrication, device measurement, and data analysis. Yongjin taught me all the ins and outs of the lab and how to turn a chunk of graphite into a working graphene field effect transistor (FET). I travelled to the NHMFL in Florida with Yongjin several times, and he was a pleasure to work with, and I will always be grateful for his help.

Dr. Jairo Velasco Jr. was also very helpful in my Ph.D. Jairo Velasco Jr., along with Jeanie Lau and Gang Liu developed a "doubly-suspended" graphene-based FET (Patent No.: US 7,948,042 B2, May 24, 2011), which was later modified by Yongjin Lee and myself, and later became a vital component of my research. Furthermore, Jairo and I had several long discussions about physics, the quantum hall effect, electrons, and X-Men in our old shared office in Pierce Hall. Jairo was both a friend and a mentor to me, and my experience at UCR would have been completely different without him.

I wish to acknowledge the entire cleanroom staff at the Center for Nanoscale Science & Engineering (CNSE) at UCR, including the cleanroom manager Dr. Mark

Heiden, and staff members Dr. Dong Yan, Dr. Dexter Humphrey. Dexter, in particular, was extremely helpful to me, and was always available to troubleshoot issues with the electron beam evaporator or cleanroom problems in general. He also gave the cleanroom a lively atmosphere and I enjoyed talking about American football with him while waiting for the electron beam evaporator vacuum chamber to pump down.

In addition to those previously mentioned, I also acknowledge the following current and fromer scientists and staff from the NHMFL: Dr. Dmitry Smirnov, Dr. Jean-Marie Poumirol, Dr. Jonathan Ludwig, Dr. David Earl Graf, Tim Murphy, Jonathan Billings, Glover Jones, and Bobby Joe Pullum. I am appreciative to have had the opportunity to collaborate with Dmitry Smirnov on different projects, and his assistance operating the cryogenic magnets was paramount to my visits to the NFHML. Another collaborator whom I acknowledge is Dr. Frank Koppens from the The Institute of Photonic Sciences (ICFO) in Castelldefels, Spain.

I also acknowledge my family for their unwavering support, both emotionally and financially, throughout my Ph.D. I thank my parents, Darrall and Michelle Myhro, for always encouraging me to stay in school and put my nose to the grindstone. I acknowledge my brother David for his interesting thought experiments and physics questions which always kept me on my toes. I also acknowledge my grandfather Samuel Boucher and my late grandmother Nancy Boucher for always encouraging me to excel in school.

I acknowledge current and former UCR faculty and staff members, including Prof. Marc Bockrath, Prof. Owen Long, Prof. Jing Shi, Prof. Umar Mohideen, Prof. Bob

Clare, Derek Beving, Jhon Gonzalez, Sonia Godinez, Mike Fournier, Will Sundquist, Herb Kuehne, Bob Ree and Jack Reed.

Finally, I would like to thank current and former Lau research group members, including: Dr. Jairo Velasco Jr., Dr. Lei Jing, Dr. Fenglin Wang, Dr. Jhao-Wun Huang, Dr. Yanmeng Shi, Dr. Nathaniel Gillgren, Dr. Ruoyu Chen, Petr Stepanov, Shi Che, Son Tran, Yulu Liu, Dmitry Shcherbakov, David Tran, Kevin Thilahar, Mason Gray, Kevin Bleich, Tim Espiritu, and Greyson Voigt.

Dedicated to my parents and my brother

ABSTRACT OF THE DISSERTATION

Electronic Properties of Suspended Few-Layer Graphene Membranes

by

Kevin Scott Myhro

Doctor of Philosophy, Graduate Program in Physics
University of California, Riverside, September 2017
Dr. Chun Ning (Jeanie) Lau, Chairperson

Graphene, the two-dimensional (2D) honeycomb lattice of sp^2-hybrized carbon atoms, has emerged as a "wonder" material with unique properties, such as its linear energy dispersion with massless Dirac fermions, so-called half-integer quantum Hall (QH) effect, unparalleled tensile strength, and high optical transparency and thermal conductivity. Its few-layer counterparts have similar mechanical but remarkably different electrical properties, including layer- and stacking-dependent band structures, massive charge carriers, and energy gaps that may arise from single particle effect as well as electronic interactions.

This dissertation reports my six year study of dual-gated suspended few-layer graphene (FLG) field effect transistor (FET) devices. In particular, we focus on their electronic transport properties at low temperature as a function of out-of-plane electric field $E_\perp$ and interlayer potential $U_\perp$, charge carrier density n, temperature T, and out-of-

plane ($B_\perp$) and parallel ($B_\parallel$) magnetic fields. A number of broken symmetry states in the absence and presence of external fields are observed in rhombohedral-stacked bilayer- (BLG), trilayer- (r-TLG), and tetralayer graphene (r-4LG). We also study the morphological deformation of suspended graphene membranes under electrostatic and thermal manipulation, which is relevant for analyzing low temperature transport data.

In particular, in BLG, r-TLG and r-4LG, we observe intrinsic insulating states in the absence of external fields, with energy gaps of 2, ~40, and ~80 meV, respectively. We attribute this increasing gap size with number of layers N to enhanced electronic-interactions near the charge neutrality point, due to the layer-dependent energy dispersions k^N in r-FLG, which give rise to increasingly diverging density of states and interaction strength with increasing N, at least up to four layers. Our observations of the spontaneous insulating state in r-FLG are consistent with a layer antiferromagnetic state with broken time reversal symmetry, where the top and bottom layers are oppositely spin polarized.

Table of Contents

List of Figures

List of Tables

Chapter 1: Introduction

1.1   Background

Physics is the fundamental science and it seeks to explain both the visible and the invisible using the most simplified, logical approaches, with the least number of assumptions and approximations. Philip Russel Wallace did just this when he employed the "tight-binding" approximation to solve the band structure of single layer graphene (SLG), the atomically-thin carbon allotrope of graphite, in 1947[1]. This model was effective in predicting the properties of a single layer of graphene, however, it was unknown at the time whether such a single atomic layer of carbon would be stable. Multi-walled carbon nanotubes (MWCNTs), which are concentric carbon fullerene tubes, were discovered in 1991[2], and single-walled carbon nanotubes (SWCNTs), or a rolled-up membrane of a single layer of graphene, were discovered in 1993[3]. It was more than half a century after Wallace's band structure calculation that flat sheets of SLG were finally isolated by Andre Geim and Konstantin Novoselov from Manchester University using the scotch tape exfoliation technique in 2004[4]. The discovery of graphene has led to a gold rush in the research of its properties and applications, resulting in tens of thousands of publications, and has sparked intense interest in graphene-based heterostructures and many other two-dimensional (2D) materials as well[5,6].
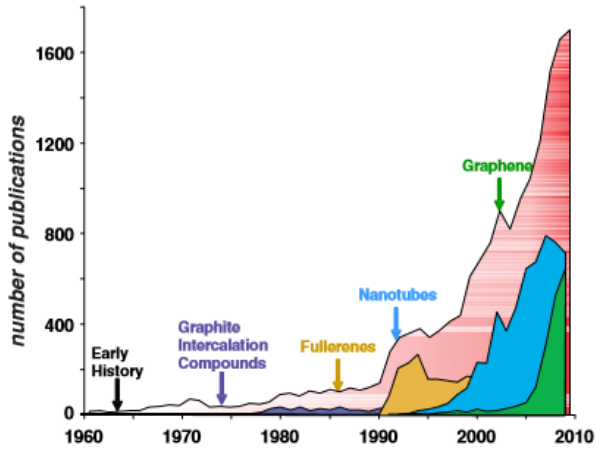
Figure 1.1. Frequency of sp² carbon publications: Number of publications on sp^2 carbon per year plotted in a 50-year interval. Image taken from ref. 6.

While SLG has been extensively studied[6-9], its multilayer counterparts, including bilayer graphene (BLG), trilayer graphene (TLG) and tetralayer graphene (4LG), have been much less explored. As it will be discussed later, multiple layers of graphene constitute unique 2D materials, different from SLG. One of the largest and most striking differences, is that while SLG is a gapless semi-metal[1,4,7,8], it has been found that BLG[8,10-12], TLG[13-15] and 4LG[16,17] exhibit spontaneous insulating states and gate-tunable band gaps with non-relativistic charge carriers. Therefore, the single element of carbon can comprise many different 2D material platforms with distinct electronic, thermal and optical properties, which is the motivation of this dissertation.

1.2   Basic properties of graphene

Graphene is a single atomic layer of carbon in a honeycomb, or hexagonal lattice. Carbon, the sixth element, is one of the most abundant elements on Earth. It exists in

stable solid allotropes as diamond and graphite and is the primary element in coal. While diamond and coal have been used for thousands of years, graphite's application is much more recent, as the first graphite pencil was invented the sixteenth century. Though graphite can be considered as a stack of graphene layers held together by van der Waals' forces, the isolation of a single atomic layer of graphene has only been achieved in 2004, and its applications are still unfolding.

Carbon exists in three dimensions (3D) as diamond and graphite, in two dimensions (2D) as graphene sheets, in one dimension (1D) as nanotubes and zero dimensions (0D) as buckeyballs. In its 2D form, graphene has been touted as a wonder material due to its unique electrical, magnetic, optical and mechanical properties[19-21]. As shown below in section 2.2.3, graphene has a linear band structure, which gives rise to relativistic charge carriers with a Fermi velocity of 10^8 m/s, which is 0.3% the speed of light[21]. Graphene is the strongest material at its length scales, with an incredible tensile strength that is 325 times stronger than steel[18]. Furthermore, graphene has an exceptional electronic mobility which can be over 100 times larger than silicon's mobility at room temperature[18]. Graphene conducts heat ten times better than copper[22], and it absorbs only $\pi\alpha = 2.3\%$ of light[23], where α is the fine structure constant, making it an unusual transparent conductor that is important for applications such as touch screens and solar cells.

1.3 Thesis outline and references

This thesis is organized as follows. Chapter two discusses the background of graphene, describes the layer-dependent properties of few-layer graphene, and derives the band structure of SLG, BLG, Bernal-stacked TLG (B-TLG), and rhombohedral-stacked multilayers of graphene based off of tight binding calculations. Chapter three describes in detail the innovative multi-level electron beam lithography fabrication techniques used to create high quality prototype suspended few-layer graphene field effect transistors. Chapter four discusses the morphological deformation of suspended graphene membranes through electrostatic and thermal manipulation via *in situ* scanning electron microscopy. Chapter five motivates the use of suspended graphene and top gates, and presents the dual-gated electronic transport data of BLG and rhombohedral-stacked trilayer graphene (r-TLG), and discusses their spontaneous and induced insulating states. Chapter six presents tunable spontaneous insulating states in suspended rhombohedral-stacked tetralayer graphene (r-4LG). Chapter seven gives a brief background on the quantum Hall effect in few-layer graphene (FLG) and discusses quantum Hall ferromagnetism in suspended r-TLG. Finally, chapter eight concludes the thesis and Appendix A provides some extra statistics on transport data and other supplementary information.

References

1. Wallace, P. R. The Band Theory of Graphite. *Phys. Rev.*, **71**, 622-634, (1947).

2. Iijima, S. Helical microtubes of graphitic carbon. *Nature*, **354**, 56-58 (1991).

3. Iijima, S., and Ichihashi, T. Single-shell carbon nanotubes of 1-nm diameter. Nature, 363, 603-605 (1993).

4. K. S. Novoselov, A. K. Geim, S. V. Morozov, D. Jiang, Y. Zhang, S. V. Dubonos, I. V. Grigorieva, and A. A. Firsov. Electric field effect in atomically thin carbon films. *Science*, **306**, 666-669 (2004).

5. A. K. Geim and K. S. Novoselov. The rise of graphene. *Nature*, **6**, 183-191 (2007).

6. M. S. Dresselhaus. Fifty years in studying carbon-based materials. *Phys. Scr.* **T146**, 014002 (2012).

7. Novoselov, K. S., Geim, A. K., Morozov, S. V., Jiang, D., Katsnelson, M. I., Grigorieva, I. V., Dubonos, S. V., and Firsov, A. A. Two-dimensional gas of massless Dirac fermions in graphene. *Nature*, **438**, 197-200 (2005).

8. Castro Neto, A. H., Guinea, F., Peres, N. M. R., Novoselov, K. S., and Geim, A. K. The electronic properties of graphene. *Rev. Mod. Phys.*, **81**, 109-163 (2009).

9. Das Sarma, S., Adam, S., Hwang, E. H., and Rossi, E. Electronic transport in two-dimensional graphene. *Rev. Mod. Phys.*, **83**, 407-470 (2011).

10. Zhang, Y., Tang, T.-T., Girit, C., Hao, Z., Martin, M. C., Zettl, A., Crommie, M. F., Ron Shen, Y., and Wang, F. Direct observation of a widely tunable bandgap in bilayer graphene. *Nature*, **459**, 820-823 (2009).

11. Bao, W., Velasco, J. Jr., Zhang, F., Jing, L., Standley, B. Smirnov, D., Bockrath, M., MacDonald, A. H., and Lau, C. N. Evidence for a spontaneous gapped state in ultraclean bilayer graphene. *Proc. Natl. Acad. Sci.*, **109** (27), 10802-10805 (2012).

12. Velasco, J. Jr., Jing, L., Bao, W., Kratz, P., Aji, V., Bockrath, M., Lau, C. N., Varma, C., Stillwell, R., Smirnov, D., Zhang, F., Jung, J., and MacDonald, A. H. Transport spectroscopy of symmetry-broken insulating states in bilayer graphene. *Nat. Nanotechnol.* **7**, 156-160 (2012).

13. Zhang, F., Sahu, B., Min, H., and MacDonald, A. H. Band structure of ABC-stacked graphene trilayers. *Phys. Rev. B*, **82**, 035409 (2010).

14. Bao, W., Jing, L., Velasco, J. Jr., Lee, Y., Liu, G., Tran, D., Standley, B., Aykol, M., Cronin, S. B., Smirnov, D., Koshino, M., McCann, E., Bockrath, M. and Lau, C. N. Stacking-dependent band gap and quantum transport in trilayer graphene. *Nature Phys.* **7**, 948-952 (2011).

15. Lee, Y., Tran, D., Myhro, K., Velasco, J. Jr., Gillgren, N., Lau, C. N., Barlas, Y., Poumirol, J. M., Smirnov, D., and Guinea, F. Competition between spontaneous symmetry breaking and single-particle gaps in trilayer graphene. *Nat. Commun.*, **5**, 5656 (2014).

16. Aoki, M. and Amawashi, H. Dependence of band structures on stacking and field in layered graphene. *Solid State Commun.* **142** (3), 123-127 (2007).

17. Grushina, A. L., Ki, D.-K., Koshino, M., Nicolet, A. A. L., Faugeras, C., McCann, E., Potemski, M., and Morpurgo, A. F. Insulating state in tetralayers reveals an even-odd interaction effect in multilayer graphene. *Nat. Commun.*, **6**, 6419 (2015).

18. "About Diamonds" *HRD Antwerp*, 2017, http://www.hrdantwerp.com/en/about-diamonds.

19. De la Fuenta, J. "Graphene Applications & Uses." *Graphenea*, 2017, https://www.graphenea.com/pages/graphene-properties#.WYkevojyvIV.

20. Kobie, N. "What are carbon nanotubes?" *Alphr*, 2016, http://www.alphr.com/science/1003177/what-are-carbon-nanotubes.

21. "In Situ Real-time Atomic Scale Nanostructural Synthesis, Characterization and Modeling." *Arizona State University*, 2007, https://www.asu.edu/clas/csss/NUE/gallery.html.

22. A. K. Geim and K. S. Novoselov. The rise of graphene. *Nature*, **6**, 183-191 (2007).

23. Castro Neto, A. H., Guinea, F., Peres, N. M. R., Novoselov, K. S., and Geim, A. K. The electronic properties of graphene. *Rev. Mod. Phys.*, **81**, 109-163 (2009).

24. Das Sarma, S., Adam, S., Hwang, E. H., and Rossi, E. Electronic transport in two-dimensional graphene. *Rev. Mod. Phys.*, **83**, 407-470 (2011).

25. Balandin, A. A., Ghosh, S., Bao, W., Calizo, I., Teweldebrhan, D., Miao, F., and Lau, C. N. Superior thermal conductivity of single-layer graphene. *Nano Lett*. **8** (3), 902-907 (2008).

26. Nair, R. R., Blake, P., Grigorenko, A. N., Novoselov, K. S., Booth, T. J., Stauber, T., Peres, N. M. R., and Geim, A. K. Fine structure constant defines visual transparency of graphene. *Science*, **320** (5881), 1308 (2008).

Chapter 2: Theoretical Background

2.1   Introduction

Electronic band structure is one of the most important concepts in solid state physics, as it determines, to a large extent, a material's electrical, optical and magnetic properties. There are many approaches to calculate the band structure of a crystal, such as the Cellular (Wigner-Seitz) method, Green's Function (KKR) method, Augmented Plane Wave (APW) method, Orthoganol Plane Wave (OPW) method and the pseudopotential method, for instance[1]. In this chapter, we will use the tight binding (TB) approximation to calculate the electronic band structure of single layer graphene (SLG), bilayer graphene (BLG), Bernal-stacked trilayer graphene (B-TLG) and rhombohedral-stacked multilayers of graphene.

2.2   The tight binding approximation

In a crystal, atoms are tightly-packed with overlapping atomic wave functions. In the TB approximation, the atomic wavefunctions overlap significantly so that the orbitals are significantly modified from those of isolated atoms, yet, the overlaps are not so extreme as to destroy the atomic description altogether.

The TB method assumes that single electrons are tightly bound to the atoms, hence the name tight binding, and considers all other electrons that form a fixed background, or mean-field, effectively neglecting the correlations between electrons. Although the TB model does not account for electron-electron interactions, it is a

reasonable starting point for calculating band structures of many crystals. The TB method requires two quantum numbers: the Bloch vector $\vec{k}$ and the band index n. Bloch wavefunctions $\Phi_{nk}(\vec{r})$ are the product of a plane wave and some function $\varphi(\vec{r})$ with the periodicity of the Bravais Lattice, as follows:

$$\Phi_{nk}(\vec{r}) = e^{i\vec{k}\cdot\vec{r}}\varphi(\vec{r}) \tag{2.1}$$

Since $\Phi_{nk}(\vec{r})$ is periodic for all Bravais Lattice vectors $\vec{R}$,

$$\Phi_{nk}(\vec{r} + \vec{R}) = \Phi_{nk}(\vec{r}) \tag{2.2}$$

If there are N unit cells in a crystal, then the atomic wave functions at given $\vec{k}$ and $\vec{r}$ can be represented by a linear combination of Bloch wavefunctions:

$$\Phi_j(\vec{k},\vec{r}) = \frac{1}{\sqrt{N}}\sum_{i=1}^{N} e^{i\vec{k}\cdot\vec{R}_{ji}}\,\varphi_j(\vec{r} - \vec{R}_{ji}) \tag{2.3}$$

where i is the summation index, $\Phi_j(\vec{k},\vec{r})$ represents the wave function of the jth unit cell, and $\vec{R}_{ji}$ is the position vector from the ith unit cell to the jth unit cell. The electronic wavefunction will therefore be a linear combination of n Bloch wavefunctions,

$$\Psi_j(\vec{k},\vec{r}) = \sum_{l=1}^{n} a_{jl}\Phi_l(\vec{k},\vec{r}) \tag{2.4}$$

where a_{jl} is the expansion coefficient. The wavefunctions $\Psi_j(\vec{k},\vec{r})$ are constructed as eigenstates of the single electron Hamiltonian, such that the energy of the jth unit cell is given by:

$$E_j(k) = \frac{<\Psi_j|H|\Psi_j>}{<\Psi_j|\Psi_j>} = \frac{\sum_{il}^{n} a_{ji}^* a_{jl}<\Phi_i|H|\Phi_l>}{\sum_{il}^{n} a_{ji}^* a_{jl}<\Phi_i|\Phi_l>} = \frac{\sum_{il}^{n} a_{ji}^* a_{jl}H_{il}}{\sum_{il}^{n} a_{ji}^* a_{jl}S_{il}} \tag{2.5}$$

where H_{il} are the transfer integral matrix elements and S_{il} is the overlap matrix elements, and they are defined as:

$$H_{il} = \frac{\langle \Phi_i|H|\Phi_l \rangle}{<\Phi_i|\Phi_l>} \tag{2.6}$$

$$S_{il} = \frac{\langle \Phi_i|S|\Phi_l \rangle}{<\Phi_i|\Phi_l>} \tag{2.7}$$

Thus, the energy band $E_j(k)$ is determined by the secular equation:

$$\det(H - E_j S) = 0 \tag{2.8}$$

where *det* is the determinant of the matrix.

2.2.1 Single layer graphene

Single layer graphene (SLG) consists of a single layer honeycomb lattice of sp²-hybridized carbon atoms. Its Bravais lattice is a triangular lattice, with two atoms per unit cell (figure 2.1). We define the primitive lattice vectors $\vec{a}_1$ and $\vec{a}_2$ as:

$$\vec{a}_1 = \left(\frac{a}{2}, \frac{\sqrt{3}a}{2}\right), \quad \vec{a}_2 = \left(\frac{a}{2}, -\frac{\sqrt{3}a}{2}\right) \tag{2.9}$$

where a = 2.46 Å is the distance between the unit cells and $a/\sqrt{3}$ is the distance between nearest neighboring carbon atoms. From the requirement $\vec{a}_i \bullet \vec{b}_j = 2\delta_{ij}$, the reciprocal lattice vectors are simply:

$$\vec{b}_1 = \left(\frac{2\pi}{a}, \frac{2\pi}{\sqrt{3}a}\right), \quad \vec{b}_2 = \left(\frac{2\pi}{a}, -\frac{2\pi}{\sqrt{3}a}\right) \tag{2.10}$$

The reciprocal lattice vectors define the Bravais lattice in the momentum space. The primitive translation vectors, reciprocal lattice vectors and the first Brillouin zone are shown in figure 2.1.
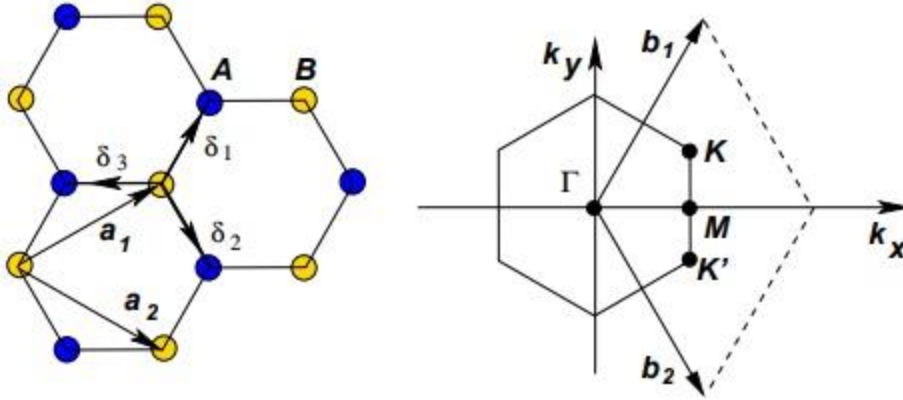
Figure 2.1. Crystal lattice structure of graphene: (a) Crystal structure diagram of graphene's honeycomb lattice with A and B triangular sub-lattices. Vectors $\vec{a}_1$ and $\vec{a}_2$ are the primitive translation vectors, and vectors $\vec{\delta}_1$, $\vec{\delta}_2$ and $\vec{\delta}_3$ point to the nearest neighbors. (b) The first Brillouin zone for SLG in (k_x, k_y) momentum space, with reciprocal lattice vectors $\vec{b}_1$ and $\vec{b}_2$. Image taken from ref. 2.

Using the secular equation given in equation 2.8, we obtain

$$\begin{vmatrix} H_{AA}(k) - E(k)S_{AA}(k) & H_{BA}(k) - E(k)S_{BA}(k) \\ H_{AB}^*(k) - E(k)S_{AB}^* & H_{BB}(k) - E(k)S_{BB}(k) \end{vmatrix} = 0 \qquad (2.11)$$

We will make the reasonable assumption that $H_{AA} = H_{BB}$ and $S_{AA} = S_{BB}$ because the two sub-lattices are identical. We need to simply determine these matrix elements to solve the energy $E(k)$ of conduction electrons in the graphene lattice.

The diagonal terms H_{AA} and S_{AA} of the determinant in equation 2.11 will be calculated separately from the off-diagonal terms. Plugging in equation 2.3 into 2.6, the first matrix element H_{AA} of the transfer integral matrix is:

$$H_{AA} = \frac{1}{N} \sum_{i=1}^{N} \sum_{j=1}^{N} e^{i\vec{k}\cdot(\vec{R}_{Aj} - \vec{R}_{Ai})} \langle \varphi_A(\vec{r} - \vec{R}_{Ai}) | H | \varphi_A(\vec{r} - \vec{R}_{Ai}) \rangle \qquad (2.12)$$

which reduces to:

$$H_{AA} = \frac{1}{N} \sum_{i=1}^{N} \langle \varphi_A(\vec{r} - \vec{R}_{Ai}) | H | \varphi_A(\vec{r} - \vec{R}_{Ai}) \rangle \qquad (2.13)$$

10

where, by the rules of eigenvalues,

$$\varepsilon = \langle \varphi_A(\vec{r} - \vec{R}_{Ai}) | H | \varphi_A(\vec{r} - \vec{R}_{Ai}) \rangle \qquad (2.14)$$

so, the diagonal elements of the transfer matrix are:

$$H_{AA} = H_{BB} = \frac{1}{N} \sum_{i=1}^{N} \varepsilon = \frac{N\varepsilon}{N} = \varepsilon \qquad (2.15)$$

With the same analysis, the diagonal elements of the overlap matrix are:

$$S_{AA} = S_{BB} = \sum_{i=1}^{N} \sum_{j=1}^{N} e^{i\vec{k}\cdot(\vec{R}_{Aj} - \vec{R}_{Ai})} \langle \varphi_A(\vec{r} - \vec{R}_{Ai}) | \varphi_A(\vec{r} - \vec{R}_{Ai}) \rangle = 1 \qquad (2.16)$$

With H_{AA}, H_{BB}, S_{AA} and S_{BB} solved simplistically, we move on to the off-diagonal matrix

elements. The interaction among atoms that are further apart become increasingly

negligible, so a simple approach to solving the off-diagonal elements is to only consider

nearest-neighbor atoms, in which there are only three. Thus, the first off-diagonal term is:

$$H_{AB} = \frac{1}{N} \sum_{i=1}^{N} \sum_{j=1}^{3} e^{i\vec{k}\cdot(\vec{R}_{Bj} - \vec{R}_{Ai})} \langle \varphi_A(\vec{r} - \vec{R}_{Ai}) | H | \varphi_A(\vec{r} - \vec{R}_{Bj}) \rangle \qquad (2.17)$$

The coupling strength to any of an A atom should be identical to each of the three

neighboring B atoms, so that we can define it to be a constant, known as the nearest

neighbor intralayer hopping parameter γ_0:

$$\gamma_0 \equiv -\langle \varphi_A(\vec{r} - \vec{R}_{Ai}) | H | \varphi_A(\vec{r} - \vec{R}_{Bj}) \rangle \qquad (2.18)$$

where the position vector between neighboring atoms is defined as:

$$\vec{\delta}_j \equiv \vec{R}_{Bj} - \vec{R}_{Ai} \qquad (2.19)$$

so that equation 2.17 becomes:

$$H_{AB} = -\frac{1}{N} \sum_{i=1}^{N} \sum_{j=1}^{3} e^{i\vec{k}\cdot\vec{\delta}_j} \gamma_0 f(k) \qquad (2.20)$$

where we have defined:

11

$$f(k) \equiv \sum_{j=1}^{3} e^{i\vec{k} \cdot \vec{\delta}_j} \tag{2.21}$$

The term $f(k)$ should be calculated explicitly to determine the matrix element H_{AB}.

The vector $\vec{\delta}_i$ points to the three nearest neighboring atoms, with the forms

$$\vec{\delta}_1 = \left(\frac{a}{2}, -\frac{a}{2\sqrt{3}}\right), \vec{\delta}_2 = \left(-\frac{a}{2}, -\frac{a}{2\sqrt{3}}\right), \vec{\delta}_3 = \left(0, \frac{a}{\sqrt{3}}\right) \tag{2.22}$$

Thus

$$f(k) = e^{i\vec{k} \cdot \vec{\delta}_1} + e^{i\vec{k} \cdot \vec{\delta}_2} + e^{i\vec{k} \cdot \vec{\delta}_3}$$

$$= e^{\frac{ik_x a}{2}} e^{-\frac{ik_y a}{2\sqrt{3}}} + e^{-\frac{ik_x a}{2}} e^{-\frac{ik_y a}{2\sqrt{3}}} + e^{\frac{ik_y a}{\sqrt{3}}}$$

$$= e^{\frac{ik_y a}{\sqrt{3}}} + 2e^{-\frac{ik_y a}{2\sqrt{3}}} \cos\left(\frac{k_x a}{2}\right) \tag{2.23}$$

Similarly, the off-diagonal overlap matrix element S_{AB} is given by:

$$S_{AB} = \frac{1}{N} \sum_{i=1}^{N} \sum_{j=1}^{3} e^{i\vec{k} \cdot (\vec{R}_{Bj} - \vec{R}_{Ai})} \left\langle \varphi_A(\vec{r} - \vec{R}_{Ai}) \middle| \varphi_B(\vec{r} - \vec{R}_{Bi}) \right\rangle = S_0 f(k) \tag{2.24}$$

where S_0 is also a constant and is defined similarly to γ_0:

$$S_0 = \left\langle \varphi_A(\vec{r} - \vec{R}_{Ai}) \middle| \varphi_B(\vec{r} - \vec{R}_{Bi}) \right\rangle \tag{2.25}$$

Therefore, the transfer integral matrix H_{SLG} and the overlap matrix S_{SLG} for SLG are:

$$H_{SLG} = \begin{bmatrix} \varepsilon_A & -\gamma_0 f(k) \\ -\gamma_0 f^*(k) & \varepsilon_B \end{bmatrix} \tag{2.26}$$

$$S_{SLG} = \begin{bmatrix} 1 & S_0 f(k) \\ S_0 f^*(k) & 1 \end{bmatrix} \tag{2.27}$$

Plugging equations 2.26 and 2.27 into 2.11, and setting $\varepsilon_A = \varepsilon_A = \varepsilon$, we obtain

$$det \begin{vmatrix} \varepsilon - E(k) & -(\gamma_0 + E(k)S_0)f(k) \\ -(\gamma_0 + E(k)S_0)f^*(k) & \varepsilon - E(k) \end{vmatrix} = 0 \tag{2.28}$$

Solving the determinant gives us:

$$(\varepsilon - E(k))^2 - (\gamma_0 + E(k)S_0)^2|f(k)|^2 = 0 \tag{2.29}$$

This is simply a quadratic equation with the form:

$$E^2(k)\left[1 - S_0{}^2|f(k)|^2\right] + E(k)[-2 - 2\gamma_0 S_0|f(k)|^2] + \varepsilon^2 - \gamma_0{}^2|f(k)|^2 = 0 \tag{2.30}$$

which has a solution:

$$E_\pm(k) = \frac{\varepsilon \pm \gamma_0|f(k)|}{1 \mp S_0|f(k)|} \tag{2.31}$$

where E_+ (E_-) corresponds to the conduction (valence) band.

The primitive reciprocal lattice vectors $\vec{b}_1$ and $\vec{b}_2$ connect the points K_+ and K_- to the two other corners of the Brillouin zone, respectively, as shown in figure 2.1b, but they explicitly cannot connect K_+ to K_-, meaning that these two points themselves are inequivalent, and they are referred to as valleys. These two points in 2D momentum space (k_x, k_y) are defined as the following, with respect to the gamma point:

$$\vec{K}_\xi = \xi\left(\frac{4\pi}{3a}, 0\right) \tag{2.32}$$

where $\xi = +1$ (-1) for the K_+ (K_-) valley. If we define the momentum

$$\vec{p} = \hbar\vec{k} - \hbar\vec{K}_\xi \tag{2.33}$$

then the function $f(k)$ from equation 2.23 becomes:

$$f(k) = e^{\frac{ip_y a}{\sqrt{3}\hbar}} + 2e^{-\frac{ip_y a}{2\sqrt{3}\hbar}}\cos\left(\frac{2\pi\xi}{3} + \frac{p_x a}{2\hbar}\right) \tag{2.34}$$

A Taylor series expansion to first order gives:

$$f(k) = 1 + \frac{ip_y a}{\sqrt{3}\hbar} + 2\left(1 - \frac{ip_y a}{2\sqrt{3}\hbar}\right)\left[(1)\left(-\frac{1}{2}\right) - \left(\frac{\sqrt{3}}{2}\right)\left(\frac{\xi\sqrt{3}p_x a}{2\hbar}\right) + \ldots\right] \tag{2.35}$$

which simplifies to:

$$f(k) = -\frac{\sqrt{3}a}{2\hbar}(\xi p_x - ip_y) \tag{2.36}$$

13

Thus, in the low energy regime near the Dirac points, $\varepsilon \sim 0$, and using equation 2.36 and its complex conjugate, the Hamiltonian from equation 2.26 reduces to a simple form:

$$H_{SLG} = v_F \begin{bmatrix} 0 & \xi p_x - ip_y \\ \xi p_x + ip_y & 0 \end{bmatrix} = v_F \begin{bmatrix} 0 & \pi^\dagger \\ \pi & 0 \end{bmatrix} \tag{2.37}$$

where

$$\pi = \xi p_x + ip_y \tag{2.38}$$

and the Fermi velocity v_F is:

$$v_F = \frac{\sqrt{3}a\gamma_0}{2\hbar} \tag{2.39}$$

Therefore, the massless Dirac quasiparticles that transport through a SLG lattice at low energies can be described by a simple $\vec{k} \cdot \vec{p}$ Hamiltonian. Plugging in the values for $a = 2.46$ Å and using $\gamma_0 = 3.033$ eV into equation 2.39, we arrive at a Fermi velocity of ~9.8 x 10^5 m/s, which is 0.3% the speed of light. From equation 2.37, the energy eigenvalues and eigenvectors are simply:

$$E_{SLG}^{\pm} = \pm vp \tag{2.40}$$

$$\Phi_{SLG}^{\pm} = \frac{1}{\sqrt{2}} \binom{1}{\pm e^{\pm i\varphi}} e^{\frac{i}{\hbar}\vec{p}\cdot\vec{r}} \tag{2.41}$$

Equation 2.40 shows that in the low energy regime, the energy of electrons near the Dirac points K_+ and K_- are linear, and thus the charger carriers are relativistic, like photons, except they move at a speed that is $1/300$ of c. The energy $E_{\pm}(k)$ from equation 2.31 and the corresponding low energy continuum limit in equation 2.40 are shown in figure 2.2.
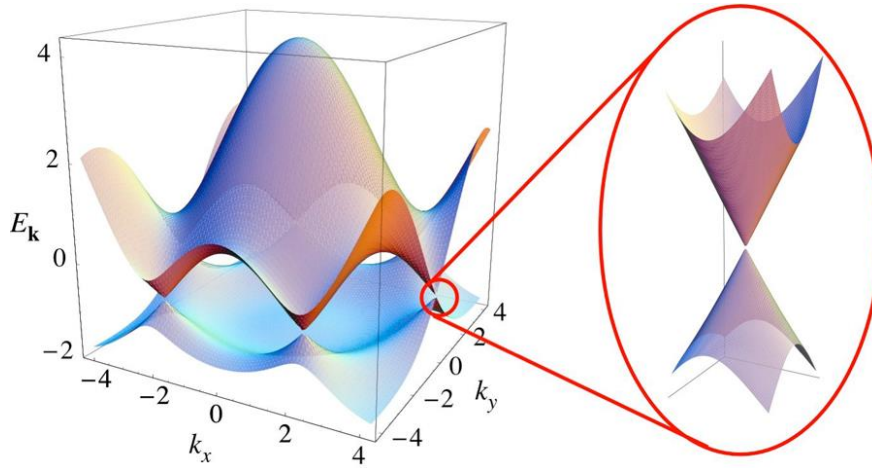
Figure 2.2. Electronic band structure of SLG from TB calculation: The full tight binding energy *E(k)* of the electronic band structure of SLG with $\gamma_0 = 3.033$ eV. The energy dispersion near the Dirac points is linear. Image taken from ref. 2.

2.2.2 Bilayer graphene

Bilayer graphene (BLG) consists of two layers of graphene stacked upon each other such that the *A* sub-lattice of the top layer is directly above the *B* sub-lattice of the bottom layer, forming a dimer bond between the stacked atoms[3]. There are four atoms in the unit cell for BLG, two from each sub-lattice and two from each layer, in a rhombus-shape[3], as shown in figure 2.3a. If the two layers didn't interact in any way, then the Hamiltonian for BLG would simply consist of the Hamiltonian in equation 2.26 repeated twice in the upper left and lower right-hand corners of the matrix, with other coupling matrix elements zero. However, the additional inter- and intralayer hopping parameters modify the Hamiltonian dramatically.

The interlayer hopping parameter γ_1 denotes the coupling between the stacked atoms, *i.e.* the B_1 atom of the bottom layer and the A_2 atom of the top layer, γ_3 denotes

that between the A_1 atom of the bottom layer and the B_2 atom of the top layer, and γ_4 between the A_1 atom of the bottom layer and the A_2 atom of the top layer.
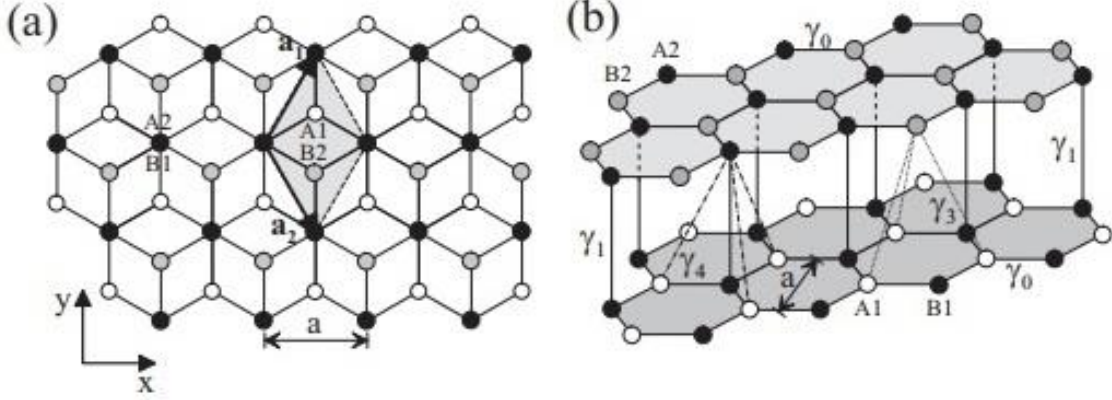
Figure 2.3. Lattice structure of BLG: (a) Top view of the BLG lattice. Black and white circles correspond to the bottom layer and black and grey circles correspond to the top layer. The unit cell is the shaded rhombus region. (b) Side view of the BLG lattice showing hopping parameters γ_0, γ_1, γ_3 and γ_4. Image taken from ref 3.

Since γ_1 is a dimer bond between the B_1 atom of the bottom layer and A_2 atom of the top layer, it logically follows that it would appear in two places in the transfer integral matrix, namely in the H_{23} and the H_{32} matrix elements. Considering hopping parameters γ_0, γ_1, γ_3 and γ_4, as shown in figure 2.3b, the transfer integral matrix for BLG has the form of two 2x2 SLG transfer integral matrices and their associated couplings. The rows and columns of the 4x4 transfer integral matrix for BLG are ordered as A_1, B_1, A_2, B_2, so that:

$$H_{BLG} = \begin{bmatrix} \varepsilon_{A1} & -\gamma_0 f(k) & \gamma_4 f(k) & -\gamma_3 f^*(k) \\ -\gamma_0 f^*(k) & \varepsilon_{B1} & \gamma_1 & \gamma_4 f(k) \\ \gamma_4 f^*(k) & \gamma_1 & \varepsilon_{A2} & -\gamma_0 f(k) \\ -\gamma_3 f(k) & \gamma_4 f^*(k) & -\gamma_0 f^*(k) & \varepsilon_{B2} \end{bmatrix} \tag{2.42}$$

In this calculation of the electronic band structure of BLG, we will only consider γ_0 and γ_1, the nearest-neighbor intra- and interlayer hopping parameters, respectively. Thus, the transfer integral and the overlap integral matrices simply to

$$H_{BLG} = \begin{bmatrix} \varepsilon_{A1} & -\gamma_0 f(k) & 0 & 0 \\ -\gamma_0 f^*(k) & \varepsilon_{B1} & \gamma_1 & 0 \\ 0 & \gamma_1 & \varepsilon_{A2} & -\gamma_0 f(k) \\ 0 & 0 & -\gamma_0 f^*(k) & \varepsilon_{B2} \end{bmatrix} \qquad (2.43)$$

$$S_{BLG} = \begin{bmatrix} 1 & S_0 f(k) & 0 & 0 \\ S_0 f^*(k) & 1 & S_1 & 0 \\ 0 & S_1 & 1 & S_0 f(k) \\ 0 & 0 & S_0 f^*(k) & 1 \end{bmatrix} \qquad (2.44)$$

where S_1 is the coupling between the B_1 and A_2 atoms:

$$S_1 = \langle \varphi_{A2}(\vec{r} - \vec{R}_{A2}) | \varphi_{B1}(\vec{r} - \vec{R}_{B1}) \rangle \qquad (2.45)$$

We will consider the low energy regime when calculating the band structure for BLG and set $\varepsilon_{A1} = \varepsilon_{B1} = \varepsilon_{A2} = \varepsilon_{B2} = S_0 = S_1 = 0$, so that the overlap matrix becomes an identity matrix and the determinant to the secular equation has the form:

$$\det(H - ES) = \det \begin{vmatrix} -E & -\gamma_0 f(k) & 0 & 0 \\ -\gamma_0 f(k) & -E & \gamma_1 & 0 \\ 0 & \gamma_1 & -E & -\gamma_0 f(k) \\ 0 & 0 & -\gamma_0 f(k) & -E \end{vmatrix} = 0 \quad (2.46)$$

Expanding the determinant along the first column gives:

$$\det(H - ES) = -E \cdot \det \begin{vmatrix} -E & \gamma_1 & 0 \\ \gamma_1 & -E & -\gamma_0 f(k) \\ 0 & -\gamma_0 f(k) & -E \end{vmatrix} +$$

$$\gamma_0 f(k) \cdot \det \begin{vmatrix} -\gamma_0 f(k) & 0 & 0 \\ \gamma_1 & -E & -\gamma_0 f(k) \\ 0 & -\gamma_0 f(k) & -E \end{vmatrix} = 0 \qquad (2.47)$$

Solving these two 3x3 determinants gives:

$$E^4 + \{-[\gamma_0 f(k)]^2 - \gamma_1{}^2\}E^2 + [\gamma_0 f(k)]^4 = 0 \qquad (2.48)$$

which is simply a quadratic equation in E^2 and has a solution:

$$E^2 = \frac{\gamma_0{}^2|f(k)|^2 + \gamma_1{}^2 \pm \sqrt{\{\gamma_0{}^2|f(k)|^2 + \gamma_1{}^2\}^2 - 4\gamma_0{}^4|f(k)|^4}}{2} \qquad (2.49)$$

Neglecting higher order term, we are left with:

$$E_\pm(\alpha, k) = \pm \frac{\gamma_1}{2} \left\{ \sqrt{1 + \frac{4\gamma_0{}^2|f(k)|^2}{\gamma_1{}^2}} + \alpha \right\} \qquad (2.50)$$

where $\alpha = \pm 1$. E_+ (E_-) corresponds to the conduction (valence) band, and $\alpha = +1$ (-1)

corresponds to the higher (lower) energy band. Using a Maclaurin series expansion of

equation 2.50 to first order, setting $\alpha = -1$ for the low energy regime, and employing

equations 2.36 and 2.39, we arrive at:

$$E_-(\alpha = -1, k) = -\frac{\gamma_0{}^2|f(k)|^2}{\gamma_1} = -\frac{1}{2m}(\xi p_x - i p_y)^2 \qquad (2.51)$$

where

$$m = \frac{\gamma_1}{2v_F{}^2} \qquad (2.52)$$

From equation 2.51, we see that BLG has acquired a mass from the interlayer hopping

parameter γ_1, with a quadratic energy dispersion. Since next-nearest intra- and interlayer

hopping parameters have been neglected and we focused to the low energy regime, the

effective Hamiltonian for BLG can be reduced to the following:

$$H_{BLG}^{Eff} = -\frac{1}{2m} \begin{bmatrix} 0 & (\xi p_x - i p_y)^2 \\ (\xi p_x + i p_y)^2 & 0 \end{bmatrix} \qquad (2.53)$$

Thus, BLG at low energies has energy eigenvalues and eigenvectors:

$$E_{BLG}^\pm = \pm \frac{p^2}{2m} \qquad (2.54)$$

$$\Phi_{BLG}^{\pm} = \frac{1}{\sqrt{2}} \left(\begin{matrix} 1 \\ \mp e^{\mp 2i\xi\varphi} \end{matrix} \right) e^{\frac{i}{\hbar}\vec{p}\cdot\vec{r}} \tag{2.55}$$

The low energy band spectrum of BLG is plotted in figure 2.4.
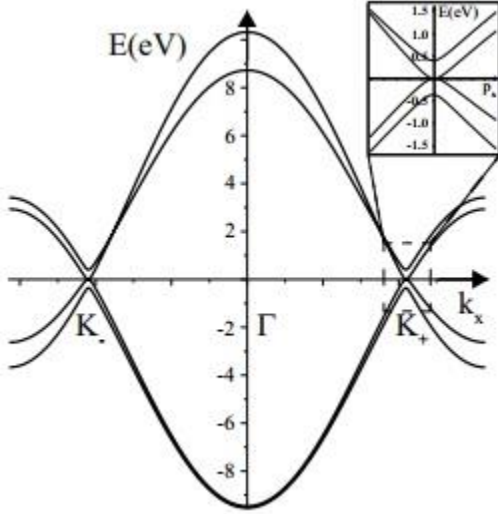
Figure 2.4. Electronic low-energy band spectrum of BLG: Plot with parameters: γ_0 = 3.16 eV, γ_1 = 0.381 eV, γ_3 = 380 meV, γ_4 = 140 meV, $\varepsilon_{B1} = \varepsilon_{A2}$ = 22 meV and $\varepsilon_{A1} = \varepsilon_{B2}$ = 0. Inset shows quadratic sub-bands near the K_+ Dirac point. Image taken from ref. 3.

2.2.3 Bernal-stacked trilayer graphene

As we saw in the previous section, the band structure for BLG differs

significantly from SLG. As more layers are added to graphene, different properties

continue to emerge, and more configurations become available. While SLG and BLG

have only one stable stacking configuration, trilayer graphene (TLG) has two stable or

metastable stacking configurations: Bernal and rhombohedral. In Bernal-stacked TLG (B-

TLG), also known as ABA TLG, the B_3 atom from the top layer sits directly above the A_2

atom from the middle layer and the B_1 atom of the bottom layer[4], as shown in figure

2.5a-c. Rhombohedral-stacked TLG (r-TLG), however, consists of two Bernal-stacked

19

bilayers conjoined at the middle layer, such that a dimer bond forms between the A_3 atom of the top layer and the B_2 atom of the middle layer, while the A_2 atom of the middle layer makes a dimer bond with the B_1 atom of the bottom layer, as shown in figure 2.5d,e.
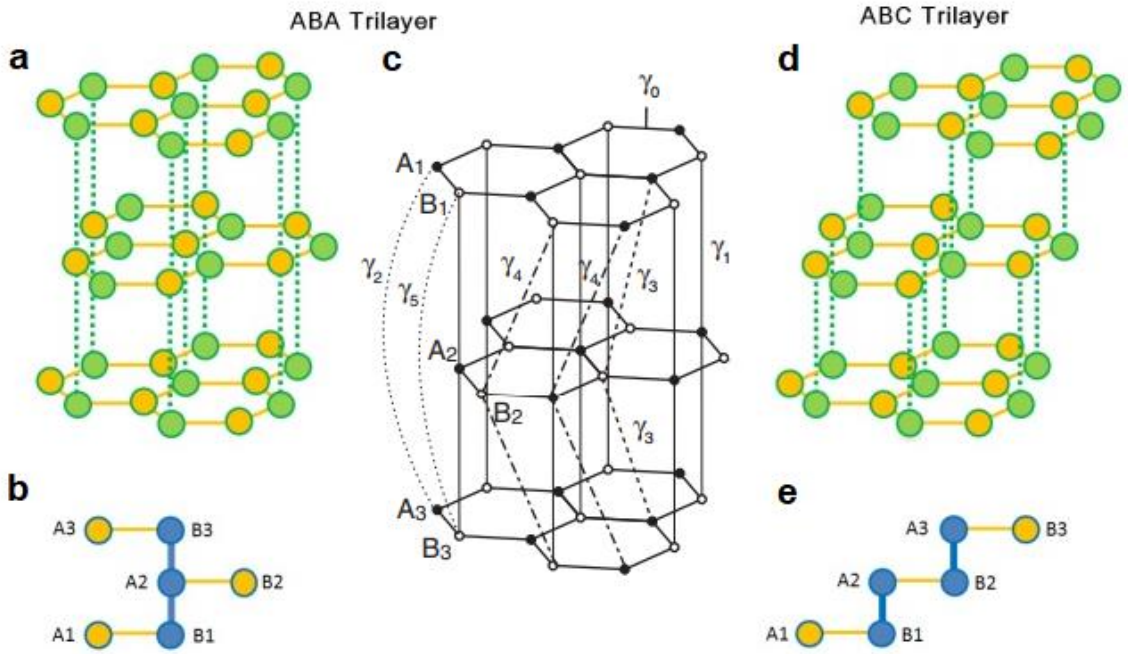
Figure 2.5. Crystal lattice structure of B-TLG: (a) Lattice structure diagram of B-TLG. (b) Side view of B-TLG lattice showing interlayer dimer bonds between atoms B_1 and A_2, and A_2 and B_3. (c) Hopping parameters γ_1 - γ_5 for B-TLG. (d) Lattice structure diagram of r-TLG. (e) Side view of r-TLG lattice showing interlayer dimer bonds between atoms B_1 and A_2, and B_2 and A_3. Images (a), (b), (d), and (e) are taken from ref. 4; image (c) is taken from ref. 5.

By considering the hopping parameters γ_0 - γ_6, the transfer integral matrix can be written down by inserting hopping parameters into the appropriate coupling matrix elements of the 6x6 matrix, with the rows and columns ordered as $A_1, B_1, A_2, B_2, A_3, B_3$, so that:

$$
H_{B-TLG} = \begin{bmatrix}
\varepsilon_{A1} & v_0\pi^\dagger & -v_4\pi^\dagger & v_3\pi & \gamma_2 & v_6\pi \\
v_0\pi & \varepsilon_{B1} & \gamma_1 & -v_4\pi^\dagger & v_6\pi & \gamma_5 \\
-v_4\pi & \gamma_1 & \varepsilon_{A2} & v_0\pi^\dagger & -v_4\pi & \gamma_1 \\
v_3\pi^\dagger & -v_4\pi & v_0\pi & \varepsilon_{B2} & v_3\pi^\dagger & -v_4\pi \\
\gamma_2 & v_6\pi^\dagger & -v_4\pi^\dagger & v_3\pi & \varepsilon_{A3} & v_0\pi^\dagger \\
v_6\pi^\dagger & \gamma_5 & \gamma_1 & -v_4\pi^\dagger & v_0\pi & \varepsilon_{B3}
\end{bmatrix}
\tag{2.56}
$$

where we have employed equations 2.20 and 2.36, and introduced the relation:

$$
v_i = \frac{\sqrt{3}a}{2\hbar}\gamma_i
\tag{2.57}
$$

The hopping parameters γ_0 - γ_5 for B-TLG are shown in figure 2.5c. The hopping

parameter γ_6, not shown in figure 2.5c, is similar to γ_5, except it connects the A_1 atom of

the bottom layer to the B_3 atom of the top layer. Next-nearest neighbor, next-next-nearest

neighbor hopping terms, and so on, become increasingly negligible due to their large $\vec{\delta}$

vectors which appear in the *f(k)* function from equation 2.23, so assuming the low energy

limit and only considering the nearest neighbor intra- and interlayer hopping parameters,

γ_0 and γ_1, respectively, the transfer integral matrix for B-TLG reduces to:

$$
H_{B-TLG} = \begin{bmatrix}
0 & v_0\pi^\dagger & 0 & 0 & 0 & 0 \\
v_0\pi & 0 & \gamma_1 & 0 & 0 & 0 \\
0 & \gamma_1 & 0 & v_0\pi^\dagger & 0 & \gamma_1 \\
0 & 0 & v_0\pi & 0 & 0 & 0 \\
0 & 0 & 0 & 0 & 0 & v_0\pi^\dagger \\
0 & 0 & \gamma_1 & 0 & v_0\pi & 0
\end{bmatrix}
\tag{2.58}
$$

Note that this matrix strongly resembles the Hamiltonian for SLG from equation 2.37,

except with an additional coupling from γ_1 from atoms B_1 and A_2 (similar to BLG) and

A_2 and B_3. Thus, the Hamiltonian for B-TLG, when only considering hopping parameters

γ_0 and γ_1, resembles a so-called 2+1 model, incorporating a linear band structure

dependence from SLG and a quadratic band structure from BLG. Namely, by applying

the following unitary transformation[6],

$$
U = \sqrt{2}\begin{bmatrix} 0 & 0 & 0 & 1 & 0 & 0 \\ 0 & 0 & 0 & -1 & 0 & 0 \\ \sqrt{2} & 0 & 0 & 0 & 1 & 0 \\ 0 & \sqrt{2} & 0 & 0 & 1 & 0 \\ 0 & 0 & 0 & 0 & 0 & 1 \\ 0 & 0 & 0 & 0 & 0 & 1 \end{bmatrix} \tag{2.59}
$$

the Hamiltonian transforms to:

$$
H_{B-TLG} = \begin{bmatrix} 0 & v_0\pi^\dagger & 0 & 0 & 0 & -\sqrt{2}\gamma_1 \\ v_0\pi & 0 & 0 & 0 & 0 & 0 \\ 0 & 0 & 0 & v_0\pi^\dagger & 0 & 0 \\ 0 & 0 & v_0\pi & 0 & 0 & 0 \\ 0 & 0 & 0 & 0 & 0 & v_0\pi^\dagger \\ -\sqrt{2}\gamma_1 & 0 & 0 & 0 & v_0\pi & 0 \end{bmatrix} \tag{2.60}
$$

This matrix can now be diagonalized using the Löwdin-partitioning method to obtain the

effective low energy Hamiltonian[6]:

$$
H_{B-TLG} = \begin{bmatrix} 0 & \frac{v_0^2(\pi^\dagger)^2}{\sqrt{2}\gamma_1} & 0 & 0 \\ \frac{v_0^2(\pi)^2}{\sqrt{2}\gamma_1} & 0 & 0 & 0 \\ 0 & 0 & 0 & v_0\pi^\dagger \\ 0 & 0 & v_0\pi & 0 \end{bmatrix} \tag{2.61}
$$

The low energy effective Hamiltonian for B-TLG using only hopping parameters γ_0 and

γ_1 explicitly shows the 2+1 model in equation 2.42. The low energy band structure is

plotted in figure 2.6.
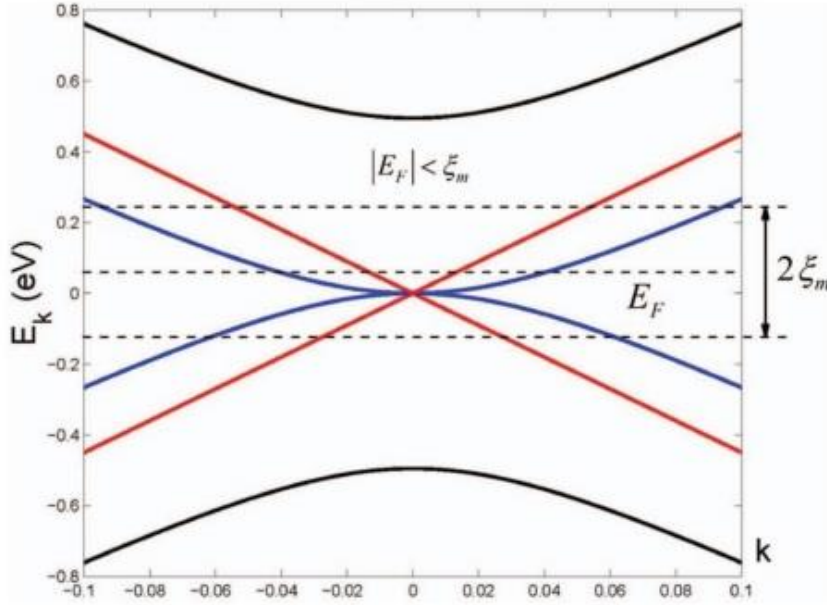
Figure 2.6. Electronic band structure of B-TLG: 2+1 model shows BLG quadratic sub-bands (black and blue) and SLG linear bands (red). ξ_m indicates the Debye frequency. Image taken from ref. 6.

It is worthwhile to note that the band structure for B-TLG is modified when more hopping parameters are used. For instance, when including hopping parameters γ_0, γ_1, γ_2, γ_5 and the onsite energy difference of two inequivalent carbon atoms of the same layer, δ, the band structure loosely resembles the 2+1 model, however, the monolayer and bilayer bands are shifted, as shown in figure 2.7[7]. Here, the SLG bands have separated by $\sim \delta + \frac{\gamma_2}{2} - \frac{\gamma_5}{2} = 2\ meV$, and the BLG bands have separated by $\sim \frac{|\gamma_2|}{2} = 14\ meV$, however, the relative shift results in no overall band gap, so B-TLG remains semi-metallic[7].
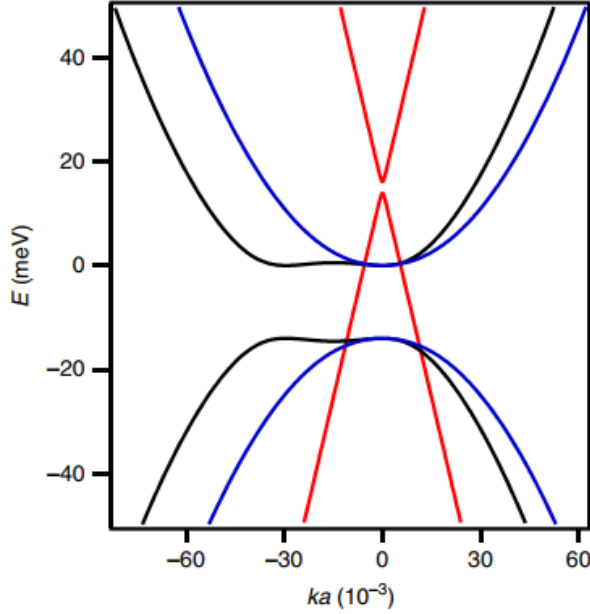
Figure 2.7. Electronic band structure of B-TLG: Band structure calculation at low energy for B-TLG around the K_- point including parameters including parameters $\gamma_0 = 3.1$ eV, $\gamma_1 = 390$ meV, $\gamma_2 = -28$ meV, $\gamma_5 = 10$ meV, and carbon atom intralayer onsite energy difference $\delta = 21$ meV. Image taken from ref. 7.

2.2.4 Rhombohedral-stacked few-layer graphene

In this section, we will use the results of the tight binding Hamiltonian calculations for r-TLG to generalize rhombohedral-stacked few-layer graphene. The lattice structure of r-TLG is shown in figures 2.5d,e and 2.8. A dimer bond forms between the A_3 atom of the top layer and the B_2 atom of the middle layer, while the A_2 atom of the middle layer makes a dimer bond with the B_1 atom of the bottom layer. Similar to the B-TLG case, we will start by considering the atoms A_1, B_1, A_2, B_2, A_3 and B_3 and the hopping parameters γ_0 - γ_6. The hopping parameters γ_1 - γ_4 for r-TLG are shown in figure 2.8b; the hopping parameters not shown are γ_0, which is the nearest neighbor
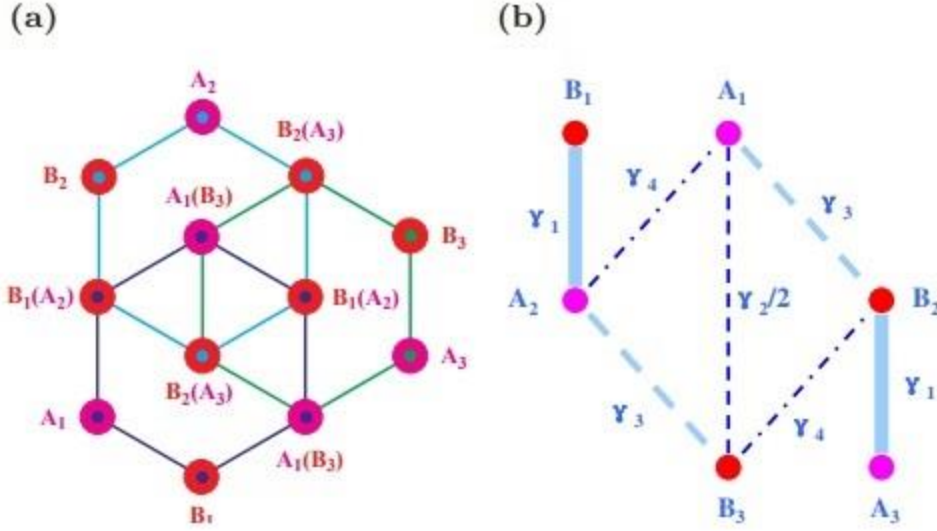
Figure 2.8. Crystal lattice structure of r-TLG: (a) overhead view of r-TLG lattice. (b) Side view of r-TLG lattice showing interlayer hopping parameters γ_1, γ_2, γ_3 and γ_4. Image taken from ref. 8.

interlayer hopping parameter, and γ_5 and γ_6, which are couplings from sites B_1 to A_3, and A_1 to A_3, respectively. We see that the Hamiltonian can be written down by inserting hopping parameters into the appropriate coupling matrix elements of the 6x6 transfer integral matrix, as follows:

$$H_{r-TLG} = \begin{bmatrix} \varepsilon_{A1} & v_0\pi^\dagger & v_4\pi^\dagger & v_3\pi & v_6\pi & \frac{\gamma_2}{2} \\ v_0\pi & \varepsilon_{B1} & \gamma_1 & v_4\pi^\dagger & v_5\pi^\dagger & v_6\pi \\ v_4\pi & \gamma_1 & \varepsilon_{A2} & v_0\pi^\dagger & v_4\pi^\dagger & v_3\pi \\ v_3\pi^\dagger & v_4\pi & v_0\pi & \varepsilon_{B2} & \gamma_1 & v_4\pi^\dagger \\ v_6\pi^\dagger & v_5\pi & v_4\pi & \gamma_1 & \varepsilon_{A3} & v_0\pi^\dagger \\ \frac{\gamma_2}{2} & v_6\pi^\dagger & v_3\pi^\dagger & v_4\pi & v_0\pi & \varepsilon_{B3} \end{bmatrix} \quad (2.62)$$

where we have employed equations 2.20, 2.36 and 2.57. Similar to the B-TLG model, we ignore the weak couplings γ_2 - γ_6, so equation 2.62 reduces to an effective form, valid for rhombohedral-stacked few-layer graphene of two layers and up:

$$H_{ABC}^{Eff} = \begin{bmatrix} 0 & v_0\pi^\dagger & 0 & 0 & 0 & 0 & \cdots \\ v_0\pi & 0 & \gamma_1 & 0 & 0 & 0 & \cdots \\ 0 & \gamma_1 & 0 & v_0\pi^\dagger & 0 & 0 & \cdots \\ 0 & 0 & v_0\pi & 0 & \gamma_1 & 0 & \cdots \\ 0 & 0 & 0 & \gamma_1 & 0 & v_0\pi^\dagger & \cdots \\ 0 & 0 & 0 & 0 & v_0\pi & 0 & \\ \vdots & \vdots & \vdots & \vdots & \vdots & & \ddots \end{bmatrix} \tag{2.63}$$

Equation 2.63 is starting to look a lot like the Hamiltonian for SLG (2.37) and BLG (2.52). It turns out that rhombohedral-stacked N-layer graphene can be explained by an N-chiral 2D electron system[9], and the effective Hamiltonian for N-layer ABC-stacked graphene is:

$$H_{ABC}^N = -\gamma_1 \begin{bmatrix} 0 & (v^\dagger)^2 \\ v^2 & 0 \end{bmatrix} \tag{2.64}$$

with energy eigenvalues[9]:

$$E_{ABC}^\pm = \pm\gamma_1 \left(\frac{v_F}{\gamma_1}\right)^N \tag{2.65}$$

where

$$v = \frac{v_F\pi}{\gamma_1} \tag{2.66}$$

This shows that the band structure of multilayer rhombohedral-stacked graphene, when considering only the nearest neighbor intra- and interlayer hopping parameters in the low energy regime, scales with k^N, meaning that r-TLG has a cubic energy dispersion and r-4LG has a quartic energy dispersion. Thus, as we continue to add layers to the few-layer graphene lattice, we introduce more interlayer couplings which modify the band structure and steadily increase the order of the polynomial of its energy dispersion. Band structure calculations[9] show that this behavior of k^N energy dispersion holds to at least four layers of graphene, but further work is needed to determine when this trend breaks down and

behavior of three-dimensional graphite occurs. The electronic band structure is plotted in

figure 2.9 for r-TLG and r-4LG.
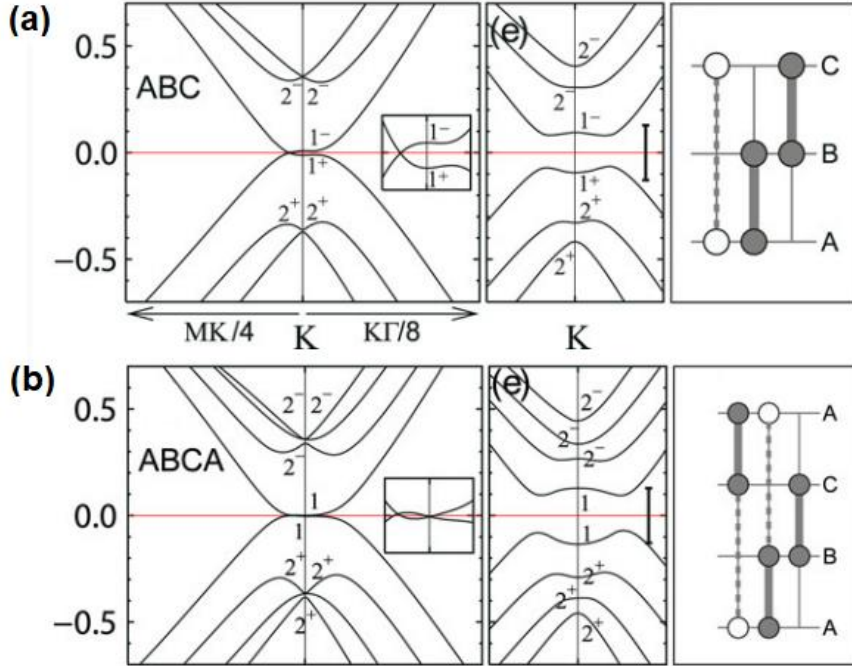
Figure 2.9. Electronic band structure of r-TLG and r-4LG with $\gamma_0 = 3eV$, $\gamma_1 = 0.363$ eV, and $\gamma_2 = 10$ meV: (a) r-TLG band structure. (b) r-4LG band structure. Image taken from ref 9.

2.3   Conclusion and references

Using the TB approximation that ignore remote hopping terms, we calculate that

SLG has a linear energy dispersion with relativistic charge carriers, BLG gains a mass

term and has a quadratic energy dispersion, and B-TLG consists of a superposition of the

quadratic bilayer and linear single layer energy bands. Finally, the energy dispersion of

N-layer rhombohedral-stacked multilayers of graphene, at least to four layers, scales as

k^N at low energies. These simple band structures serve as zero-order approximation for

understanding the electronic properties of few-layer graphene, but can be significantly

modified by remote hopping parameters and electronic interactions.

References

1. Ashcroft, N. W. and Mermin, N. D. *Solid State Physics*. Saunders College, Philadelphia, 1976.

2. Castro Neto, A. H., Guinea, F., Peres, N. M. R., Novoselov, K. S., and Geim, A. K. The electronic properties of graphene. *Rev. Mod. Phys.* **81**, 109 (2009).

3. McCann, E. and Koshino, M. The electronic properties of bilayer graphene. *Rep. Prog. Phys.* **76** (5), 056503 (2013).

4. Lui, C. H., Li, Z., Mak, K. F., Cappelluti, E., and Heinz, T. F. Observation of an electrically tunable band gap in trilayer graphene. *Nature Phys.*, **7**, 944-947 (2011).

5. Morimoto, T., and Koshino, M. Gate-induced Dirac cones in multilayer graphenes. *Phys. Rev. B*, **87**, 085424 (2013).

6. Liu, H., Jiang, H., and Xie, X. C. Intrinsic superconductivity in ABA-stacked trilayer graphene. *AIP Adv.*, **2**, 041405 (2012).

7. Datta, B., Dey, S., Samanta, A., Agarwal, H., Borah, A., Watanabe, K., Taniguchi, T., Sensarma, R., and Deshmukh, M. M. Strong electronic interactions and multiple quantum Hall ferromagnetic phases in trilayer graphene. *Nat. Commun.*, **8**, 14158 (2017).

8. Zhang, F., Sahu, B., Min, H., and MacDonald, A. H. Band structure of ABC-stacked graphene trilayers. *Phys. Rev. B.*, **82**, 035409 (2010).

9. Aoki, M. and Amawashi, H. Dependence of band structures on stacking and field in layered graphene. *Solid State Commun*. **142** (3), 123-127 (2007).

Chapter 3: Device Fabrication

3.1   Introduction

In this chapter, we will present the fabrication recipe employed for creating

doubly-suspended few-layer graphene (FLG) prototype field effect transistor (FET)

devices. This recipe was originally created by Gang Liu, Jairo Velasco Jr. and Chun Ning

(Jeanie) Lau, and later modified by Yongjin Lee and myself. This recipe entails a careful

sample characterization and a multi-level electron beam lithography (EBL) process which

results in both a suspended, contactless top gate and a suspended FLG membrane[1]. The

samples are prepared by the mechanical exfoliation of graphite, and the number of layers

and stacking order are determined. EBL is then used to define the device electrodes and a

suspended top gate, and wet-etched to suspend the graphene membrane. Current

annealing is performed post fabrication to improve sample quality.

3.2   Sample Preparation

To prepare samples, we exfoliate graphene from Kish graphite with scotch tape

onto oxidized silicon wafers, and use optical contrast and Raman spectroscopy to

determine the number of layers and stacking order of the FLG sheets.

3.2.1 Graphene Exfoliation

Kish graphite is used in all samples fabricated. First, the graphene is mechanically

exfoliated onto diced Silicon wafers with 300-nm SiO_2 surface layer using the scotch tape

technique[2]. The diced wafers are inspected under an optical microscope for exfoliated FLG flakes with the desired shape, thickness and surface homogeneity. Long, thin, and homogenous flakes are selected, typically. Sometimes graphene flakes with non-ideal shapes are patterned into the desired shape or geometry by inductively-coupled plasma (ICP) etching (see figure 3.4).

3.2.2 Identification of Thickness and Stacking Order

The thickness of a graphene flake can be estimated by measuring the relative green shift (RGS) between the flake and substrate,

$$RGS = \frac{G_S - G_G}{G_S} \qquad (3.1)$$

where G_S (G_G) is the green channel value of the substrate (graphene flake). Each layer of graphene has an opacity of $\pi\alpha = 2.3\%$, where $\alpha = 1/137$ is the fine structure constant; together with the thin film interference between lights paths that reflect off graphene, SiO_2 and Si, optical contrast under a standard optical microscope can be used an effective tool in estimating the number of layers of graphene. The RGS values for single layer graphene (SLG) and FLG are listed along with the Raman backscattering peak intensity ratio I_G/I_{2D} in table 3.1. A similar method can be employed to estimate the thickness of hexagonal boron nitride using the RGS value, and those results are discussed in Appendix A.1.

An additional tool for confirming the flake thickness is the use of Raman spectroscopy[3]. In particular, the G mode in graphite is a single resonance intravalley longitudinal optical phonon mode near the Γ point and the 2D mode is a double-

resonance intervalley scattering process which exhibits a strong frequency dependence on the excitation laser energy[5-7]. The ratio between the intensities of the peaks, I_G/I_{2D}, predictably and linearly increases with increasing number of layers[3,4]. We empirically determined the peak intensity ratio I_G/I_{2D} for the first four layers of graphene after taking Raman spectra from over one hundred samples; the measured I_G/I_{2D} values are shown along with RGS values in table 3.1. In this work, we used a Horiba LabRAM HR Evolution Raman laser with a 532-nm wavelength.

	RGS	I_G/I_{2D}
SLG	0.030 ± 0.010	0.8 ± 0.1
BLG	0.053 ± 0.013	1.5 ± 0.2
TLG	0.078 ± 0.013	2.2 ± 0.2
4LG	0.105 ± 0.015	2.8 ± 0.2

Table 3.1: Experimentally measured RGS and I_G/I_{2D} values for the first four layers of graphene.

To distinguish between Bernal and rhombohedral stacking orders, we rely upon the shape of the 2D, as shown in figure 3.1. The 2D peak in the Raman backscattering spectrum is symmetric for Bernal-stacked (B-) TLG and B-4LG, but it has a right-handed shoulder for rhombohedral-stacked (r-) TLG and r-4LG[8-10].
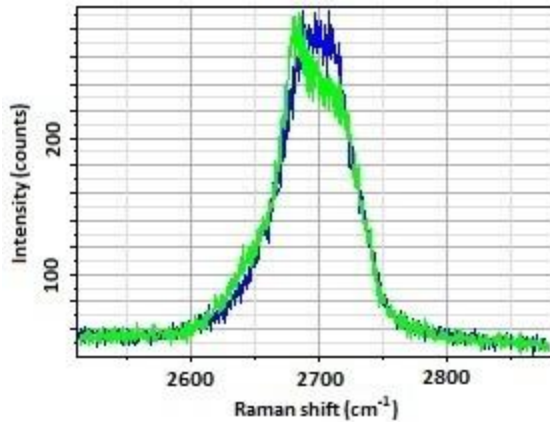
Figure 3.1. Raman spectra of 2D peak in TLG: The 2D peak of the Raman shift of Bernal- (blue) and rhombohedral- (green) stacked TLG show characteristically different shapes. While the 2D peak of B-TLG is symmetric, the 2D peak of r-TLG has a prominent right-handed shoulder.

3.3   Electron beam lithography

The second stage in sample fabrication is the process of electron beam lithography (EBL). A scanning electron microscope (SEM) is used to perform EBL so as to define alignment mark matrices, create a mask for dry etching if necessary, define a top gate and to define source/drain electrode patterns. In total, there are five to six lithographic steps required: two steps are required to make alignment marks, one optional step may be needed to dry-etch the graphene flake, two steps are required to define the top gate, and one step is required to write the source and drain electrodes. After the final lithography step, the entire device is submerged in buffered oxide etch (BOE) to create a suspended, dual-gated graphene device. These fabrication procedures are described in detail below.

3.3.1 Alignment Marks

Since the graphene flakes are small and randomly placed on the substrate, in order to couple them to metal contacts, we first fabricate alignment mark matrices around the selected graphene flakes. First, double layers of electron beam resists, methyl methacrylate (MMA) and polymethyl methacrylate (PMMA), are spun onto the sample, and each layer is baked at 180 ºC for ten minutes on a standard hot plate. Then a small dab of silver paint is placed on the sample, and its location on the diced wafer relative to the flake is noted for reference. Next, the sample is loaded into the SEM, and the beam is focused onto the sample using the conducting silver paint. Alignment marks are written surrounding the flake with a predetermined alignment mark matrix using a Nanometer Pattern Generation System (NPGS) file. After EBL exposure, the sample is developed in a 3:1 ratio of isopropyl alcohol (IPA) to methyl isobutyl ketone (MIBK) for 60 seconds, rinsed in IPA for 30 seconds, and dried with N_2 gas. The alignment mark matrix is 1.44 mm x 1.44 mm in size, which makes it relatively easy to successfully target a graphene flake on the 4-mm x 4-mm chip.

After the initial alignment mark matrix is exposed and developed, images of the sample with the resist mask are taken with an optical microscope. An additional four alignment marks are then patterned with NPGS to be ±35 and ±55 μm in the horizontal direction along the flake, in close proximity to the flake, as shown in figure 3.2. Finally, 10 nm of chromium and 80 nm of gold are then evaporated into the alignment mark patterns using an electron beam evaporator. The metal is lifted off in acetone at room

temperature for a couple hours and then rinsed in IPA. Optical images are taken of the metallic alignment marks to allow for future pattern designs with the NPGS program.
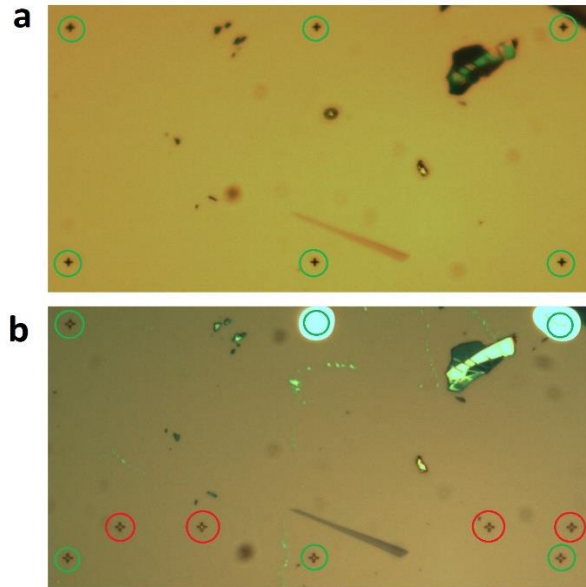
Figure 3.2. Optical images of alignment marks on a sample: (a) The alignment mark matrix, with crosses circled in green. The separation between the crosses is 60 μm. (b) Extra alignment marks in close proximity to the flake (circled in red) are written and overlaid onto the original alignment mark matrix crosses (circled in green).

3.3.2 Inductively-coupled plasma etching

For two-terminal devices, a rectangular-shaped flake is most desirable. To obtain rectangular flakes, sometimes an additional EBL step is required to define a mask for dry etching. Two layers of PMMA resist are spun onto the sample for 40 seconds at 4,000 rpm and 1,000 rpm/sec, and each layer is baked for 10 minutes. With the metal alignment marks visible under the resist layers, NPGS design patterns are then generated to map out areas on the flake to be etched away.

After exposing the sample with EBL, it is developed in IPA:MIBK (3:1) for 60 seconds, rinsed in IPA for 30 seconds and dried with N_2 gas. The sample is then placed on a 4" silicon wafer and loaded into the ICP etcher. O_2 or SF_6 gases are used to etch away the undesirable areas of the graphene flake. Typically, O_2 is admitted into the ICP chamber with DC power of 300 W and RF power of 30 W for 10-15 seconds. Figure 3.3 displays the optical images of a graphene flake at various stages during this etching step.
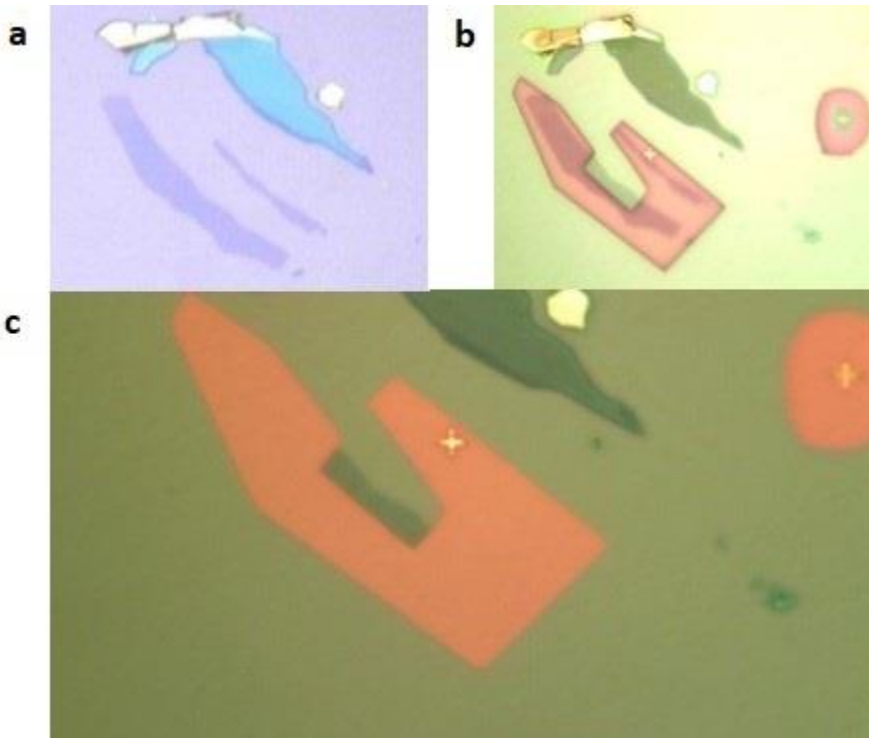
Figure 3.3. Inductively Coupled Plasma etching: (a) Graphene flake, as exfoliated onto an oxidized silicon wafer without electron beam resist. (b) Graphene flake with two layers of PMMA and a window in the resist opened with electron beam lithography. (c) The final, etched graphene flake, before removing the resist mask.

3.3.3 Suspended top gate fabrication

Fabrication of suspended, contactless top gates is a crucial step in the study of these suspended FLG devices. We typically design top gates such that their anchors are

about 1 μm away from the graphene flake and the top gate bridge is laterally separated from the source or drain electrodes by about 350 nm. Once the master NPGS file is completed, i.e. the entire device design, it is then decomposed into the three lithographic steps: *1E*, *2E*, and *3E*.

The *1E* step is the first lithographic step for fabricating the suspended top gate, and it defines the top gate electrode and anchors. The *1E* step requires spinning and baking lift-off resist (LOR) and PMMA onto the sample. The LOR 3B is spun onto the sample first at 4,000 rpm for 40 seconds with acceleration and deceleration rates of 300 rpm/sec. Next, the sample is baked for five minutes at 190 °C. Another layer of PMMA is then spun on the sample at 4,000 rpm for 40 seconds with acceleration and deceleration rates of 1,000 rpm/second, and baked at 180 °C for 10 minutes. Again, a dab of silver paint is placed onto the sample for focusing purposes in the SEM. With proper doses determined from dose tests with the corresponding electron beam resists, the *1E* pattern is written on the sample. The typical dosages range from 250 to 600 $\mu C/cm^2$ with an electron beam accelerating voltage of 20 kV.

After exposure from the e-beam, the sample is developed by submerging it into a solution with a 3:1 ratio of IPA:MIBK at room temperature for 60 seconds. MIBK is used to open the PMMA window. The sample is then placed in IPA for 30 seconds, and observed under an optical microscope. If the PMMA window is completely opened in the resist mask without under- or over-developing, then we can proceed to develop in MF319 solution for about two seconds to open the LOR window. The sample is then quickly moved to deionized water for five minutes, and subsequently gently dried with N_2 gas.

The final process of the *1E* step is to remove the top-most PMMA layer by submerging the sample in acetone at room temperature for ten minutes, then rinsing with IPA and drying with N_2 gas. Now the entire top gate pattern is opened in the LOR window except for the top gate bridge.

In the second lithographic step for fabricating the suspended top gate, the *2E* step, the top gate electrodes and anchors are defined again, together with the air-bridge. LOR still remains on the sample from the *1E* step, and this is a vital requisite: a small rectangular region of LOR must remain on the sample where the top gate bridge is to be located. This serves as a sacrificial layer for depositing metals for the bridge. LOR 3B is used because it has a film thickness of 300 nm when spun at the specifications discussed above. Step *2E* involves spinning, sequentially, one layer of MMA and one layer of PMMA onto the chip for 40 seconds at 4,000 rpm with acceleration and deceleration rates of 1,000 rpm/sec; each layer is baked for 10 minutes at 180 °C. MMA is used because of its undercut after developing which facilitates the formation of robust anchors. Again, a dab of silver paint is applied to the sample and the *2E* step is written with the EBL with correct doses as determined from dose tests. Since the LOR was already developed in the *1E* step, we use IPA:MIBK (3:1) to develop the MMA and PMMA layers for 60 seconds, then rinse in IPA for 30 seconds and dry with N_2 gas.

The MMA/PMMA window is now open. After inspecting under an optical microscope, the sample is ready for the three-angle electron beam evaporation. The sample is placed on a 45° angle tilt stage and 15 nm (165 nm) of Cr (Au) is deposited at a rate of 3.2 (4.0 Angstroms/s), while maintaining temperatures in the evaporator below 50

°C and pressures below 10^{-5} torr. We then rotate the sample by precisely 180° on the 45° angle tilt stage, and evaporate Cr/Au again. A final evaporation of 10 nm Cr and 100 nm Au is performed without the use of the tilt stage. The *1E*, *2E* and three-angle evaporation processes are shown in figure 3.4. Finally, the chip is removed from the evaporator and the metal is lifted off in PG remover for two hours at 60 °C. The chip is rinsed seven times in beakers with IPA before drying in a critical point dryer (CPD). Drying in a CPD dramatically improves device yield, as it replaces the IPA with liquid carbon dioxide (LCO_2), which is then brought past its critical point such that maximal surface tension is eliminated. It is important to reduce surface tension to prevent the thin top gate structure from collapsing as the liquid is dried. High quality LCO_2 is used to reduce the introduction of impurities to the sample. The critical point dryer used in this work is the AutoSamdri 815B Series A, by the Tousimis Research Corporation.
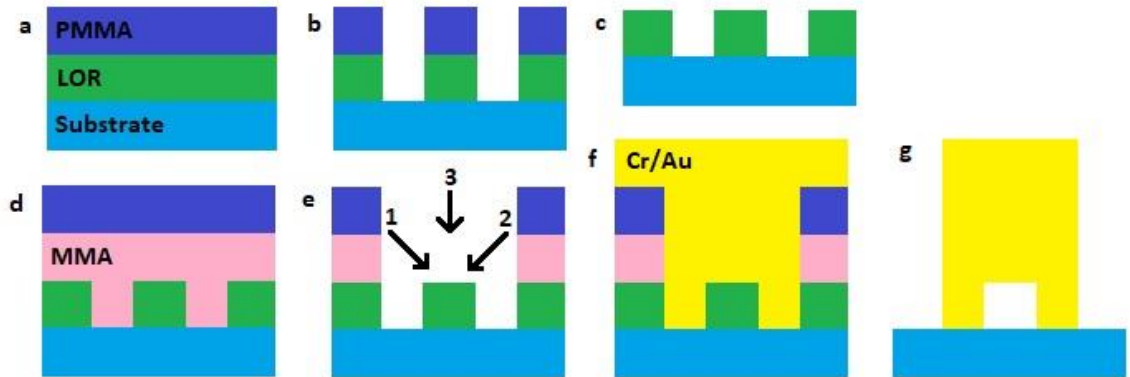
Figure 3.4. Schematic of 1E and 2E lithographic steps with three-angle electron beam evaporation: (a) LOR (green) is first spun and baked onto the SiO$_2$ substrate (light blue), followed by PMMA (dark blue). (b) Next, the first pattern (1E step) is exposed on the sample, and developed. (c) The top-most PMMA layer is removed with acetone, and (d) a new layer of MMA (pink) and PMMA (dark blue) are spun and baked on the sample again. (e) Next, the sample is exposed once again (2E step), to prepare for the three-angle electron-beam evaporation. (f) Chromium and gold metal (yellow) are evaporated onto the sample from three difference incident angles. (g) Finally, lift off in PG remover removes all resists. The end-result is a suspended, contactless top gate.

3.3.4 Split top gates

Another device design that I developed is suspended split top gates. The fabrication process for split top gates is identical to that of a single, suspend top gate. However, split top gates require extremely precise electron beam dosages, and the split top gates are much less robust, with weaker anchors. A minimum separation between the two split top gates was determined to be about 700 nm; separations less than 700 nm typically resulted in over-exposure of the top gate bridges and anchors due to EBL proximity effects. Furthermore, the surface area of the top gate anchors are also reduced were reduced as well to prevent shorting due to EBL proximity effects. Scanning electron microscope images of split top gates are shown in figure 3.5.
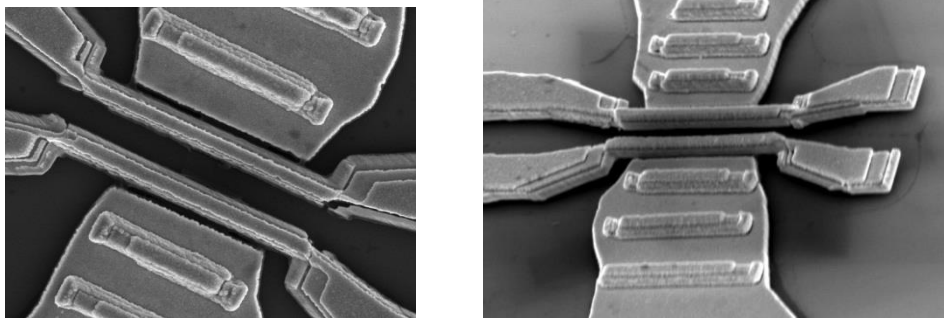
Figure 3.5. SEM image of suspended, split top gates: (a) Overhead image of suspended split top gates which shows the deposited metal is not shorted to the electrodes. (b) Tilted image of suspended split top gates shows that the top gates are indeed suspended above the graphene layer.

3.3.5 Source and drain electrodes

The final process in the EBL procedure is the fabrication of the source and drain electrodes, lithographic step *3E*. In this step, we use MMA and PMMA bilayer as resists. After the electron beam exposure, and development in MIBK:IPA (3:1), 15 nm of chromium and 150 nm of gold are evaporated onto the sample. Chromium and gold are chosen because they do not react with HF, which will be used in the next step to suspend the graphene. Chromium acts as a sticking or wetting layer, since gold by itself does not adhere well to the SiO_2 substrate. Gold is used instead of chromium only, because it conducts well and because thick layers of chromium tend to crack and flake apart. A large thickness of 150 nm of gold is chosen to reduce the probability of gate leakage during wire bonding.

3.3.6 Suspending the graphene membranes

Wet etching with a buffered oxide etch (BOE) is used to suspend the graphene. The BOE solution used comprises of a 6:1 volumetric ratio of 40% ammonium fluoride (NH_4F) in deionized water to 49% hydrofluoric acid (HF) in deionized water. After the final metal evaporation of source and drain top gates, the device is placed in acetone at room temperature or heated to 65 °C in order to lift off the resist. While the sample is still submerged in acetone, it is brought directly into IPA without drying, and rinsed in seven small beakers, each containing about 60 mL of IPA. Next, the samples are submerged in a 6:1 BOE solution for 70 seconds, so as to release the graphene flake from the SiO_2 substrate. After the etching is complete, the sample is again dried in a CPD. The resultant device is a suspended few-layer graphene field effect transistor device with dual gates, as shown in figure 3.6.
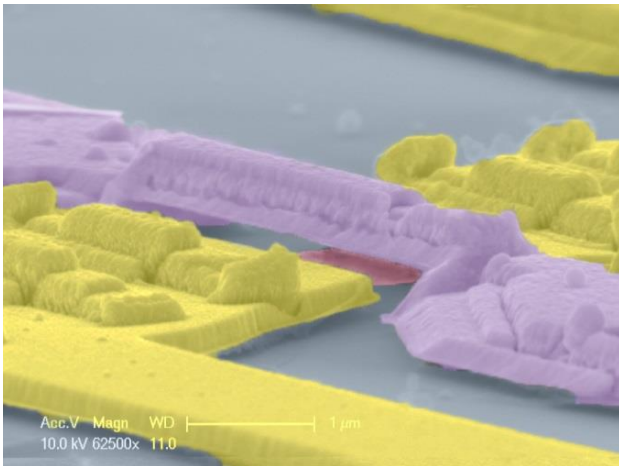
Figure 3.6. SEM image of doubly-suspended FLG device: False coloring is used to highlight features of the suspended, contactless top gate and the source-drain electrodes. The scale bar is 1 μm.

3.4   Post-fabrication annealing

After fabrication, the sample is wire bonded to a 16- or 20-pin chip carrier and cooled in a cryostat. Before measurements, the sample must first be annealed and characterized.

3.4.1 Current annealing

As-fabricated devices are contaminated with resist residues that introduce significant scattering and doping, thus typically have initially very low mobility and large minimum conductance. To improve device quality by removing impurities, we perform current annealing, during which a relatively large DC current density through the sample generates sufficient Joule-heating to burn off impurities.

To perform current annealing, we load a suspended graphene device on a chip carrier into a He3 or He4 cryostat, lowering the sample temperature to about 1.5K, and pumping out the sample space to a rough vacuum. We apply a DC voltage to the sample and measure its current. The current-voltage (I-V) characteristics are plotted while the bias is slowly ramped up at speeds of 5-15 mV/s and stopped when the I-V curve becomes sublinear and begins to saturate, as shown in Figure 3.7a. Current saturation usually occurs at a current density of ~ 0.2-0.4 mA/μm/layer. Usually the sample is moderately resistive immediately following fabrication (2-5 kΩ) and has little or no gate response. After several current annealing cycles, rhombohedral-stacked graphene devices are much more resistive (>200 kΩ) or insulating and display a characteristic V-shaped conductance (G) vs back gate (V_{BG}) curve, as shown in Figure 3.7b.
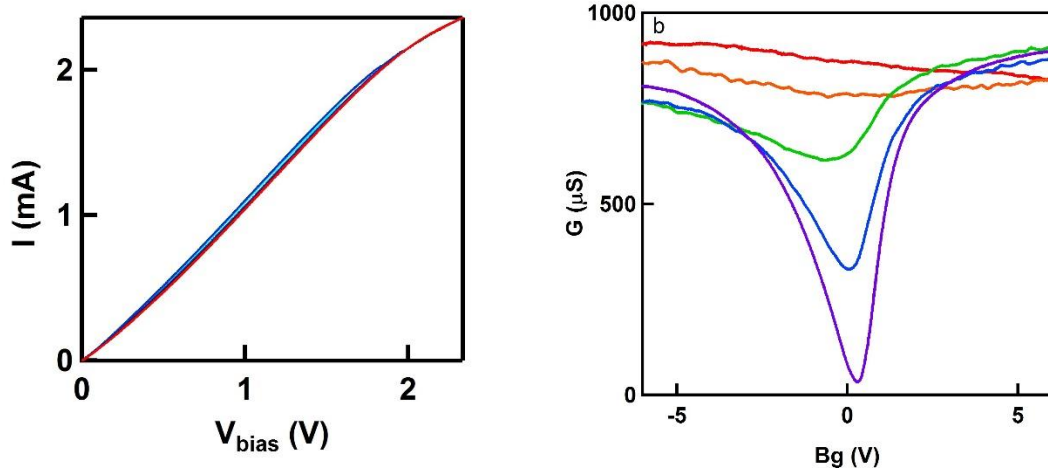
Figure 3.7. Current-annealing a suspended r-4LG device: (a) *I-V* curve of five annealing cycles. The *I-V* curve becomes sublinear at high voltage biases. (b) *G(V_{BG})* curves after each of five different current annealing cycles. The red, orange, green, blue and purple curves correspond to the first, fourth, fifth, seventh and eighth current annealing cycles.

3.4.2 Calculation of field effect mobility

A metric to characterize the device performance is its electronic field effect mobility, μ, as defined as

$$\mu = \frac{\sigma}{ne} = \frac{\sigma}{V_{BG}}\left(\frac{1}{C_{BG}^A e}\right) = \frac{\Delta G}{\Delta V_{BG}} \bullet \frac{L}{W} \bullet \left(\frac{1}{C_{BG}^A e}\right) \qquad (3.1)$$

where σ, n, C_{BG}^A and e are the conductivity, charge carrier density, capacitance per area between the graphene and the back gate, and electron charge, respectively. The value dG/dV_{BG} is simply the slope of a $G(V_{BG})$ curve, L/W is the aspect ratio of the sample, and C_{BG}^A is given by:

$$C_{BG}^A = \frac{C_P}{A} \qquad (3.2)$$

where A is the area and C_P is the capacitance of two sets parallel plate capacitors in series, given by:

$$\frac{1}{C_P} = \frac{1}{C_1} + \frac{1}{C_2} = \frac{d_1}{\kappa_1 \varepsilon_1 A} + \frac{d_2}{\kappa_2 \varepsilon_2 A} \qquad (3.3)$$

Here, C_1 is the capacitance of the air gap beneath the graphene with height d_1, and $\kappa_1 = 1$ for air. C_2 is the capacitance of the remaining, unetched SiO$_2$ with thickness d_2 and $\kappa_2 = 3.9$. For typical devices, $d_1 \sim 130$ nm and $d_2 \sim 170$ nm, thus $C_{BG}^A = 51 \, aF/\mu m^2$. This results in a charge carrier density in these fabricated samples of:

$$n = \frac{C_{BG}^A}{e}(V_{BG} - V_{BG}^D) = (3.1 \ x \ 10^{10} \ V^{-1} cm^{-2})(V_{BG} - V_{BG}^D). \qquad (3.4)$$

The range of back gate chosen for mobility calculation is typically $\sim (V_{BG}{}^D, V_{BG}{}^D + 3V)$, or similarly the carrier density range is $\sim (0, +10^{11} \text{ cm}^{-2})$, where $V_{BG}{}^D$ is the back gate voltage at which the conductance minimum is observed. Typically, mobility is calculated on the electron-side (positive gate voltage).

If a device is not imaged in an SEM prior to measurement (thus d_1 and d_2 are undetermined), then we can estimate the capacitance using the experimentally measured Landau fan. In a magnetic field, quantized plateaus are observed at integer filling factors ν,

$$\nu = \frac{nh}{Be} = C_{BG}^A \frac{(V_{BG} - V_{BG}^D)h}{Be} \qquad (3.5)$$

Therefore, the slope V_{BG}/B at a given filling factor determines the back gate capacitance per area C_{BG}^A. When plotting G as a function of V_{BG} and B, these quantum Hall states appear as a fan radiating from $n = B = 0$. We typically plot $G(V_{BG}, B)$ or the differentiated

conductance $\frac{dG(V_{BG}, B)}{dV_{BG}}$ (the latter accentuates the features), and measure the slopes of the

QH states on the *n-B* plane.

3.5   Conclusion and references

In this chapter, we discussed the how FLG samples are prepared by scotch tape exfoliation, characterized by optical contrast and Raman spectroscopy, and fabricated with EBL. The intricate steps of the fabrication recipe were described, including: spinning electron beam resists, writing alignment marks, dry etching the graphene flakes, multi-step EBL processes and electron beam evaporations to define suspended top gates and contact electrodes, and suspending the FLG membrane with wet etching and drying in a CPD. We also included SEM images of fabricated devices, which show the FLG membranes suspended above the substrate, with a suspended, contactless top gate that does not short to the source-drain contacts. Furthermore, we described some details of the post-fabrication annealed process, which leads to high mobility samples by burning off impurities, and provided geometrical calculations of the field effect mobility in our devices.

References

1. Liu, G., Velasco, J., Bao, W., & Lau, C. N. Fabrication of graphene p-n-p junctions with contactless top gates. *Appl. Phys. Lett.* **92**, 203103 (2008).

2. Novoselov, K. S., Geim, A. K., Morozov, S. V., Jiang, D., Zhang, Y., Dubonos, S. V., Grigorieva, I. V. & Firsov, A. A. Electric field effect in atomically thin carbon films. *Science*. **306**, 666-669 (2004).

3. Ni, Z. H., Wang, H. M., Kasim, J., Fan, H. M., Yu, T., Wu, Y. H., Feng, Y. P. & Shen, Z. X. Graphene thickness determination using reflection and contrast spectroscopy. *Nano Lett*. **7** (9), 2758-2763 (2007).

4. Graf, D., Molitor, F., Ensslin, K., Stampfer, C., Jungen, A., Hierold, C. & Wirtz, L. Spatially resolved Raman spectroscopy of single- and few-layer graphene. *Nano Lett*. **7**, 238 (2007).

5. Cong, C., Yu, T. & Wang, H. Raman Study on the G mode of graphene for determination of edge orientation. *ACS Nano.* **4** (6), 3175-3180 (2010).

6. Thomsen, C. & Reich, S. Double resonant Raman scattering in graphite. *Phys. Rev. Lett*. **85** (24), 5214-5217 (2000).

7. Ferrari, A. C. Raman spectroscopy of graphene and graphite: Disorder, electron-phonon coupling, doping and nonadiabatic effects. *Solid State Commun*. **143**, 47-57 (2007).

8. Lui, C. H., Li, Z., Chen, Z., Klimov, P. V., Brus, L. E., & Heinz, T. F. Imaging stacking order in few-layer graphene. *Nano Lett.*, **11**, 164-169 (2011).

9. Cong, C., Yu, T., Sato, K., Shang, J., Saito, R., Dressellhaus, G. F. & Dressellhaus, M. S. Raman characterization of ABA- and ABC-stacked trilayer graphene. *ACS Nano*, **5**, 8760 (2011).

10. Nguyen, T. A., Lee, J.-U., Yoon, D. & Cheong, H. Excitation energy dependent Raman signatures of ABA- and ABC-stacked few-layer graphene. *Sci. Rep*. **4**, 4630 (2014).

11. Lau, C. N., Liu, G., & Velasco Jr., J. U.S. Patent 7,948,042 B2 (2011).

Chapter 4: In situ observation of electrostatic and thermal manipulation of suspended graphene membranes

4.1   Introduction

Suspended graphene membranes enable the investigation of its intrinsic mechanical, electrical, optical, and thermal properties, such as unparalleled breaking strength[1,2], wrinkling instability[3-5], observation of the fractional quantum Hall effect[6-8], states with spontaneous broken symmetries[9-14], ultrahigh thermal conductivity[15] and negative thermal expansion coefficient[4]. Thus, many of graphene's intrinsic properties are only revealed via the study of suspended devices[16]. However, as an elastic membrane, graphene deforms readily, with an intricate relation between its morphology and electrical properties[17-22]. Thus, *in situ* studies of graphene's deformation under externally controlled parameters are critical for an in-depth understanding of suspended graphene membranes.

In this chapter, we report in situ observation of thermally and electrostatically induced morphological deformation of graphene membranes that are suspended across trenches. Under applied gate voltage, the graphene membrane deforms to adopt a nearly parabolic profile with a vertical displacement as large as 200 nm for a 3 μm-long trench. Interesting, unclamped membranes slide under tension into the trenches. During cooling, due to their large negative thermal expansion coefficient[4], graphene membranes buckle, forming periodic ripples with large deflections of the free edges. As these distortions are expected to have significant impact on graphene's electrical properties[17-22], our results will be important for understanding electrical, thermal, and mechanical properties of

suspended graphene devices, as well as paving the way for rational engineering of graphene using local strain and morphology.

4.2   Device fabrication

The device fabrication method in this work[23] differs from the doubly-suspended fabrication recipe described in the previous chapter. Here, suspended graphene membranes are prepared by the standard mechanical cleave technique on Si/SiO$_2$ wafers with prepatterned trenches, as shown in figure 4.1a. Membranes that are 1, 2 and 3 layers thick are identified by color contrast in an optical microscope and/or using Raman spectroscopy. The trenches are defined by photolithography followed by plasma etching in a reactive ion etcher (RIE) system. The SiO$_2$ layer is 300 nm thick with trench depth and length of d_1 = 250 nm and $L \sim 3.0 - 3.3$ μm, respectively. Typically, narrow and rectangular-shaped graphene sheets with widths W less than 1 μm are selected by directly depositing Ti/Au metal electrodes through shadow masks[24]. Two types of devices are fabricated: (1) the graphene sheet is clamped by two metal electrodes that are deposited ~1 μm from the edges of the trench (figure 4.1b), and (2) the graphene sheet is unclamped with one of its ends contacted by a metal electrode placed ~ 10 mm away from the trench edge (figure 4.2a).
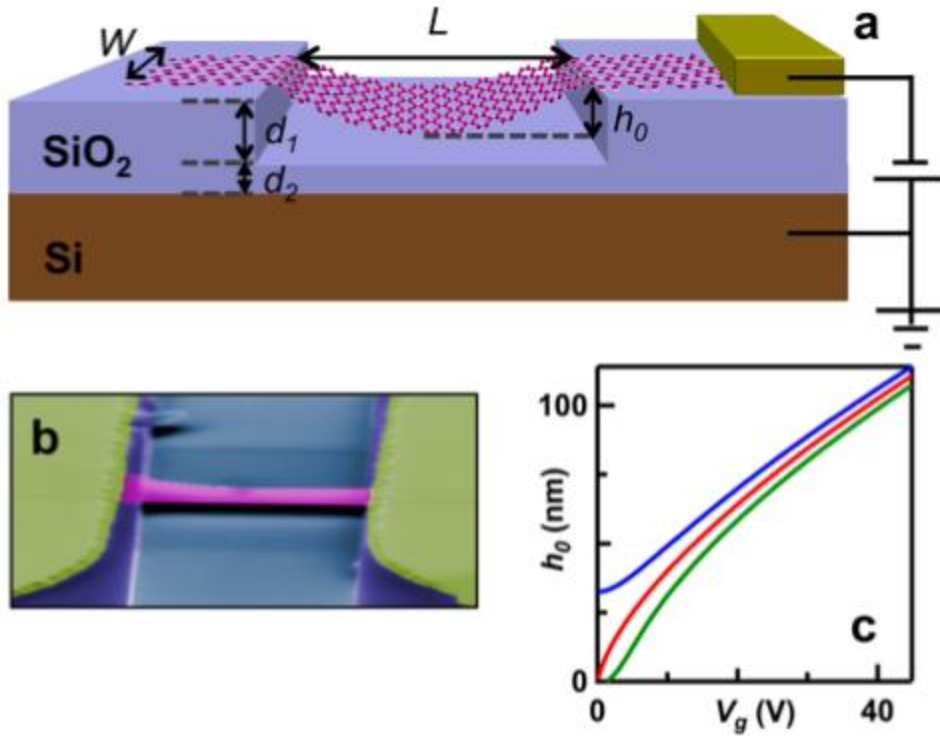
Figure 4.1. Device schematic, SEM and $h_0(V_g)$: (a) Schematic diagram of the deflection of a graphene membrane under V_g. (b) SEM image of a doubly clamped graphene device. All trenches in this work have L ~ 3.0–3.3 μm. (c) Vertical deflection h_0 calculated from equation 4.1, using $\Delta L = 0$ (red), -1 nm (blue), and 1 nm (green), respectively. Images taken from ref. 23.

4.3   Electrostatic manipulation

Graphene's deformation under electrostatic force can be modeled as a thin film that is doubly clamped at x = -L/2 and x = L/2; under a uniform P in the out-of-plane direction, it deflects and adopts a parabolic profile. Because of its extremely small thickness, graphene is almost always in the large deflection limit with maximum deflection h_0 at $x = 0$ given by the equation[25-27]

$$PL^2 = 8T_0 t h_0 + \frac{64}{3}\frac{Et}{L^2(1-v^2)}h_0{}^3 \tag{4.1}$$

49

where $t \approx 0.34$ nm per layer is the thickness, and E is the Young's modulus. v is the Poisson ratio and is predicted to range from 0.1 to 0.3 for SLG[28,29]. Here, we use $v = 0.165$, the value for graphite in the basal plane[30]. $T_0 = [E/(1 - v^2)](\Delta L/L)$ is the pre-existing stress in the membrane at $P = 0$, leading to relative elongation DL that can be either positive (tension) or negative (slack). In our experiments, the electrostatic pressure is $P = (C^2 V_g^2)/(2\varepsilon_0)$, where C is the capacitance per unit area between graphene and the gate, and ε_0 is the permittivity of vacuum.

The formulation of equation 4.1 neglects the additional elastic energy required to bend the graphene sheet to a finite radius of curvature, because when using continuum elasticity, this bending energy can be shown to be much smaller than the stretching of energy of equation 4.1. For a finite-thickness continuum sheet, this energy ratio is negligibly small by a factor of $\sim (t/h_0)^2$. For single layer graphene (SLG), the elastic bending energy is alternatively modeled in terms of its bending rigidity, which is expected to lie in the range $\kappa \approx 1.1$ eV[26] to ~ 7 eV[31], in which case the energy ratio is $\sim (9\kappa/Eth_0^2)$ and again is safely neglected for any reasonable vale of $h_0 > 1$ nm. We also consider the effect of ripples acting as corrugations which increase the bending stiffness. For sinusoidal ripples of amplitude A, the energy ratio now scales as $\sim (A/h_0^2)$ and can be neglected for the experiments reported here (typical $h_0 \sim 20$–200 nm and $A \sim 1$–10 nm)[4].

For the vast majority of works on suspended graphene, one makes the approximation of parallel plate geometry between graphene and the gate, in which case h_0 can be calculated by solving the equation

$$\frac{\varepsilon_0}{2}\left(\frac{\varepsilon_r}{\varepsilon_r d_1 + d_2}\right)^2 V_g^2 L^2 = 8T_0 t h_0 + \frac{64}{3}\frac{Et}{L^2(1-v^2)}h_0^3 \qquad (4.2)$$

where $d_1 = 250$ nm is the depth of the trench, $d_2 = 50$ nm is the thickness of the residual

SiO_2 at the bottom of the trench, and, $\varepsilon_r \sim 3.9$ is the dielectric constant of SiO_2. Figure

4.2c plots the calculated h_0 for SLG as a function of V_g, using $L = 3.1$ μm, $E = 1$ TPa, and

$\varDelta L = 0$ (red), -1 nm (blue), and 1 nm (green), respectively. Noticeably, even a miniscule

strain (~0.03%) results in significant variation in h_0 at small V_g; at large V_g, all three

curves approach the asymptotic value $h_0 = [(3/64)\,(PL^4)/(Et)]^{1/3}$, which is sublinear

in V_g.

   To experimentally study the deflection, we perform in situ SEM imaging while

applying V_g to the devices. A series of images taken at 85° tilt angle for an unclamped

device at different V_g is shown in figure 4.2a–d. At $V_g = 0$, the graphene membrane

appears to be flat and taut across the trench. As V_g is increased, the graphene deflects

toward the gate, and adopts a parabolic profile. From the SEM images, we can readily

measure h_0, which increases with V_g and reaches ~ 200 nm at $V_g = 30$ V. When V_g is

returned to zero from 30 V, graphene reverts to its flat state with little or no slacking.

Indeed, we observe minimal hysteresis in h_0 when V_g is swept up and down between 0

and ± 30 V (figure 4.2e), which suggests that the deflection is elastic and reversible. At

sufficiently large V_g, the graphene sheet irreversibly collapses to the bottom of the trench

(figure 4.2f), with ripples in the highly strained regions that bridge the trenches' banks

and bottom[4].
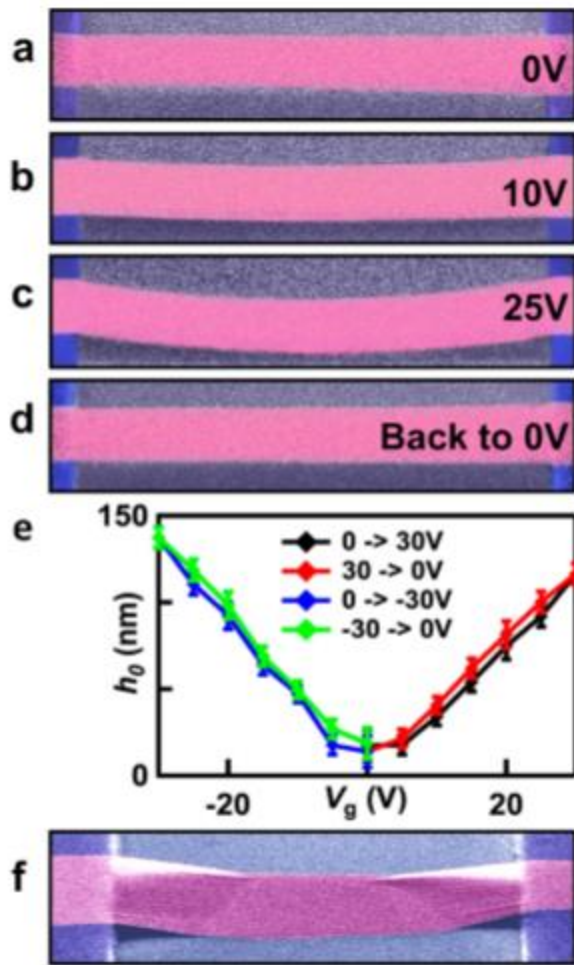
Figure 4.2. SEM images and $h_0(V_g)$ measurement: (a) A series of SEM images taken at 85o tilt angle for an unclamped SLG device at different V_g = 0, 10, 25, and back to 0 V, respectively. (e) Minimal hysteresis in h_0 of an unclamped TLG device as V_g sweeps between 0 and ± 30 V. (f) An SEM image showing a graphene sheet collapse to the bottom of the trench at sufficiently large V_g (here V_g = 40 V). Images taken from ref. 23.

The measured values of h_0 at V_g ranging from 0 to 45 V for unclamped devices

are shown as blue triangles in figure 4.3. The three panels correspond to single layer

(SLG), bilayer (BLG), and trilayer graphene (TLG) devices, respectively. For

comparison, h_0 calculated from equation 4.2 is plotted as green dotted lines, using

experimentally determined values of L. To account for the curvature of h_0 in SLG at low V_g, T_0 is obtained from fitting to be 10^8 Pa; $T_0 = 0$ for BLG and TLG devices (in general, we find that T_0 is sample-dependent, presumably due to variations in the exfoliation and fabrication process). The experimental data are in reasonable agreement with equation 4.2 at low V_g but deviate significantly for $V_g > 15$ V, becoming superlinear in V_g.
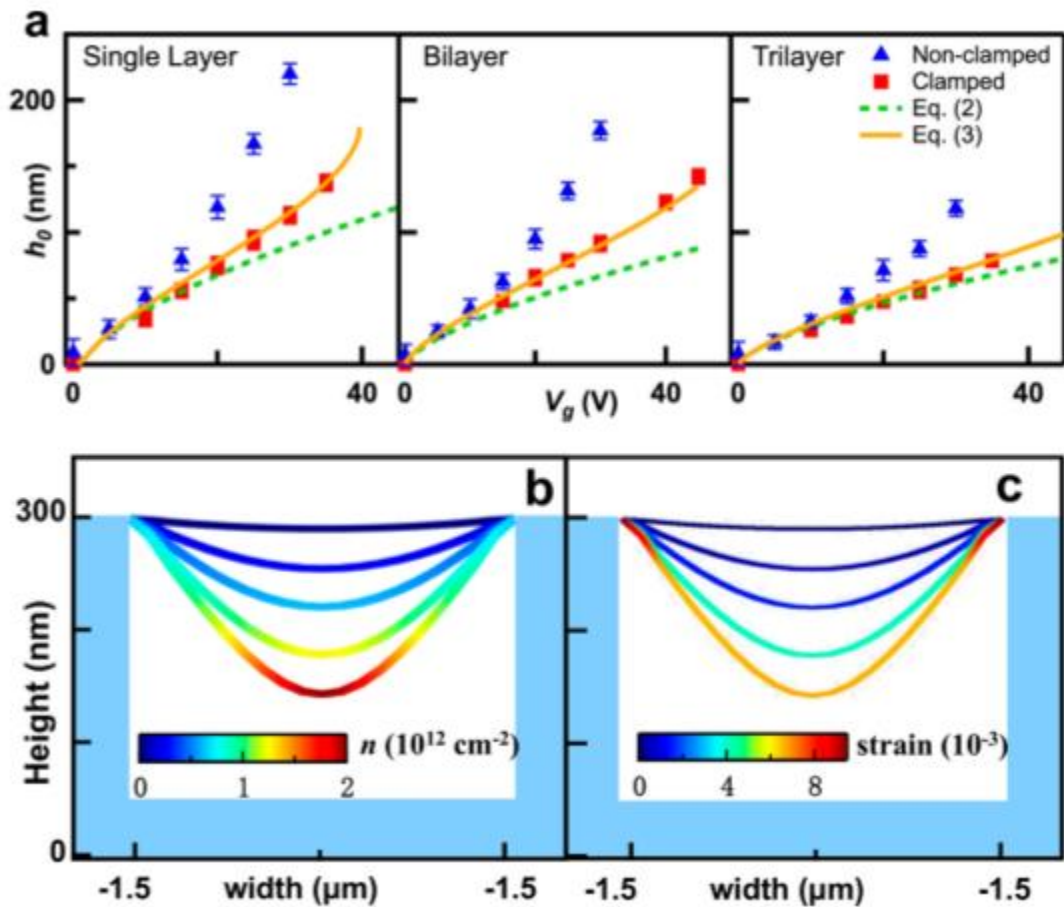
Figure 4.3. Electrostatic gate deflection $h_0(V_g)$ for suspended SLG, BLG and TLG devices, and simulation data of suspended SLG: (a) $h_0(V_g)$ for single layer, bilayer, and trilayer suspended graphene devices, respectively. The symbols are experimental data and the dotted and solid lines are calculated using equations 4.2 and 4.3, respectively. (b,c) Simulation showing nonuniform distribution of charge density and strain distribution (from top to bottom: $V_g = 1, 10, 20, 30$, and 33.8V). Here, $T_0 = 0$. Images are taken from ref. 23.

The same trend is observed for all devices with larger discrepancy for thinner sheets.

The failure of equation 4.2 to account for the data prompts us to consider the possibility of the graphene sheet sliding into the trench under tension. To test this hypothesis, we revise the device geometry by depositing electrodes on graphene near the trench edges. Deflection data obtained from these doubly clamped devices (red squares in figure 4.3a) are notably smaller than the unclamped counterparts and are much closer to the calculated values. Taken together, these data indicate that under tension induced by the electrostatic pressure, the substrate-supported portion of unclamped graphene may slide into the trench, thus giving rise to increased deflection. Remarkably, this process appears to be elastic and reversible, since upon reducing V_g to 0, h_0 returns to < 15 nm (figure 4.2a–e). Further works with similar experiments might enable one to study the layer dependence and substrate dependence of friction between graphene and the substrate[32].

On the other hand, the sliding of graphene membranes under tension can only partially account for the discrepancy between the measured and calculated deflection values from equation 4.2. In particular, the experimental data are superlinear, whereas the calculated curves are sublinear. To elucidate this discrepancy, we note that, at large V_g, graphene adopts a parabolic profile, and hence the approximation of parallel plate electrostatics used in equation 4.2 is no longer valid. Instead, the capacitance between graphene and the top of the residual SiO_2 layer is modified to

$$C = \frac{\varepsilon_0}{\sqrt{h_0(d_1-h_0)}} \tan^{-1}\left(\sqrt{\frac{h_0}{d_1-h_0}}\right) \tag{4.3}$$

Thus, by combining equations 4.1 and 4.3, and taking into account the series capacitance of the SiO_2 layer, we self-consistently solve for $h_0(V_g)$ using E as a fitting parameter. The results, which are calculated using E = 1.10 TPa (SLG), 0.98 TPa (BLG), and 1.17 TPa (TLG), are plotted as solid lines in figure 4.3a. Again, T_0 are obtained to be ~ 10^8 Pa for SLG and 0 otherwise. The new curves are in very good agreement with experimental data; the value of Young's modulus for graphene is determined to be E = 1.08 ± 0.1 TPa, similar to that reported previously[1,2]. Our results also agree with the numerical analysis in ref. 26. We also note that equation 4.2, which is based on the common assumption of parallel-plate geometry, is in reasonably good agreement with SLG data for V_g < 15 V and with TLG data for V_g < 35 V.

Further insight into the deflecting membrane can be achieved by using COMSOL, a finite element simulation software, to model the inhomogeneous charge density distribution (n) that arises from the large deformation of the graphene sheet at high V_g and in turn alters the profile of the sheet. Figure 4.3b,c plots the spatial map of n and strain at different V_g. Both become notably inhomogeneous at high V_g: n reaches its maximum at the center of the deformed graphene sheet, while the strain is maximum at the clamped boundaries. These results should be important for understanding and interpreting transport and nanoelectromechanical data of suspended graphene devices.

4.4   Strain-induced rippling effects

Thus far we only considered flat suspended graphene membranes. On the other hand, many devices contain ripples. Such ripples are a consequence of graphene's extremely small buckling energy and readiness to deform and can result from either tensile or compressive strain[4]. Since these long-wavelength ripples are smooth on the atomic scale, they are expected to have negligible effect on graphene's intrinsic mechanical properties such as Young's modulus and Poisson's ratio, and, as noted above, the effect of corrugations in increasing the bending stiffness is also negligible in these experiments. Conversely, these ripples and strains are expected to strongly impact the electronic properties of graphene. Here, we investigate the effect of gating on graphene membranes containing strain-induced ripples. Figure 4.4a displays the SEM image of an unclamped device with oblique ripples, and electrodes that are deposited ~ 1.5 μm away from the trench. Under applied V_g, in addition to the out-of-plane deflection of the entire sheet, the wavelength of the ripples λ decreases (figure 4.4b,c). Such a phenomenon is expected from the classical elasticity theory, $\lambda^4 \, \alpha \, \gamma^{-1}$, where γ is the longitudinal tensile, which increases with $V_g{}^4$. Furthermore, V_g also changes the orientation of the ripples from oblique to normal to the edges of the trench, which could be explained by the partial sliding of the substrate-supported region of graphene. However, when metal contacts extend onto the suspended portion of graphene, as shown in figure 4.4d,e, the ripples are pinned by the electrodes, and varying V_g has a much weaker effect on the morphology of the graphene ripples.
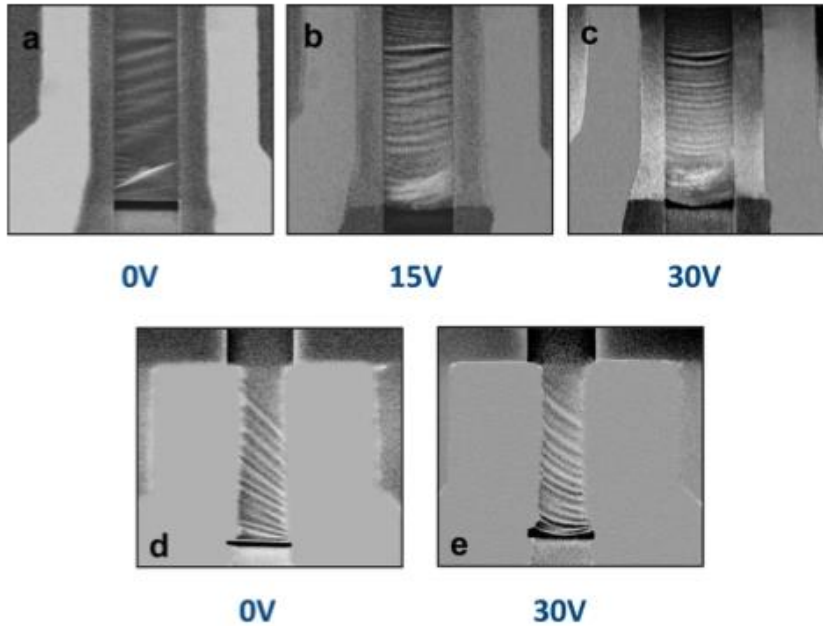
Figure 4.4. SEM images of suspended graphene devices: (a-c) SEM images of a partially clamped suspended graphene device with ripples at V_g = 0, 15, and 30 V, respectively. Electrodes are placed ~ 1.5 μm from the trench edges. (d,e) SEM images of a fully clamped suspended graphene device with oblique ripples at different V_g = 0 and 30 V, respectively. The ripples are fully clamped by electrodes that extend over the graphene. Images are taken from ref. 23.

4.5   Thermal maniuplation

We now examine the effect of low temperature on graphene membranes' morphology. Despite extensive low-temperature transport measurements on suspended graphene devices, direct observation of their morphology at low temperature has been lacking. Using an SEM cold stage, we perform in situ SEM imaging for relatively wide (W > L) graphene sheets at room temperature and at 100 K. Figure 4.5 shows that a graphene sheet that is originally flat at room temperature becomes rippled at 100 K. These ripples arise from the compressive strain induced by graphene's negative thermal

expansion coefficient (TEC) and its substrate-pinned edges. Graphene's expansion upon cooling can also induced the upward buckling of its two free edges, forming a 'butterfly' feature at two sides, as shown in figure 4.5b,c.
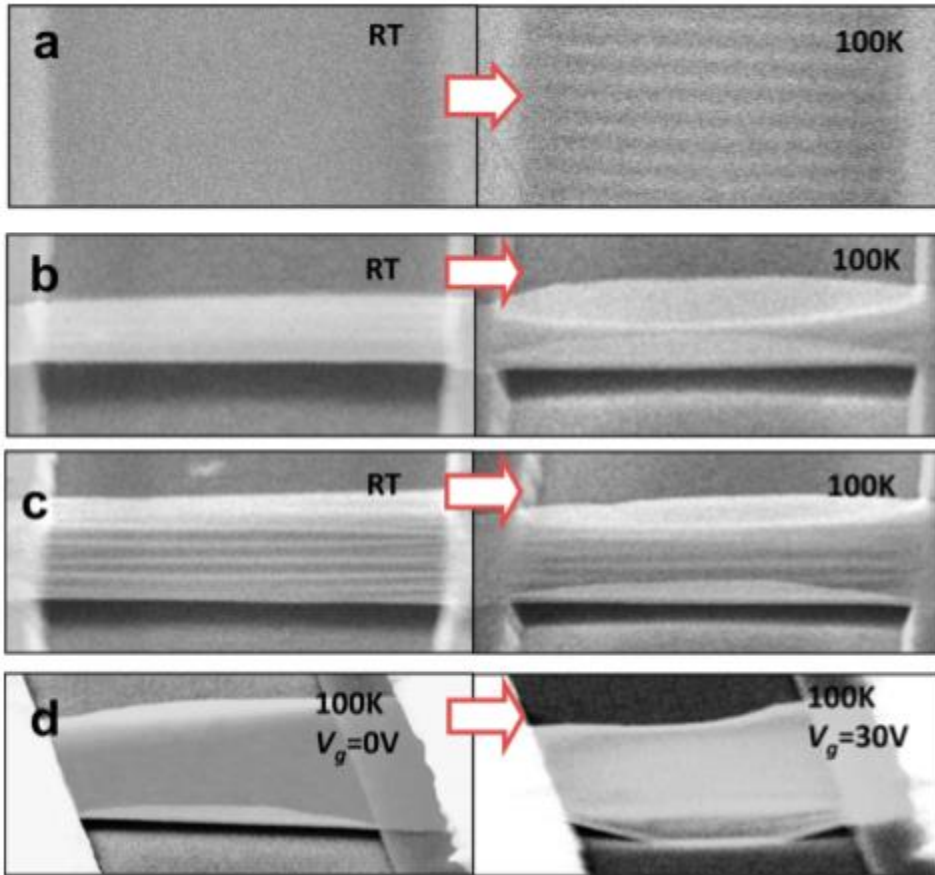
Figure 4.5. SEM images of suspended SLG devices at room temperature and 100 K using a cold SEM stage: (a-c) SEM images for $V_G = 0$ with devices at room temperature (left panels) and cooled to 100 K (right panels). (d,e) In situ SEM images with devices cooled to 100 K at $V_G = 0$ V (left panel) and 30 V (right panel). Images taken from ref. 23.

This observation readily enables us to estimate the lower bound of the magnitude of the TEC by measuring the length along the arc of the butterfly feature. We estimate that the average TEC between 100 K and room temperature is as large as $-2 \times 10^{-5} \, K^{-1}$ for

58

single layer graphene, consistent with previous measurements[4,33-35]. Lastly, when V_g is applied to a wide graphene device at low temperature, the expanded butterfly feature is pulled to the bottom of the trench, though the bulk of the sheet remains free-standing. Therefore suspended graphene membranes, particularly those with large aspect ratios (W/L $\gg$ 1), are prone to collapsing at low temperature.

4.6   Conclusion and references

To conclude, we observe significant deflections of SLG, BLG and TLG membranes sheets in response to electrostatic force, which is in agreement with a model for the deflection of a thin film with elastic constant ~ 1.1 TPa. Finite element analysis simulations indicate that charge carrier density and strain are highly inhomogeneous in the suspended graphene membranes, with maxima at the center and clamped edges of the graphene membrane, respectively. At low temperature, due to graphene's negative TEC, the central portion of a wide graphene sheet ripples and butterfly features form at its two free edges. Thus, these observations imply important applications for electrical, mechanical, thermal, and strain engineering in suspended graphene devices. Furthermore, these results of morphological deformation, inhomogeneous charge carrier density and strain, ripples and butterfly features should be taken into careful consideration when analyzing low temperature electronic transport data in suspended graphene field effect transistor devices.

References

1. Frank, I., Tanenbaum, D. M., Van der Zande, A. M., and McEuen, P. L. Mechanical properties of suspended graphene sheets. *J. Vac. Sci. Technol. B*, **25**, 2558-2561 (2007).

2. Lee, C., Wei, X. D., Kysar, J. W., and Hone, J. Measurement of the elastic properties and intrinsic strength of monolayer graphene. *Science*, **321**, 385-388 (2008).

3. Meyer, J. C., Geim, A. K., Katsnelson, M. I., Novoselov, K. S., Booth, T. J., and Roth, S. The structure of suspended graphene sheets. *Nature*, **446**, 60-63 (2007).

4. Bao, W., Miao, F., Chen, Z., Zhang, H., Jang, W. Y., Dames, C., and Lau, C. N. Controlled ripple texturing of suspended graphene and ultrathin graphite membranes. *Nat. Nanotechnol.*, **4**, 562-566 (2009).

5. Vandeparre, H., Pineirua, M., Brau, F., Roman, B., Bico, J., Gay, C., Bao, W., Lau, C. N., Reis, P. M., and Damman, P. Wrinkling hierarchy in constrained thin sheets from suspended graphene to curtains. *Phys. Rev. Lett.*, **106**, 224301 (2011).

6. Bolotin, K. I., Ghahari, F., Shulman, M. D., Stormer, H. L., and Kim, P. Observation of the fractional quantum Hall effect in graphene. *Nature*, **462**, 224301 (2011).

7. Du, X., Skachko, I., Duerr, F., Luican, A., and Andrei, E. Y. Fractional quantum Hall effect and insulating phase of Dirac electrons in graphene. *Nature*, **462**, 192-195 (2009).

8. Bao, W. Z., Zhao, Z., Zhang, H., Liu, G., Kratz, P., Jing, L., Velasco, J., Smirnov, D., and Lau, C. N. Magnetoconductance oscillations and evidence for fractional quantum Hall states in suspended bilayer and trilayer graphene. *Phys. Rev. Lett.*, **105**, 246601 (2010).

9. Mayorov, A. S., Elias, D. C., Mucha-Kruczynski, M., Gorbachev, R. V., Tudorovskiy, T., Zhukov, A., Morozov, S. V., Katsnelson, M. I., Fal'ko, V. I., Geim, A. K., and Novoselov, K. S. Interaction-driven spectrum reconstruction in bilayer graphene. *Science*, **333**, 860 (2011).

10. Martin, J., Feldman, B. E., Weitz, R. T., Allen, M. T., and Yacoby, A. Local compressibility measurements of correlated states in suspended bilayer graphene. *Phys. Rev. Lett.*, **105**, 256806 (2010).

11. Weitz, R. T., Allen, M. T., Feldman, B. E., Martin, J., and Yacoby, A. Broken-symmetry states in doubly gated suspended bilayer graphene. *Science*, **330**, 812-816 (2010).

12. Velasco, J., Jing, L., Bao, W., Lee, Y., Kratz, P., Aji, V., Bockrath, M., Lau, C. N., Varma, C., Stillwell, R., Smirnov, D., Zhang, F., Jung, J., and MacDonald, A. H. Transport spectroscopy of symmetry-broken insulating states in bilayer graphene. *Nat. Nanotechnol.*, **7**, 156-160 (2011).

13. Freitag, F., Trbovic, J., Weiss, M., and Schonenberger, C. Spontaneously gapped ground state in suspended bilayer graphene. *Phys. Rev. Lett.*, **108**, 076602 (2012).

14. Bao, W., Velasco, J., Zhang, F., Jing, L., Standley, B., Smirnov, D., Bockrath, M., MacDonald, A. H., and Lau, C. N. Evidence for a spontaneous gapped state in ultra-clean bilayer graphene. *Proc. Natl. Acad. Sci. U.S.A.*, **109**, 10802-10805 (2012).

15. Balandin, A. A., Ghosh, S., Bao, W., Calizo, I., Teweldebrhan, D., Miao, F., and Lau, C. N. Superior thermal conductivity of single-layer graphene. *Nano Lett.*, **8**, 902 (2008).

16. Lau, C. N., Bao, W., and Velasco, J. Properties of suspended graphene membranes. *Mater. Today*, **15**, 238-245 (2012).

17. Guinea, F., Horovitz, B., and Le Doussal, P. Gauge field induced by ripples in graphene. *Phys. Rev. B*, **77**, 205421 (2008).

18. Guinea, F., Katsnelson, M. I., and Vozmediano, M. A. Midgap states and charge inhomogeneities in corrugated graphene. *Phys. Rev. B*, **77**, 075422 (2008).

19. De Parga, A. L. V., Calleja, F., Borca, B., Passeggi, M. C. G., Hinarejos, J. J., Guinea, F., and Miranda, R. Periodically rippled graphene: Growth and spatially resolved electronic structure. *Phys. Rev. Lett.*, **100**, 056807 (2008).

20. Kim, E.-A. and Castro Neto, A. H. Graphene as an electronic membrane. *Europhys. Lett.*, **84**, 57007 (2008).

21. Katsnelson, M. I. and Geim, A. K. Electron scattering on microscopic corrugations in graphene. *Philos. Trans. R. Soc. London Ser. A.*, **366**, 195-204 (2008).

22. Morozov, S. V., Novoselov, K. S., Katsnelson, M. I., Schedin, F., Elias, D. C., Jaszczak, J. A., and Geim, A. K. Giant intrinsic carrier mobilities in graphene and its bilayer. *Phys. Rev. Lett.*, **100**, 016602 (2008).

23. Bao, W., Myhro, K., Zhao, Z., Chen, Z., Jang, W., Jing, L., Miao, F., Zhang, H., Dames, C., and Lau, C. N. In situ observation of electrostatic and thermal manipulation of suspended graphene membranes. *Nano Lett.*, **12**, 5470-5474 (2012).

24. Bao, W., Liu, G., Zhao, Z., Zhang, H., Yan, D., Deshpande, A., LeRoy, B., and Lau, C. N. Lithography-free fabrication of high quality substrate-supported and freestanding graphene devices. *Nano Res.*, **3**, 98-102 (2010).

25. Lifshitz, E. M. and Landau, L. D. Theory of Elasticity, 3rd ed., Butterworth-Heinemann: Woburn, MA, **7**, 25 (1986).

26. Fogler, M. M., Guinea, F., and Katsnelson, M. I. Pseudomagnetic fields and ballistic transport in a suspended graphene sheet. *Phys. Rev. Lett.*, **101**, 226804 (2008).

27. Medvedyeva, M. V. and Blanter, Y. M. Piezoconductivity of gated suspended graphene. *Phys. Rev. B*, **83**, 045426 (2011).

28. Zakharchenko, K. V., Katsnelson, M. I., and Fasolino, A. Finite temperature lattice properties of graphene beyond the quasiharmonic approximation. *Phys. Rev. Lett.*, **102**, 046808 (2009).

29. Scarpa, F., Adhikari, S., and Phani, A. S. Effective elastic mechanical properties of single layer graphene sheets. *J. Nanosci. Nanotechnol.*, **20**, 065709 (2009).

30. Blakslee, O. L., Proctor, D. G., Seldin, E. J., Spence, G. B., and Weng, T. Elastic constants of compression-annealed pyrolytic graphite. *J. Appl. Phys.*, **41**, 3373-3382 (1970).

31. Lindahl, N., Midtvedt, D., Svensson, J., Nerushev, O. A., Lindvall, N., Isacsson, A., and Campbell, E. E. B. Determination of the bending rigidity of graphene via electrostatic actuation of buckled membranes. *Nano Lett.*, **12**, 3526-3531 (2012).

32. Koenig, S. P., Boddeti, N. G., Dunn, M. L., and Bunch, J. S. Ultra-strong adhesion of graphene membranes. *Nat. Nanotechnol.*, **6**, 543 (2011).

33. Chen, C.-C., Bao, W., Theiss, J., Dames, C., Lau, C. N., and Cronin, S. B. Raman spectroscopy of ripple formation in suspended graphene. *Nano Lett.*, **9**, 4172-4176 (2009).

34. Singh, V., Sengupta, S., Solanki, H. S., Dhall, R., Allain, A., Dhara, S., Pant, P., and Deshmukh, M. M. Probing thermal expansion of graphene and modal dispersion at low-temperature using graphene nanoelectromechanical systems resonators. *J. Nanosci. Nanotechnol.*, **21**, 165204 (2010).

35. Yoon, D., Son, Y. W., and Cheong, H. Negative thermal expansion coefficient of graphene measured by Raman spectroscopy. *Nano Lett.*, **21**, 165204 (2010).

Chapter 5: Spontaneous and induced insulating states in rhombohedral-stacked bilayer and trilayer graphene

5.1   Introduction

In this chapter, we will begin by motivating the use of suspended structures, including both the few-layer graphene (FLG) membranes and the suspended top gates. We will discuss the independent tuning of the out-of-plane electric field and charge carrier density in the sample, which can only be achieved by dual-gating. Next, we will discuss the origin of the single particle gap in bilayer graphene (BLG), and show transport data in moderate and high mobility suspended BLG devices with electric field tuning. Furthermore, we will show results of probing a spontaneous insulating state in BLG, and discuss its nature. We will also show results for the tuning of the intrinsic gap in high mobility rhombohedral-stacked trilayer graphene (r-TLG) devices as a function of carrier density, temperature, electric and magnetic fields. Finally, we will discuss the nature of the ground state of r-TLG at low temperature.

5.2   The importance of suspended structures

"Doubly-suspended" refers to the FLG membranes suspended above the dielectric layer and below the top gate, as shown in figure 3.6 from chapter three. Several research groups have reported high electronic mobility in suspended single layer graphene[1-3] (SLG), FLG[4-6] and symmetry-broken insulating states in doubly-suspended FLG with suspended top gates[4,7-9], making the suspension of SLG, FLG and top gates an invaluable method for probing 2D materials.

Exfoliating graphene directly onto an SiO_2 or SiC substrate typically results in moderate device mobility ranging from 1,000 to 10,000 cm^2/Vs, although these numbers are still relatively low compared to that can be achieved in suspended devices[1,4,10,11] or devices supported on or encapsulated within hexagonal boron nitride (hBN) layers[12-15]. hBN-supported graphene devices are more robust, though the presence of a substrate increases screening, so that the strength of electronic interactions is reduced. For instance, no gate tunable interaction-induced band gap has been observed in FLG encapsulated in hBN[16]. On the other hand, suspended graphene devices can be extremely clean and provides an ideal platform for exploring electronic interactions close to the charge neutrality point, though they are structurally fragile[17] and can be susceptible to strain[17] or ripples[17,18]. In this thesis, I focus only on suspended devices, whose field effect mobility is enhanced over that of substrate-supported devices by factors of about 50-200, reaching upwards of 200,000 cm^2/Vs[6], as shown in figure 5.1. Such high mobilities can be extremely difficult to achieve with typical substrate-supported samples.
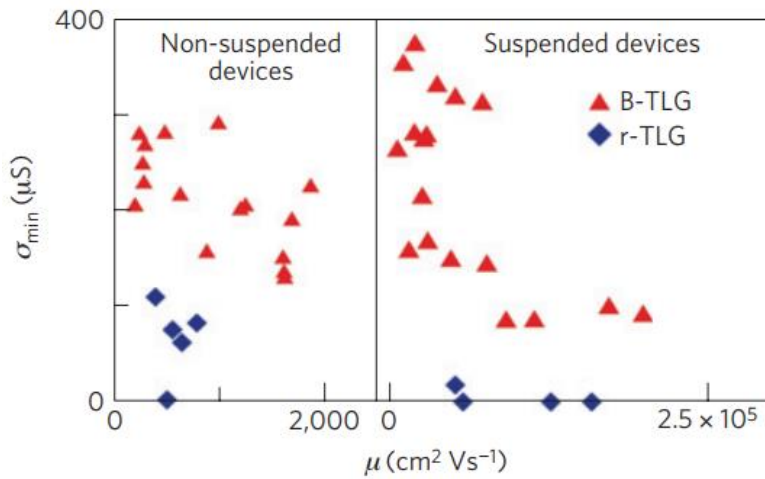
Figure 5.1. Minimum conductance σ_{min} v. electronic mobility µ for B-TLG and r-TLG devices: (a) non-suspended and (b) suspended devices. Image taken from ref. 6.

5.3 Independent tuning of the out-of-plane electric field and charge carrier density

A suspended graphene membrane separated from a metallic gate can be modeled as a parallel plate capacitor, with induced charge carrier density

$$n = \frac{Q}{eA} = \frac{C_A V_G}{e} \tag{5.1}$$

where Q is the total induced charge, A is the area in which the charge is distributed, C_A is the capacitance per area, V_G is the applied gate voltage, and e is the electron charge. When both back gate and top gate are present, equation 5.1 becomes:

$$n = n_{BG} + n_{TG} \equiv \frac{C_{BG}^A}{e}(V_{BG} - V_{BG}^D) + \frac{C_{TG}^A}{e}(V_{TG} - V_{TG}^D) \tag{5.2}$$

where n_{BG} (n_{TG}) is the charge carrier density induced by the back (top) gate, C_{BG}^A (C_{TG}^A) is the capacitance per area of the back (top) gate, V_{BG} (V_{TG}) is the applied back (top) gate voltage, and V_{BG}^D (V_{TG}^D) is the back (top) gate Dirac point. From Gauss' Law, the out-of-plane electric field $E_\perp$ in the sample is:

$$E_\perp = \frac{(n_{BG} - n_{TG})e}{2\varepsilon_0} \tag{5.3}$$

where ε_0 is the vacuum permittivity. Since all terms are known and there only exists two variables (V_{BG} and V_{TG}), the two equations can be independently solved, resulting in the de-coupling of $E_\perp$ and n in these dual-gated samples.

5.4 Electric field tuning and spontaneous insulating states in bilayer graphene

We first focus on dual-gated suspended BLG devices, which typically have source-drain separations $\sim 1 - 1.5$ μm, and widths $1.3 - 1.6$ μm. Current annealing at

T=1.6K is used to remove resist residue and absorbants through Joule heating, as discussed in chapter three. Samples are measured in a He^3 cryostat,

5.4.1 Single particle gap in bilayer graphene

From tight-binding calculations, the charge carriers in BLG behave as massive Dirac fermions, and are described by a combination of the Schrödinger and Dirac equations, with energy given by[19,20-24]

$$E_s(k) = \left[e^2 V_\perp{}^2 + \hbar^2 v_F{}^2 k^2 + t_\perp{}^2/2 \pm (4e^2 V^2 \hbar^2 v_F{}^2 k^2 + t^2 \hbar^2 v_F{}^2 k^2 + t_\perp{}^4/2)^{1/2}\right]^{1/2}$$

$$(5.4)$$

where $V_\perp$ is the electric potential across the bilayer, e the electron charge, h is Planck's constant, v_F~10^6 m/s is SLG's Fermi velocity, t~3 eV is the nearest neighbor hopping, $t_\perp$~0.4 eV is the interlayer hopping energy, and the $\pm$ signs refer to the conduction and valence bands, respectively. For $V_\perp$=0 and at low energies, BLG has a parabolic dispersion with zero band gap, $E=\pm h^2 k^2/2m^*$, where m*=$t_\perp/2v_F{}^2$ ~0.03m_e is the effective mass of charge carriers[25-27] and m_e is electron rest mass. For $V_\perp \neq 0$, the band structure adopts a 'Mexican-hat' shape, with a band gap $\Delta = t_\perp V_\perp/(t_\perp{}^2 + V_\perp{}^2)^{1/2}$.

We note that $V_\perp$ is the screened internal potential between the layers, and is not simply given by $E_\perp$d, where $E_\perp$ is the applied external field and d=0.34 nm is the interlayer spacing. Generally, $V_\perp$ is reduced from $E_\perp$d by a factor of 5-10 at low $E_\perp$ and by a factor of ~2 at large $E_\perp$. The most interesting consequence of equation 5.4 is that BLG allows creation of a band gap that is tunable by an applied external potential and

ranges from 0 to 250 meV. Such a tunable band gap has been verified in a number of transport and optical experiments[28-33], and is significant as a promising route to band gap engineering and control in graphene electronics.

5.4.2 Transport data of bilayer graphene devices with moderate mobility

We first examine the transport data[35] from a dual-gated suspended device with moderate mobility, ~10,000 cm^2/Vs. The presence of two gates allows us to adjust the applied electric field $E_\perp$ and induced charge density n independently. Figure 5.2 presents a two-dimensional plot of the two-terminal differential conductance $G=dI/dV$ (color) vs. applied back gate voltage V_{bg} and top gate voltage V_{tg}. The most prominent feature of the plot, the thin diagonal band, indicates the CNP of the device, demonstrating that charge density and type can be tuned by either of the two gates. The slope of the band in the V_{tg}-V_{bg} plane yields the ratio between the capacitive coupling efficiency of the two gates, $C_{tg}/C_{bg} \cong 0.34$, where C_{bg} (C_{tg}) is the capacitance per unit area between graphene and the back gate (top gate). From Landau fan data (not shown) as well as geometrical consideration, we estimate that $C_{bg} \sim 50$ aF/μm^2 and $C_{tg} \sim 16.6$ aF/μm^2.
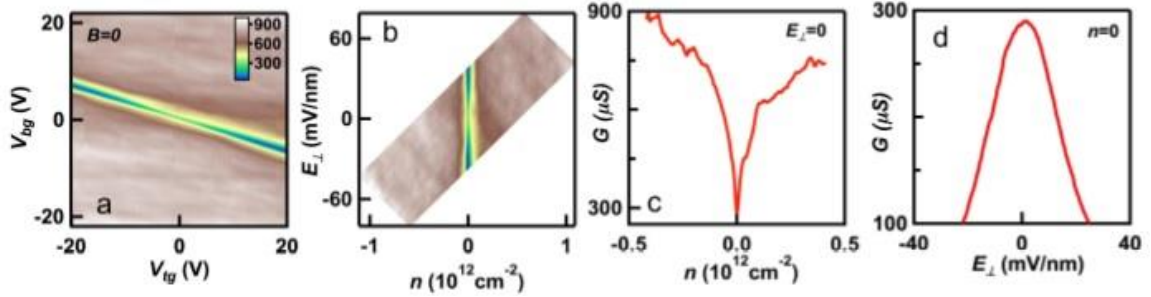
Figure 5.2. Electronic transport data in a suspended BLG device with a moderate mobility. (a). $G(V_{bg}, V_{tg})$ of a device with mobility 10,000 cm^2/Vs at B=0. (b). Same data as (a) plotted as $G(E_\perp, n)$. (c). Line trace $G(n)$ at $E_\perp$=0. (d). Line trace $G(E_\perp)$ at n=0. Image taken from ref. 35.

The device behavior is more easily analyzed as a function of $E_\perp$ and n, which are

calculated using equations 5.2 and 5.3. Figure 5.2b replots the data in figure 5.2a as a

function of $E_\perp$ (vertical axis) and n (horizontal axis). A line trace $G(n)$ at $E_\perp$=0 is shown

in figure 5.2c. As expected, G rises sharply as n increases, indicating reasonably high

device quality. Figure 5.2d displays the vertical line trace $G(E_\perp)$ at n=0, where G

decreases symmetrically with $E_\perp$ of either polarity. Such a conductance maximum at n=0

is consistent with the opening of a small band gap induced by electric field.

5.4.3 Transport data of bilayer graphene devices with high mobility

The $E_\perp$-induced gap in equation 5.4 (nascent in figure 5.2d) is often called the

single-particle gap, since it emerges from calculations that ignore electronic interactions.

Interestingly, it appears to break down for our very best samples with mobility >50,000

cm^2/Vs[4,34,36,37]. Figure 5.3a-b plots $G(V_{bg}, V_{tg})$ and $G(E_\perp, n)$ of a device[35] with mobility

~80,000 cm^2/Vs. Similar to figure 5.2c, the line trace $G(n)$ at $E_\perp$=0 shows an exceedingly

steep V curve, indicating very strong field effect (figure 5.3c). However, in contrast to

data in figure 5.2d, $G(E_\perp)$ at $n=0$ displays a conductance minimum at $E_\perp=0$, and increases

to a maximum at $|E_\perp|\sim15$ mV/nm, before decreasing again for larger $E_\perp$. Another

surprising feature is that the minimum conductivity at $E_\perp=n=0$ is exceedingly low, $\sim$1-5

μS, thus the device is insulating at the CNP. This again is in sharp contrast with the

device in figure 5.2, whose minimum conductance is $\sim$300 μS.
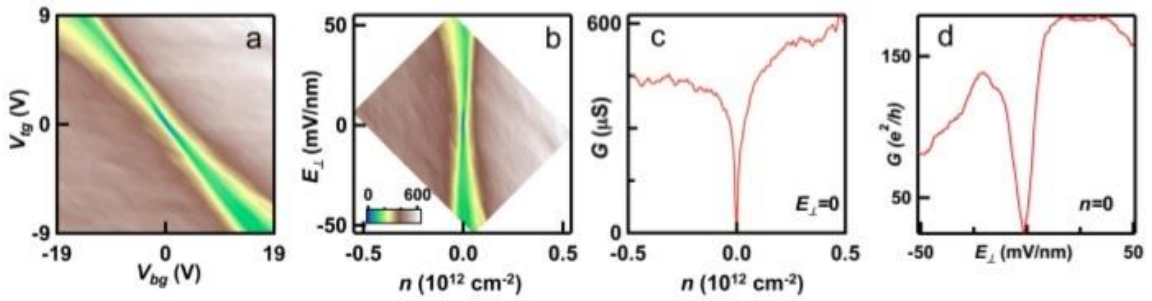
Figure 5.3. Electronic transport data in a suspended BLG device with high mobility:
(a). $G(V_{bg}, V_{tg})$ of a device with mobility 80,000 cm^2/Vs at $B=0$. (b). Same data as (a)
plotted as $G(E_\perp, n)$. (c). Line trace $G(n)$ at $E_\perp=0$. (d). Line trace $G(E_\perp)$ at $n=0$. Image
taken from ref. 35.

To further investigate the insulating state at the CNP, we measure its conductance

G as a function of source-drain bias V and n_{bg}. The data are shown in figure 5.4a. The

dark blue region near the origin represents a low conductance state, 'sandwiched'

between conductance peaks (bright red regions) from above and below. This is more

clearly seen in the line trace $G(V)$ at $n_{bg}=n=E_\perp=0$ (figure 5.4b), where G remains close to

0 for small V, but rises abruptly to conductance peaks at $V=\pm2$mV, and decreases to 350

μS for $|V|>3$mV. Such a $G(V)$ curve strongly resembles the density of states of a gapped

state, such as that of a superconductor or charge density wave, and points to the formation

of a gapped insulating phase in charge neutral BLG. Intriguingly, this insulating phase

can be 'extinguished' by the application of $E_\perp$. Figure 5.4c plots $G(V, n)$ at $E_\perp=14.4$

mV/nm. In contrast to data at $n_{bg}=n=E_\perp=0$ (figure 5.4b), both the central insulating

region and the sharp conductance peaks are absent. Instead, the $G(V)$ line trace (figure

5.4d) is moderately V-shaped, suggesting slightly non-linear I-V characteristics, which is

what one would normally expect for transport across a mesoscopic device. Thus, upon

application of a small electric field, the gapped insulating phase is suppressed, and BLG

reverts to the behavior of a more conventional conductor.
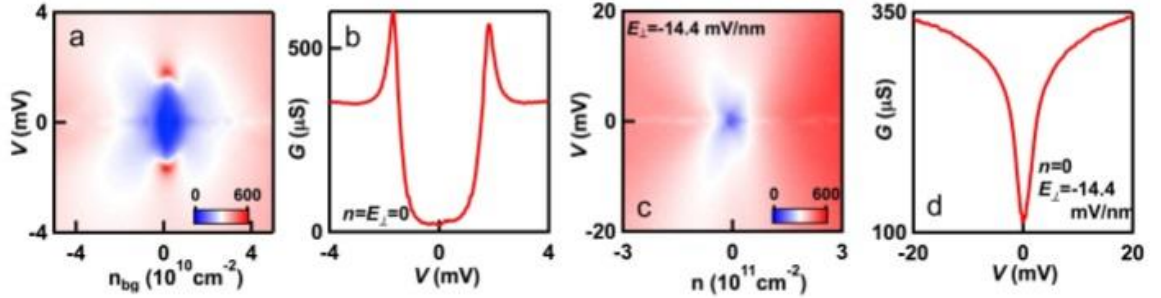
Figure 5.4. Gate-tuning the spontaneous insulating state in bilayer graphene: (a). $G(V, n_{bg})$ at $B=0$. (b). Line trace through (a) at $n_{bg}=n=E_\perp=0$. (c). $G(V, n)$ at $E_\perp=14.4$ mV/nm. Color scale is the same as that in (a). (d). Line trace through (c) at $n=0$. Image taken from ref. 35.

Finally, we examine how this insulating phase change with temperature T and

magnetic field B. Figure 5.5a displays minimum conductivity $\sigma_{min}(T)$ at $B=n=E_\perp=0$ for

two different samples. For both samples, the conductance drops precipitously at $T\sim5$K,

suggesting the onset of an insulating phase. In magnetic field, the conductance, which is

already low, decreases exponentially with B, and reaches nS or $(G\Omega)^{-1}$ for $B\sim0.3$T. This

gapped insulating phase we observe in charge neutral bilayer graphene cannot be

explained by singe particle physics, but arises from many body interactions. In fact, the

enhanced density of states of BLG at the CNP is unstable to electronic interactions and

favors formation of correlated states with various broken symmetries. There has been
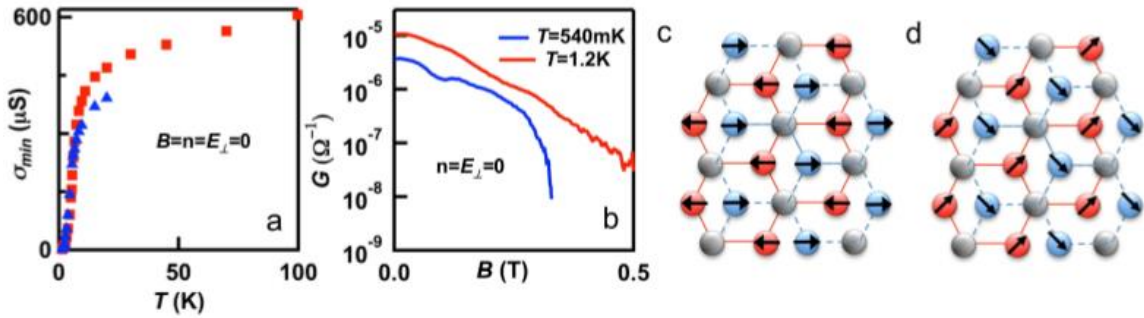
Figure 5.5. Transport measurements and electron configurations in BLG: (a). Minimum conductivity of two suspended BLG devices vs. T(K) at the charge neutrality point. (b). Conductance vs. B at T=0.54 and 1.2K, respectively. (c). Schematic configuration of electrons in BLG at B=0, showing a layer antiferromagnetic state. (d). Schematic configuration of electrons at finite B, showing a canted antiferromagnetic state. Image taken from ref. 35.

much experimental and theoretical debate on this topic[4,27,34,36-58]. Various theoretical models proposed a number of possible correlated states in BLG, which include: (1). nematic state with reduced rotational symmetry, (2). Quantum anomalous Hall and current loop states with broken time reversal symmetry, (3). layer antiferromagnetic state with broken time reversal and spin rotation symmetries, (4). charge layer polarized state with broken inversion symmetry, and (5). quantum spin Hall state with broken spin rotational and Ising valley symmetries. Our experimental data is most consistent with the layer antiferromagnetic state (LAF), where the two layers are oppositely spin polarized (figure 5.5c); upon application of magnetic field and the onset of Zeeman energies, the spins start to tilt, giving rise to a canted antiferromagnetic state, which has recently been confirmed by an experiment on BLG in a tilted magnetic field[59].

5.5   Probing of the intrinsic gap in rhombohedral-stacked trilayer graphene with temperature and external fields

Similar to the high-quality BLG devices measured, pristine rhombohedral-stacked

trilayer graphene (r-TLG) samples in this work show high electronic field effect

mobilities between 20,000 and 90,000 cm^2/Vs, with low minimum conductance at low

temperatures in the absence of external fields. The r-TLG samples in this work typically

have source-drain separations ~ 1 – 1.5 μm, and widths 1.3 – 1.6 μm. In this work, we

probe the spontaneous interaction-induced gap of two high mobility, suspended r-TLG

devices[60] as a function of temperature and external fields.

5.5.1   Temperature dependence of the intrinsic gap in rhombohedral-stacked trilayer graphene

To investigate the nature of the intrinsic gap in r-TLG, we take transport

spectroscopy[34,61] of two r-TLG devices at $n=U_\perp=0$ reveals intriguing features: at small

source-drain bias V, the device stays insulating, but as V increases ±42mV, G rises by

more than six orders of magnitude to extremely sharp peaks, then decreases to ~15 e^2/h

for larger V (figure 5.6a). Such a $G(V)$ curve strongly resembles the density of states of a

gapped phase, suggesting the presence of an energy gap Δ~42meV at $n=U_\perp=\mathbf{B}=0$. With

increasing charge density n, the gap diminishes and eventually disappears entirely (figure

5.6b). At $n=3\text{x}10^{11}\text{cm}^{-2}$, $G(V)$ is flat, indicating that r-TLG becomes gapless at high

density. The gapped, insulating state near the CNP in the absence of external fields is

unexpected from tight-binding calculations, but instead suggests a phase arising from

electronic interactions with spontaneous broken symmetries[62]. The magnitude of the gap, ~42meV, is exceedingly large for an interaction-induced state.
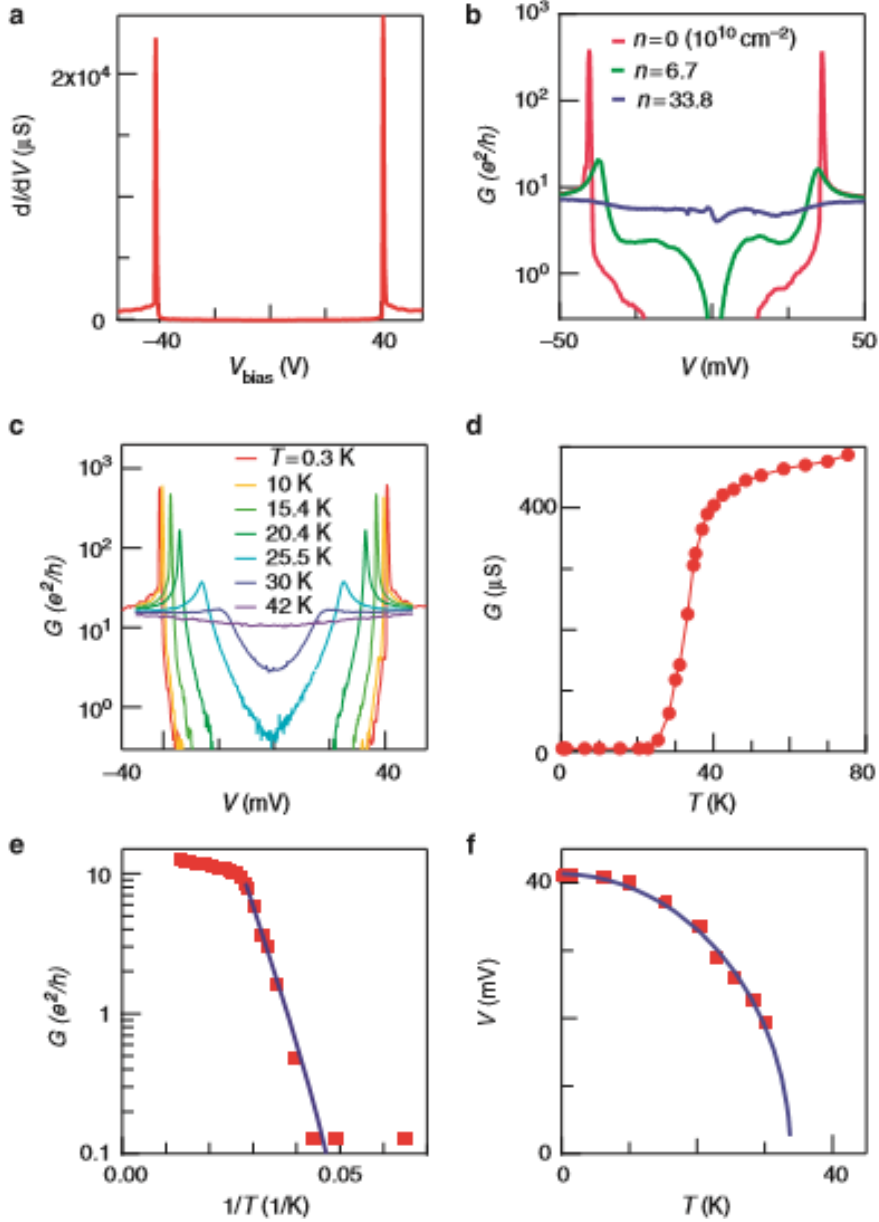
Figure 5.6. Transport data at $B_\perp=0$ (a,b: Device 1; c-f: Device 2): (a) $G(V)$ at $U_\perp=n=0$. (b) $G(V)$ at $U_\perp=0$ and different n. (c) $G_{min}(V)$ at $U_\perp=n=0$ and different temperatures. (d) G_{min} at $V=0$ versus T. (e) G_{min} versus $1/T$ in Arrhenius scale. The blue line is a fit to the equation $G_{MIN} = G_0 e^{-\Delta/2k_BT}$ for 30K<T<40K. (f) Measured Δ as a function of T. The solid line is a fit to equation 5.5. Image taken from ref. 60.

It is more than an order of magnitude larger than that found in BLG[34,36], reflecting the divergent nature of the density of states and strong electronic interactions in r-TLG at the CNP. It also a factor of seven larger than that previously observed in singly gated devices[6], likely due to improved device geometry and quality.

To further establish the magnitude of the gap, we examine temperature dependence of $G(V)$ at $n=U_\perp=0$ (figure 5.6c). Figure 5.6d plots minimum conductance $G_{min}=G(V=0)$ as a function of T. At high temperatures $T>40K$, the device is conductive, $G_{min}\sim15$ e^2/h with a small linear T-dependence. The $G(V)$ curves are approximately constant, similar to that of a conventional resistor. However, when $T<\sim40K$, G_{min} drops precipitously and becomes insulating for $T<30K$, and $G(V)$ curves develop prominent peaks at finite V. In the transition region $30<T<40K$, the $G_{min}(T)$ curve is well-described by the thermal activation equation, $G_{MIN} = G_0 e^{-\Delta/2k_B T}$ (figure 5.6e), where k_B is the Boltzmann's constant and $\Delta\sim43$meV is obtained as a fitting parameter. This is in excellent agreement with the value of Δ obtained from $G(V)$ curves at $T=300$mK, thus confirming the presence of an insulating state with $\sim42 \pm 1$ meV gap. Using $G(V)$ curves, we can also directly measure the evolution of Δ (taken as half of the peak-to-peak separation in V) as a function of T. As shown in figure 5.6f, Δ is almost constant for $T<10K$, but drops precipitously for $T>30K$. This behavior is a characteristic of order parameters during phase transitions in mean field theories. Thus, we fit $\Delta(T)$ to the function[63]

$$\Delta(T) = \Delta_0 \left[A\left(1-\frac{T}{T_C}\right) + B\left(1-\frac{T}{T_C}\right)^2\right]^{1/2} \tag{5.5}$$

where T_c is the critical temperature. Equation 5.5 reduces to the usual mean –field

functional form $\sqrt{1 - \frac{T}{T_c}}$ for T/T_c sufficiently close to 1, and the second term $\left(1 - \frac{T}{T_c}\right)^2$ is

inserted to capture the vanishingly small dependence on T as $T\rightarrow 0$. Excellent agreement

with data is obtained, yielding $A = 2.0$, $B = -1.0$, and $T_c = 34K$. The energy scale of

the gap, $\frac{\Delta_0}{k_B} = 500\ K$, which is much larger than that associated with the critical

temperature, signifies that this insulating state observed at the CNP is a correlated phase.

5.5.2 Tuning of the intrinsic gap in rhombohedral-stacked trilayer graphene with external fields

To elucidate the nature of this correlated phase, we examine how it is modified in

the presence of an external field that selectively breaks one of the degeneracies. For

instance, application of $U_\perp$ breaks the inversion (which-layer) symmetry, and, in the

single-particle picture, gives rise to a proportionally scaled energy gap. Figure 5.7a

displays G as a function of V and $U_\perp$ at n=0. As $U_\perp$ is the externally imposed potential

bias, it will be heavily screened due to r-TLG's large density of states near the CNP[64-66].

Thus, we expect the screened interlayer potential bias $U_\perp^S \ll U_\perp$. Using a simplified two-

band Hamiltonian for r-TLG and assuming that the dielectric constant of r-TLG is 1, we

self-consistently calculate $U_\perp^S$ for given values of n and $U_\perp$:

$$U_\perp^S = U_\perp + \frac{de^2}{2\varepsilon_0}\left(\frac{1}{\pi}\right)\left(\frac{\gamma_1}{\hbar v}\right)^2 \left(\frac{U_\perp^S}{2\gamma_1}\right)^{2/3} \left[\int_0^{x_F} \frac{dx}{\sqrt{1+x^3}} - 2.8\right] \qquad (5.7)$$

where $x_F = v^2 \pi \hbar^2 n \left[\frac{4}{(U_\perp^S)^2 \gamma_1^4} \right]^{1/3}$, γ_1 is the interlayer hopping parameter, v is the Fermi

velocity of charges in monolayer graphene, and d=0.67nm is the spacing between

outmost layers. The screening-corrected data $G(V, U_\perp^S)$ are shown in figure 5.7b. The

sharp peaks in $G(V)$, that is, the gap edges, appear as red curves that separate the

insulating (dark blue) and conductive (light blue) regions in figure 5.7a,b.
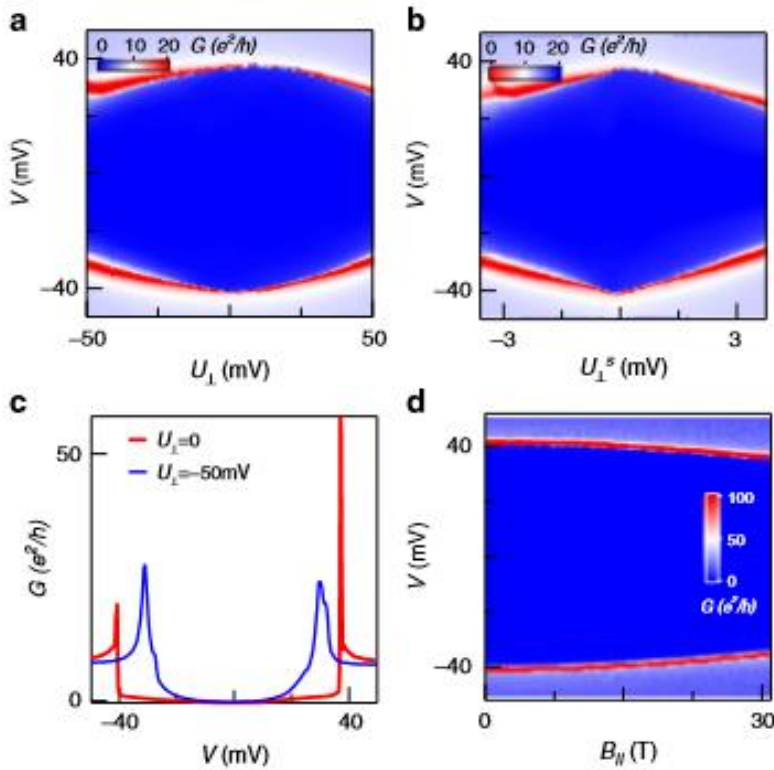
Figure 5.7. Transport data at n=0 and finite $U_\perp$ and $B_{/\!/}$: (a) $G(V, U_\perp)$ and $G(V, U_\perp^S)$ in
units of e^2/h from Device 1. (c) Line traces $G(V)$ at $U_\perp$=0 and $U_\perp$= -50mV. (d) $G(V, B_{/\!/})$
in units of e^2/h from Device 2. Image taken from ref. 60.

Δ decreases symmetrically and linearly with applied $U_\perp^S$ of either polarity, to $\sim$ 30meV at

$|U_\perp|$=50mV or $|U_\perp^S|$=3mV (figure 5.7b), though not yet completely closed at the largest

applied $|U_\perp|$ (in other devices with lower mobility, we also observe that the device

conductance increases from <0.1 e^2/h with increasing $|U_\perp|$, exceeding $1.5e^2/h$ at

$|U_\perp|$=85mV). In contrast, an in-plane magnetic field $B_{/\!/}$ couples to the spin but not orbital

degrees of freedom and raises the Zeeman energy. Figure 5.7d plots $G(V, B_{/\!/})$ for $B_{/\!/}$=0 to

31T. Δ stays almost constant for $B_{/\!/}$|<10T, but decreases to 35mV at $B_{/\!/}$=31T. Thus,

addition of Zeeman energy suppresses the gapped phase, suggesting that the phase has

spin-ordering, but no net magnetic moment.

5.5.3 Discussion of the intrinsically-gapped state

To summarize our experimental findings, we observe an insulating state in r-TLG

at n=$U_\perp$=$\mathbf{B}$=0, with an energy gap $\Delta(T$=0)~42meV. This gap can be suppressed by

increasing charge density n, a critical temperature T_c~34K, by an interlayer potential $U_\perp$

of either polarity and by an in-plane magnetic field. Among the spatially uniform

correlated phases in r-TLG discussed in the literature[67-72], only LAF, in which the top and

bottom layers have equal number of electrons with opposite spin polarization, is

consistent with our experimental observations. For instance, the presence of an energy

gap eliminates the mirror-breaking, inversion breaking, interlayer current density wave or

layer polarization density wave states[71], and the zero conductance eliminates the

superconductor, quantum spin Hall and quantum anomalous Hall states that host finite (or

even infinite) conductance. Furthermore, the symmetrical suppression of the gap by $U_\perp$ of

either polarity suggests that charges in the insulating state are layer-balanced, as the

device would otherwise exhibit opposite dependence on $U_\perp$ of opposite polarities. This

excludes all layer-polarized states, including the quantum valley Hall and layer polarization density wave states, and any single-particle state that arises from inadvertent doping of one of the surface layers.

Thus, based on the above experimental observations, we identify LAF with broken time reversal and spin rotation symmetries as the most likely candidate among the proposed ground states in r-TLG. Theoretically, an LAF ground state can be justified by the following considerations. The strong screening due to the large density of states in r-TLG leads to very short-range Coulomb repulsions among. For such local interactions, the most likely symmetry-broken states are the LAF and nematic phases, and the gapless and conductive nematic phase is incompatible with our observation of a gapped insulator, leaving LAF as the only viable alternative. Moreover, mean field arguments that generally favor the LAF phase should be more robust in r-TLG than that in bilayer graphene, due to the divergent density of states and stronger electrons near the CNP that suppresses fluctuations. Finally, recent works[73,74] report formation of magnetic moments in graphene that results from interactions among the p-electrons of graphene in the presence of hydrogen and fluorine atoms and vacancies, thus it is not unreasonable to expect emergent magnetism arising from strong electronic interactions in r-TLG.

Within the mean-field framework, a simple estimate of the LAF gap yields

$$\Delta \approx 2 \times \left(\frac{c}{\pi\sqrt{3}}\right)^3 \frac{\gamma_1^4 U^3}{\gamma_0^6} \tag{5.8}$$

where $\gamma_0 \approx 2.7\text{eV}$, $\gamma_0 \approx 0.4\text{eV}$ are tight binding parameters, c $\approx$2.8, and U is the Hubbard onsite interaction. Using these parameters, and substituting the experimentally obtained value Δ=42meV, we obtain U~13eV, not too different from theoretically

predicated values[75-77] of 5–10eV. Alternatively, the gap can be further enhanced by

exchange processes associated with the long-range part of the interaction[75]. A possible

phase diagram for charge neutral r-TLG that is consistent with our experimental results,

together with schematics for electron configurations, is summarized in figure 5.8. In the

absence of external fields, a charge neutral r-TLG is an LAF with broken time reversal

and spin rotation symmetries. Increasing $U_\perp$ of either polarity pushes electrons to one of

the surface layers and suppresses the gap. For sufficiently large $|U_\perp|$, all charges reside in

either the top or bottom layer, giving rise to a quantum valley Hall (QVH) insulator with

broken inversion symmetry. We note that the different broken symmetries of the QVH
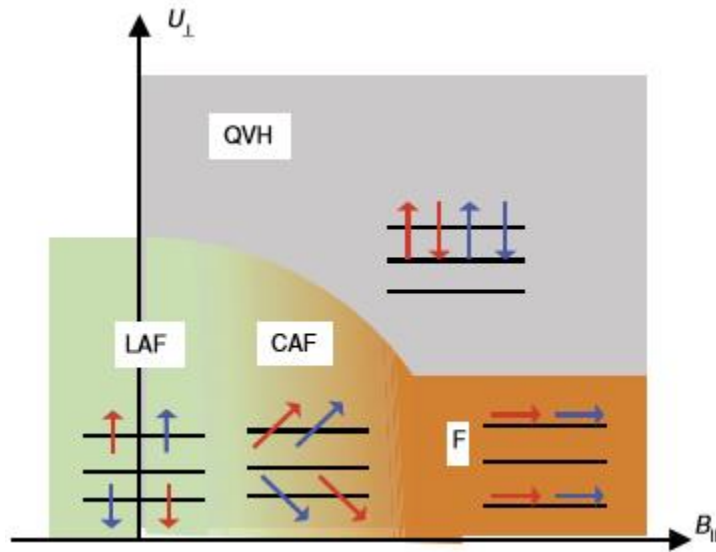
Figure 5.8. Possible phase diagram and schematics of electronic configurations for r-TLG: The blue and red arrows indicate charges from K and K' valleys, respectively (CAF, canted antiferromagnet; F, ferromagnet; LAF, layer antiferromagnet; QVH, quantum valley Hall). Image taken from ref. 60.

and LAF states preclude a continuous phase transition between them[49,78,79]. In contrast, as

$B_\parallel$ increases from 0, the competition between the Zeeman and the exchange energies tilts

the electron spins, and r-TLG crosses over to the CAF phase. For very large $B_{/\!/}$, we expect that the electrons eventually form a ferromagnet (F); in the quantum Hall regime, this ferromagnet is analogous to a quantum spin Hall state[59], with counter-propagating edge states and conductance B~$6e^2$/h.

5.6 Conclusion and references

We have provided evidence that the suspension of FLG membranes and the application of top gates are important to increase field mobility and decouple $E_\perp$ and n, respectively, allowing for the fine tuning of external fields in high mobility samples. We have shown that moderate mobility BLG devices are conducting at low temperature in the absence of external fields and obey the single particle picture with the tendency for $E_\perp$ to open a single particle gap. Conversely, high mobility BLG devices are insulating at low temperature with a 2-meV-gap that is closed by $E_\perp$, which violates the single particle picture and implies the presence of correlated electron behavior. Furthermore, we have shown results for the tuning of the ~40 meV intrinsic gap in high mobility r-TLG as a function of carrier density, temperature, electric and magnetic fields. Finally, transport data is consistent with a layer antiferromagnetic phase for both BLG and r-TLG at low temperature in the absence of external fields.

References

1. Bolotin, K. I., Sikes, K. J., Jiang, Z., Klima, M., Fudenberg, G., Hone, J., Kim, P., and Stormer, H. L. Ultrahigh electron mobility in suspended graphene. *Solid State Commun.* **146** (9-10), 351-355 (2008).

2. Bolotin, K. I, Sikes, K. J., Hone, J., Stormer, H. L., and Kim, P. Temperature-dependent transport in suspended graphene. *Phys. Rev. Let*. **101**, 096802 (2008).

3. Tombros, N., Veligura, A., Junesch, J., Van den Berg, J. J., Zomer, P. J., Wojtaszek, M., Vera Marun, I. J., Jonkman, H. T., and Van Wees, B. J. Large yield production of high mobility freely suspended grapehen electronic mobility devices on a PMGI based organic polymer. *J. Appl. Phys.*, **109**, 093702 (2011).

4. Weitz, R. T., Allen, M. T., Feldman, B. E., Martin, J., and Yacoby, A. Broken-symmetry states in doubly gated suspended bilayer graphene. *Science*, **330**, 812-816 (2010).

5. Bao, W., Velasco Jr., J., Zhang, F., Jing, L., Standley, B., Smirnov, D., Bockrath, M., MacDonald, A. H., and Lau, C. N. Evidence for a spontaneous gapped state in ultraclean bilayer graphene. *Proc. Natl. Acad. Sci.*, **109** (27), 10802-10805 (2012).

6. Bao, W., Jing, L, Velasco Jr., J., Lee, Y., Liu, G., Tran, D., Standley, B., Aykol, M., Cronin, S. B., Smirnov, D., Koshino, M., McCann, E., Bockrath, M., and Lau, C. N. Stacking-dependent band gap and quantum transport in trilayer graphene. *Nat. Phys*., **7**, 948-952 (2011).

7. Velasco Jr., J., Lee, Y., Zhang, F., Myhro, K., Tran, D., Deo, M., Smirnov, D., MacDonald, A. H., and Lau, C. N. Competing ordered states with filling factor two in bilayer graphene. *Nat. Commun*., **5**, 4550 (2014).

8. Lee, Y., Velasco Jr., J., Tran, D., Zhang, F., Bao, W., Jing, L., Myhro, K., Smirnov, D., and Lau, C. N. Broken symmetry quantum hall states in dual-gated ABA trilayer graphene. *Nano Lett*., **13**, 1627-1631 (2013).

9. Lee, Y., Tran, D., Myhro, K., Velasco Jr., J., Gillgren, N., Poumirol, J. M., Smirnov, D., Barlas, Y., and Lau, C. N. Multicomponent quantum hall ferromagnetism and Landau level crossing in rhombohedral trilayer graphene. *Nano Lett.*, **16**, 227-231 (2016).

10. Novoselov, K. S., Geim, A. K., Morozov, S. V., Jiang, D., Zhang, Y., Dubonos, S. V., Grigorieva, I. V., and Firsov, A. A. Electric field effect in atomically thin carbon films. *Science*, **306** (5696), 666-669 (2004).

11. Pallecchi, E., Lafont, F., Cavaliere, V., Schopfer, F., Mailly, D., Poirier, W., and Ouerghi, A. High electron mobility in epitaxial graphene on 4H-SiC(0001) via post-growth annealing under hydrogen. *Sci. Rep*., **4**, 4558 (2014).

12. Dean, C. R., Young, A. F., Meric, I., Lee, C., Wang, L., Sorgenfrei, S., Watanabe, K., Taniguchi, T., Kim, P., Shepard, K. L., and Hone, J. Boron nitride substrates for high quality graphene electronics. *Nat. Nanotechnol.*, **5**, 722-726 (2010).

13. Gannett, W., Regan, W., Watanabe, K., Taniguchi, T., Crommie, M., and Zettl, A. Boron nitride substrates for high mobility chemical vapor deposited graphene. *Appl. Phys. Lett.*, **98** (24), 242105 (2011).

14. Wang, L., Meric, I., Huang, P. Y., Gao, Q., Tran, H., Taniguchi, T., Watanabe, K., Campos, L. M., Muller, D. A., Guo, J., Kim, P., Hone, J., Shepard, K. L., and Dean, C. R. One-dimensional electrical contact to a two-dimensional material. *Science*. **342** (6158), 614-617 (2013).

15. Stepanov, P., Barlas, Y., Espiritu, T., Che, S., Watanabe, K., Taniguchi, T., Smirnov, D., and Lau, C. N. Tunable symmetries of integer and fractional quantum hall phases in heterostructures with multiple Dirac bands. *Phys. Rev. Lett.*, **117**, 076807 (2016).

16. Li, L. H., Santos, E. J. G., Xing, T., Cappelluti, E., Roldan, R., Chen, Y., Watanabe, K., and Taniguchi, T. Dielectric screening in atomically thin boron nitride nanosheets. *Nano Lett.*, **15**, 218-223 (2015).

17. Bao, W., Myhro, K., Zhao, Z., Chen, Z., Jang, W., Jing, L., Miao, F., Zhang, H., Dames, C., and Lau, C. N. In situ observation of electrostatic and thermal manipulation of suspended graphene membranes. *Nano Lett.*, **12**, 5470-5474 (2012).

18. Bao, W., Miao, F., Chen, Z., Zhang, H., Jang, W. Y., Dames, C., and Lau, C. N. Controlled ripple texturing of suspended graphene and ultrathin graphite membranes. *Nat. Nanotechnol.*, **4**, 562-566 (2009).

19. Castro Neto, A. H., Guinea, F., Peres, N. M. R., Novoselov, K. S., and Geim, A. K. The electronic properties of graphene. *Rev. Mod. Phys.*, **81**, 109–162 (2009).

20. McCann, E. and Fal'ko, V. I. Landau-level degeneracy and quantum hall effect in a graphite bilayer. *Phys. Rev. Lett.*, **96**, 086805 (2006).

21. Guinea, F., Castro Neto, A. H., and Peres, N. M. R. Electronic states and Landau levels in graphene stacks. *Phys. Rev. B*, **73**, 245426 (2006).

22. Barlas, Y., Cote, R., Nomura, K. and MacDonald, A. H. Intra-Landau-level cyclotron resonance in bilayer graphene. *Phys. Rev. Lett.*, **101**, 097601 (2008).

23. Min, H., K., Borghi, G., Polini, M., and MacDonald, A. H. Pseudospin magnetism in graphene. *Phys. Rev. B,* **77**, 041407 (2008).

24. Min, H. K., Sahu, B., Banerjee, S. K., and MacDonald, A. H. Ab initio theory of gate induced gaps in graphene bilayers. *Phys. Rev. B,* **75**, 155115 (2007).

25. Cho, S. and Fuhrer, M. S. Massless and massive particle-in-a-box states in single- and bi-layer graphene. *Nano Res*. **4**, 385 (2011).

26. Henriksen, E. A., Jiang, Z., Tung, L. C., Schwartz, M. E., Takita, M., Wang, Y. J., Kim, P., and Stormer, H. L. Cyclotron resonance in bilayer graphene. *Phys. Rev. Lett*., **100**, 087403 (2008).

27. Martin, J., Feldman, B. E., Weitz, R. T., Allen, M. T., and Yacoby, A. Local Compressibility Measurements of Correlated States in Suspended Bilayer Graphene. *Phys. Rev. Lett*., **105**, 256806 (2010).

28. Zou, K. and Zhu, J. Transport in gapped bilayer graphene: The role of potential fluctuations. *Phys. Rev. B*, **82**, 081407 (2010).

29. Oostinga, J. B., Heersche, H. B., Liu, X. L., Morpurgo, A. F., and Vandersypen, L. M. K. Gate-induced insulating state in bilayer graphene devices. *Nat. Mater.* **7**, 151–157 (2008).

30. Yan, J. and Fuhrer, M. S. Charge transport in dual-gated bilayer graphene with Corbino geometry. *Nano Lett*., **10**, 4521 (2010).

31. Jing, L., Velasco Jr, J., Kratz, P., Liu, G., Bao, W., Bockrath, M., and Lau, C. N. Quantum transport and field-induced insulating states in bilayer graphene pnp junctions. *Nano Lett*., **10**, 4000–4004 (2010).

32. Xia, F. N., Farmer, D. B., Lin, Y. M., and Avouris, P. Graphene field-effect transistors with high on/off current ratio and large transport band gap at room temperature. *Nano Lett*., **10**, 715–718 (2010).

33. Taychatanapat, T. and Jarillo-Herrero, P. Electronic transport in dual-gated Bilayer graphene at large displacement fields. *Phys. Rev. Lett*., **105**, 166601 (2010).

34. Velasco Jr, J., Jing, L., Bao, W., Lee, Y., Kratz, P., Aji, V., Bockrath, M., Lau, C. N., Varma, C., et al., Transport spectroscopy of symmetry-broken insulating states in bilayer graphene. *Nat. Nanotechnol*., **7**, 156–160, (2012).

35. Lee, Y., Myhro, K., Tran, D., Gillgren, N., Velasco, J. Jr., Bao, W., Deo, M., and Lau, C. N. Band gap and correlated phenomena in bilayer and trilayer graphene. Proc. of SPIE, 8725, 872506 (2013).

36. Freitag, F., Trbovic, J., Weiss, M., and Schonenberger, C. Spontaneously gapped ground state in suspended bilayer graphene. *Phys. Rev. Lett*., **108**, 076602 (2012).

37. Veligura, A., van Elferen, H. J., Tombros, N., Maan, J. C., Zeitler, U., and van Wees, B. J. Transport gap in suspended bilayer graphene at zero magnetic field. *Phys. Rev. B*, **85**, 155412 (2012).

38. Nandkishore, R. and Levitov, L. Quantum anomalous Hall state in bilayer graphene. *Phys. Rev. B*, **82**, 115124 (2010).

39. Zhang, F. and MacDonald, A. H. Distinguishing spontaneous quantum Hall states in graphene bilayers. *Phys. Rev. Lett.*, **108**, 186804 (2012).

40. Zhang, F., Min, H., and MacDonald, A. H. Competing ordered states in bilayer graphene. *Phys. Rev. B*, **86**, 155128 (2012).

41. Kharitonov, M. Canted antiferromagnetic phase of the ν=0 quantum Hall state in bilayer graphene. *Phys. Rev. Lett.*, **109**, 046803 (2012).

42. Kharitonov, M. Edge excitations of the canted antiferromagnetic phase of the nu=0 quantum Hall state in graphene: A simplified analysis. *Phys. Rev. B*, **86**, 075450 (2012).

43. Mayorov, A. S., Elias, D. C., Mucha-Kruczynski, M., Gorbachev, R. V., Tudorovskiy, T., Zhukov, A., Morozov, S. V., Katsnelson, M. I., Fal'ko,V. I., et al. Interaction-driven spectrum reconstruction in bilayer graphene. Science, **333**, 860 (2011).

44. Lemonik, Y., Aleiner, I., and Fal'ko, V. I. Competing nematic, antiferromagnetic, and spin-flux orders in the ground state of bilayer graphene. *Phys. Rev. B*, **85**, 245451 (2012).

45. Lemonik, Y., Aleiner, I. L., Toke, C., and Fal'ko, V. I. Spontaneous symmetry breaking and Lifshitz transition in bilayer graphene. *Phys. Rev. B*, **82**, 201408 (2010).

46. Li, J. A., Martin, I., Buttiker, M., and Morpurgo, A. F. Topological origin of subgap conductance in insulating bilayer graphene. *Nat. Phys.*, **7**, 38–42 (2011).

47. Vafek, O. and Yang, K. Many-body instability of Coulomb interacting bilayer graphene: Renormalization group approach. *Phys. Rev. B*, **81**, 041401 (2010).

48. Throckmorton, R. E. and Vafek, O. Fermions on bilayer graphene: Symmetry breaking for B=0 and nu=0. *Phys. Rev. B*, **86**, 115447 (2012).

49. Jung, J., Zhang, F., and MacDonald, A. H. Lattice theory of pseudospin ferromagnetism in bilayer graphene: Competing interaction-induced quantum Hall states. *Phys. Rev. B*, **83**, 115408 (2011).

50. Scherer, M. M., Uebelacker, S., and Honerkamp, C. Instabilities of interacting electrons on the honeycomb bilayer. *Phys. Rev. B*, **85**, 235408 (2012).

51. Zhu, L., Aji, V., and Varma, C. M. Ordered loop current states in bilayer graphene. *Phys. Rev. B*, **87**, 035427 (2012).

52. Gorbar, E. V., Gusynin, V. P., Miransky, V. A., and Shovkovy, I. A. Broken symmetry nu=0 quantum Hall states in bilayer graphene: Landau level mixing and dynamical screening. *Phys. Rev. B*, **85**, 235460 (2012).

53. Gorbar, E. V., Gusynin, V. P., Jia, J., and Miransky, V. A. Broken-symmetry states and phase diagram of the lowest Landau level in bilayer graphene. *Phys. Rev. B*, **84**, 235449 (2011).

54. Gorbar, E. V., Gusynin, V. P., Miransky, V. A., and Shovkovy, I. A. Coexistence and competition of nematic and gapped states in bilayer graphene. *Phys. Rev. B*, **86**, 125439 (2012).

55. Cote, R., Luo, W. C., Petrov, B., Barlas, Y., and MacDonald, A. H. Orbital and interlayer skyrmion crystals in bilayer graphene. *Phys. Rev. B*, **82**, 245307 (2010).

56. Cote, R., Lambert, J., Barlas, Y., and MacDonald, A. H. Orbital order in bilayer graphene at filling factor v =1. *Phys. Rev. B*, **82**, 035445 (2010).

57. Shizuya, K. Structure and the Lamb-shift-like quantum splitting of the pseudo-zero-mode Landau levels in bilayer graphene. *Phys. Rev. B*, **86**, 045431 (2012).

58. Kim, S., Lee, K., and Tutuc, E. Spin-polarized to valley-polarized transition in graphene bilayers at v=0 in high magnetic fields. *Phys. Rev. Lett*., **107**, 016803 (2011).

59. Maher, P., Dean, C. R., Young, A. F., Taniguchi, T., Watanabe, K., Shepard, K. L., Hone, J., and Kim, P. Evidence for a spin phase transition at charge neutrality in bilayer graphene. *Nat. Phys.*, **9**, 154–158 (2013).

60. Lee, Y., Tran, D., Myhro, K., Velasco, J. Jr., Gillgren, N., Lau, C. N., Barlas, Y., Poumirol, J. M., Smirnov, D., and Guinea, F. Competition between spontaneous symmetry breaking and single-particle gaps in trilayer graphene. *Nat. Commun*., **5**, 5656 (2014).

61. Velasco, Jr J., et al. Transport measurement of Landau level gaps in bilayer graphene with layer polarization control. *Nano Lett*. **14**, 1324–1328 (2014).

62. Jia, J., Gorbar, E. V., and Gusynin, V. P. Gap generation in ABC-stacked multilayer graphene: Screening versus band flattening. *Phys. Rev. B*, **88**, 205428 (2013).

63. Ferrell, R. A. Temperature dependence of the superconductivity energy gap. *Zeitschrift fur Physik*, **182**, 1 (1964).

64. van Gelderen, R., Olsen, R., and Smith, C. M. Screening in multilayer graphene. *Phys. Rev. B*, **88**, 115414 (2013).

65. Koshino, M. Interlayer screening effect in graphene multilayers with ABA and ABC stacking. *Phys. Rev. B*, **81**, 125304 (2010).

66. Min, H., Hwang, E. H., and Das Sarma, S. Polarizability and screening in chiral multilayer graphene. *Phys. Rev. B*, **86**, 081402 (2012).

67. Castro, E. V., Pilar Lopez-Sancho, M., and Vozmediano, M. A. H. Vacancy induced zero energy modes in graphene stacks: The case of ABC trilayer. *Solid State Commun.*, **152**, 1483–1488 (2012).

68. Olsen, R., van Gelderen, R., and Smith, C. M. Ferromagnetism in ABC-stacked trilayer graphene. *Phys. Rev. B*, **87**, 115414 (2013).

69. Liu, H., Jiang, H., Xie, X. C., and Sun, Q.-f. Spontaneous spin-triplet exciton condensation in ABC-stacked trilayer graphene. *Phys. Rev. B*, **86**, 085441 (2012).

70. Jung, J. and MacDonald, A. H. Gapped broken symmetry states in ABC trilayer graphene. *Phys. Rev. B*, **88**, 075408 (2013).

71. Cvetkovic, V. and Vafek, O. Topology and symmetry breaking in ABC trilayer graphene. Preprint at http://arXiv.org/abs/1210.4923 (2012).

72. Scherer, M. M., Uebelacker, S., Scherer, D. D., and Honerkamp, C. Interacting electrons on trilayer honeycomb lattices. *Phys. Rev. B*, **86**, 155415 (2012).

73. Nair, R. R. et al. Spin-half paramagnetism in graphene induced by point defects. *Nat. Phys.*, **8**, 199–202 (2012).

74. Nair, R. R. et al. Dual origin of defect magnetism in graphene and its reversible switching by molecular doping. *Nat. Commun.*, **4**, 2010 (2013).

75. Wehling, T. O. et al. Strength of effective coulomb interactions in graphene and graphite. *Phys. Rev. Lett.*, **106**, 236805 (2011).

76. Verges, J. A., SanFabian, E., Chiappe, G., and Louis, E. Fit of Pariser-Parr-Pople and Hubbard model Hamiltonians to charge and spin states of polycyclic aromatic hydrocarbons. *Phys. Rev. B*, **81**, 085120 (2010).

77. Schuler, M., Rosner, M., Wehling, T. O., Lichtenstein, A. I., and Katsnelson, M. I. Optimal Hubbard models for materials with nonlocal Coulomb interactions: graphene, silicene, and benzene. *Phys. Rev. Lett*., **111**, 036601 (2013).

78. Zhang, F., Sahu, B., Min, H. K., and MacDonald, A. H. Band structure of ABC-stacked graphene trilayers. *Phys. Rev. B*, **82**, 035409 (2010).

79. Zhang, F., Tilahun, D., and MacDonald, A. H. Hund's rules for the N=0 Landau levels of trilayer graphene. *Phys. Rev. B*, **85**, 165139 (2012).

Chapter 6: Spontaneous insulating states in suspended rhombohedral-stacked tetralayer graphene

6.1   Introduction

The intrinsic insulating states observed in suspended bilayer (BLG) and rhombohedral-stacked trilayer graphene (r-TLG) devices, as discussed in last chapeter, arise from the large density of states near the charge neutrality point (CNP). Notably, the gap in r-TLG, which has a cubic dispersion, is an order of magnitude larger than that of BLG which has quadratic dispersion. This prompts us to examine rhombohedral-stacked tetralayer graphene (r-4LG) devices, which are predicted to have k^4 dispersion in the low-energy limit[1], and enormous density of states near the CNP. Though a small intrinsic gap is observed in Bernal-stacked tetralayer graphene (4LG) devices[2], r-4LG has not been explored. Using bias spectroscopy that is used to measure the intrinsic gaps in suspended BLG[3-5] and r-TLG[6-8] graphene, we report the experimental observation of a giant spontaneous insulating state in r-4LG at low temperatures in the absence of external fields. These suspended r-4LG samples have varying gap sizes ranging from 45 to 80 meV, which are mapped as a function of T, n, $E_\perp$, and $B_\perp$. Furthermore, we summarize findings on BLG, r-TLG and 4-TLG and discuss the nature of the intrinsic insulating state in rhombohedral-stacked few-layer graphene (FLG).

6.2 Temperature dependence of the intrinsic gap

In this section, we will discuss the results of probing the intrinsic band gap in FLG with respect to temperature, as shown in figure 6.1. Most r-4LG devices used in this study have dimensions $L = W = 1.5$ mm. Figure 6.1a plots the two-terminal differential conductance as a function of source-drain bias of an r-4LG device at the CNP and $B=E_\perp=0$ for T = 0.260 (red), 20 (orange), 30 (green), 35 (blue) and 70 K (purple), respectively. At low temperature, the gap size Δ, which is taken as the half of the peak-to-peak spacing, is measured to be 75 meV. This gap size is indeed very large, considering its nature as a correlated state. As temperature increases, Δ decreases in size, and is completely washed out at 70 K. The gap size Δ and the critical temperature T_c are plotted for BLG, r-TLG and r-4LG as a function of number of layers in the inset of figure 6.1b. We have observed a systematic trend in a few dozens of samples of increasing gap and critical temperature with increasing number of layers of rhombohedral-stacked FLG.
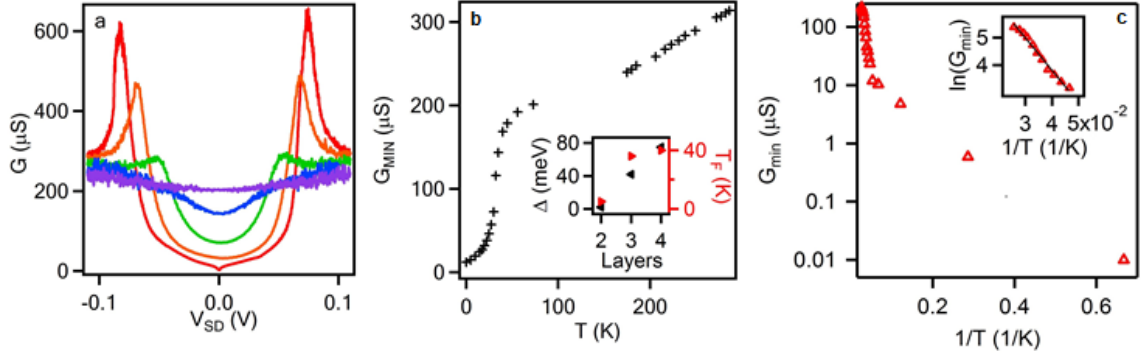
Figure 6.1: Probing the intrinsic gap in r-4LG at different temperature at
$n=E_{\perp}=B=0$. (a) $G(V_{SD})$ at varying temperatures. The red, orange, green, blue and purple line traces correspond to $T = 0.260, 20, 30, 35,$ and 70 K, respectively. (b) $G_{MIN}(T)$ for another r-4LG device. Inset: Gap size Δ and critical temperature T_c as a function of layer for 2, 3 and 4 layers. (d) $G_{MIN}(1/T)$ in Arrhenius scale for another r-4LG device. Inset: $ln(G_{MIN})$ plotted versus $1/T$ which shows nearly linear behavior.

The minimum conductance versus temperature $G_{MIN}(T)$ is plotted in figure 6.1b

for another r-4LG device. At high temperature, G_{MIN} is linear in T, suggesting

conductivity limited by electron-phonon scattering[9-14]. At ~40K, the conductance

decreases dramatically to zero, suggesting a metal-insulating transition. Similar data from

another r-4LG is plotted in Arrhenius scale as $G_{MIN}(1/T)$ in figure 6.1c. Around 20 K the

slope of $G_{MIN}(1/T)$ abruptly changes, indicating two different energy scales involved in

transport. Thus, r-4LG continues a trend found in its fewer-layer rhombohedral-stacked

FLG allotropes counterparts: increasing gap size and critical temperature with increasing

number of layers of graphene. This correlated phase of electron interactions will be

qualitatively discussed in section 6.5.

6.3 Dual-gated electrical tuning of the intrinsic gap

In this section, we explore the dependence of the intrinsic band gap in FLG on out-of-plane electric field $E_\perp$ and charge carrier density n. We observed similar behavior in several high-quality, doubly-suspended r-4LG FET devices. In figure 6.2a, we plot $G(V_{SD}, E_\perp)$ for an r-4LG device with a 48 meV gap. As $|E_\perp|$ increases from 0, the gap closes, as shown by line traces $G(V_{SD})$ at different $E_\perp$ at $n = B = 0$ and $T = 1.5$ K in figure 6.2b. The red, green, blue and purple line traces correspond to $E_\perp = 0$, 75, 155 and 190 mV/nm, respectively. We plot the gap size Δ verses electric field $E_\perp$ in the inset of figure 6.2b and find that at a critical field of 155 mV/nm the gap is completely closed, but increasing the electric field further causes the gap to re-open. This is similar to that observed in BLG, i.e. small $E_\perp$ closes the interaction-induced energy gap, and the device transitions to a layer-polarized state with a trivial band gap at very large $E_\perp$ (in this device, we limited the maximum out-of-plane electric field $E_\perp^{MAX} = 190$ mV/nm in order to prevent strain-induced buckling of the r-4LG membrane under electrostatic force, as the suspended FLG samples are mechanically fragile).
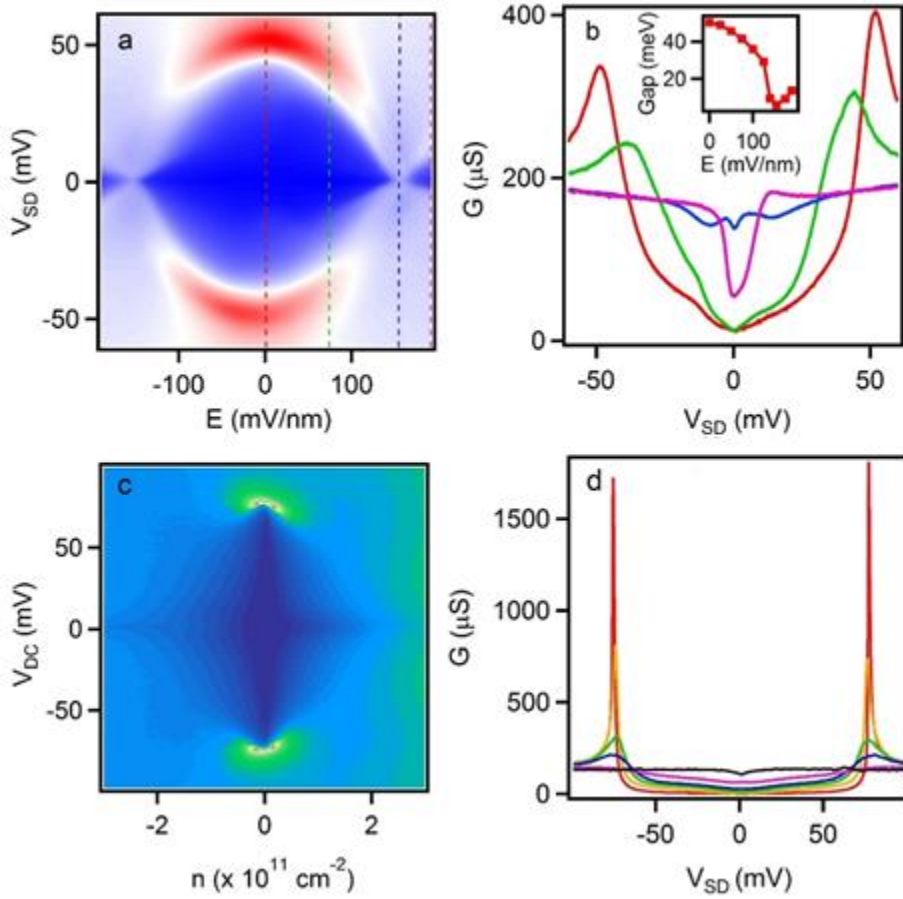
Figure 6.2: Tuning the intrinsic gap in r-4LG at $B = 0$. $G(V_{SD}, E_\perp)$ in μS for a suspended r-4LG device with 10,000 cm^2/Vs mobility and a 48 meV gap at $n = 0$ and $T = 1.5$ K. (b) Line traces $G(V_{SD})$ from (a) at varying out-of-plane electric field $E_\perp$. Red, green, blue and purple line traces correspond to $E_\perp = 0$, 75, 155 and 190 meV/nm. Inset: Gap size plotted vs. out-of-plane electric field, $\Delta(E_\perp)$. (c) $G(V_{SD}, n)$ in μS for another r-4LG device with a 79 meV gap at $E_\perp = 0$ and $T = 260$ mK. (d) Line traces $G(V_{SD})$ from (c) at varying charge carrier density n. The red, orange, green, blue, purple and black line traces correspond to $n = 0$, -0.2, -0.4, -0.6, -1.2, and -3.0 x 10^{11} cm^{-2}, respectively. Inset: Conductance at the CNP plotted vs. carrier density, $G_{CNP}(n)$.

Similar measurements are taken on another r-4LG device with a 79 meV gap.

$G(V_{SD}, n)$ is plotted in figure 6.2c at $E_\perp = B = 0$, and $T = 260$ mK. A robust insulating

state is observed as the blue low-conducting region near the CNP on the plot. Line traces

$G(V_{SD})$ are plotted in figure 6.2d where the red, orange, green, blue, purple and black line

traces are taken at $n = 0$, -0.2, -0.4, -0.6, -1.2, and -3.0 x 10^{11} cm^{-2}, respectively. The

gapped state completely closes at -3.0 x 10^{11} cm^{-2}, as high charge density increases

screening and decreases interaction effects.

6.4   Dependence of the intrinsic gap on magnetic field

In this section, we investigate the evolution of the gapped state of r-4LG in a

perpendicular magnetic field B. Figure 6.3a-b plots $G(V_{SD}, B)$ and line traces $G(V_{SD})$ at

different B, respectively. We can see that B increases the energy gap, while also

modifying the line shape of $G(V_{SD})$.
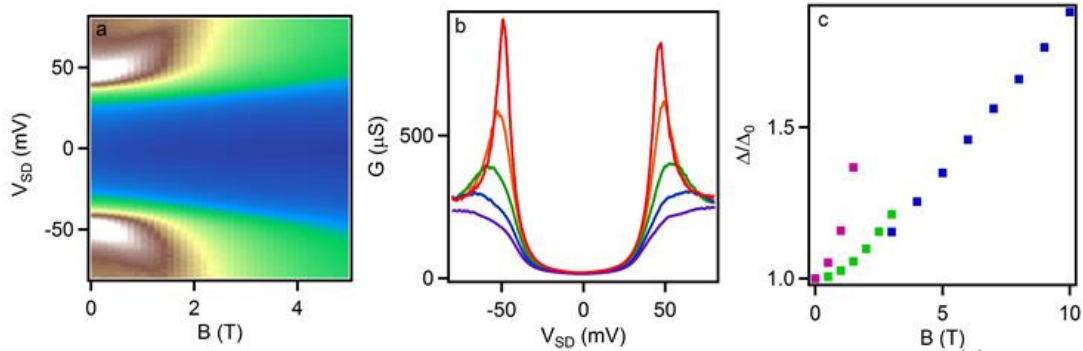
Figure 6.3. Tuning the intrinsic gap in r-4LG with perpendicular magnetic field at $n=E_{\perp}=0$ **and low temperature:** (a) $G(V_{SD}, B)$ in μS for a doubly-suspended r-4LG device. (b) Line traces $G(V_{SD})$ from (a) at varying magnetic field B. Red, orange, green, blue and purple line traces correspond to $B = 0$, 0.5, 1.0, 1.5 and 2.0 T, respectively. (c) Normalized gap size with respect to base temperature gap, $\Delta(B)/\Delta_0$. Results are shown for three different devices in purple, green and blue.

Measured base-temperature gaps Δ are normalized with respect to their $B = 0$ gap size

and plotted v. magnetic field as $\Delta(B)/\Delta_0$ in figure 6.3c. In this plot, we observe nearly-

linear dependencies of the gap size with magnetic field. The reason for the differing

94

slopes between the purple data points and the green and blue data points is unknown and could be related to the pre-existing strain or disorder in the system.

6.5 The nature of the intrinsic gap

To further investigate the nature of the intrinsic gap in r-4LG, we measure the gap size with varying different for several samples. Figure 6.4 plots $\Delta(T)$ normalized by the $\Delta_0(T=0)$ for three different suspended r-TLG devices. All three data sets collapse into a single curve, underscoring the reproducibility of these results. Similar to the analysis in the previous chapter on r-TLG, we can model this behavior of a closing gap with temperature by using T_c as an order parameter in temperature in the mean field approximation and by expressing $\Delta(T)$ as:

$$\frac{\Delta(T)}{\Delta_0(T=0)} = \left[A\left(1 - \frac{T}{T_c}\right) + B\left(1 - \frac{T}{T_c}\right)^2\right]^{1/2} \tag{6.1}$$

The data points are thus fitted to equation 6.1 (black curve in figure 6.1b), yielding fitting parameters $A = 1.57$, $B = -0.52$, and $T_c = 40$ K. Both the gap size Δ and the critical temperature T_c for r-4LG are larger than r-TLG, indicating an even more-enhanced correlated electron phase at the CNP in r-4LG.
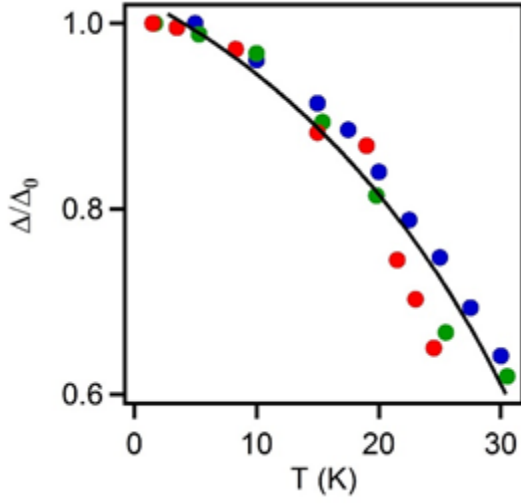
Figure 6.4. Intrinsic gap closure with temperature in r-4LG: Normalized gap size with respect to base temperature gap as a function of temperature, $\Delta(T)/\Delta_0$. Results are plotted in blue, green and red for three different devices.

Spontaneous symmetry breaking and the breakdown of single particle physics has been observed to occur in FLG systems[15-19] close to the CNP where electronic interactions become increasingly relevant. The interaction parameter, r_S, also known as the Wigner-Seitz radius, is given by the ratio of the average electron Coulomb interaction energy to the average Fermi energy, and this parameter has the form:

$$r_S \propto n^{\frac{-(p-1)}{2}} \tag{6.2}$$

where n is the charge carrier density and p is the energy dispersion power of the energy eigenstates of the Hamiltonian. In the case of linearly dispersing energy bands[3], $p=1$ and the interaction strength for SLG, r_S^{SLG}, is constant and independent of carrier density n. In BLG, however, which has two sets of quadratic energy bands with $p=2$ and a constant density of states[4], approaching the CNP leads to an increasing interaction strength r_S which has the form $r_S^{BLG} \propto n^{-1/2}$ and diverges at the CNP as $n\rightarrow0$. In r-TLG that has a

cubic dispersion with $p=3$ and diverging density of states $DOS \propto n^{-1/2}$ at low energies[6], the interaction strength diverges even quicker near the CNP with $r_S^{TLG} \propto n^{-1}$. Finally, tight-binding Hamiltonian calculations show that r-4LG has a quartic energy dispersion[1], and this causes the DOS to diverge faster as $DOS \propto n^{-1}$ at the CNP, and the interaction strength will also diverge even faster with $r_S^{4LG} \propto n^{-3/2}$ near the CNP. This trend of rapidly diverging DOS and electronic interaction strength r_S with number of layers near the charge neutrality is consistent with our experimental observation that the interaction-induced gap and transition temperature both increase with number of layers, as summarized in table 6.1. It is unclear when this layer-dependent trend will saturate in multiple layers of graphene as graphite is formed, and more work is needed to further probe the electrical properties of unobserved FLG allotropes of five, six and seven layers.

	$E(k)$	$E(n)$	DOS	$r_S \propto n^{\frac{-(p-1)}{2}}$	Δ (meV)	T_c (K)
SLG	$\propto k$	$\propto n^{1/2}$	$\propto n^{1/2}$	constant	0	0
BLG	$\propto k^2$	$\propto n$	constant	$\propto n^{-1/2}$	2	5
r-TLG	$\propto k^3$	$\propto n^{3/2}$	$\propto n^{-1/2}$	$\propto n^{-1}$	42	36
r-4LG	$\propto k^4$	$\propto n^2$	$\propto n^{-1}$	$\propto n^{-3/2}$	44-79	40

Table 6.1: Properties of SLG, BLG, r-TLG and r-4LG. Energy as a function of wave vector $E(k)$ and as a function of carrier density $E(n)$, density of states (DOS), the interaction parameter r_S, gap size Δ (meV) and critical temperature in T_c(K) are given for SLG, BLG, r-TLG and r-4LG. Δ and T_c are determined empirically by analyzing data gathered by the Jeanie Lau group.

6.6 Conclusion and references

In suspended rhombohedral-stacked tetralayer graphene, we observed an insulating state with giant interaction-induced energy gap, up to ~80 meV. This gap can be closed by increasing temperature, out-of-plane electric field and charge carrier density, and increased further by a magnetic field. The presence of this gap is similar to those observed in BLG and r-TLG, and arises from the correlated electron behavior that dominates near the CNP as the DOS and interaction parameter diverge. It is not clear, however, whether the trend of increasing gap size with number of layers will continue, as effects of screening, higher subbands and remote hopping parameters will increase in thicker samples and the k^N dispersion may no longer be a valid approximation.

References

1. Aoki, M. and Amawashi, H. Dependence of band structures on stacking and field in layered graphene. *Solid State Commun*. **142** (3), 123-127 (2007).

2. Grushina, A. L., Ki, D.-K., Koshino, M., Nicolet, A. A. L., Faugeras, C., McCann, E., Potemski, M., and Morpurgo, A. F. Insulating state in tetralayers reveals an even-odd interaction effect in multilayer graphene. *Nat. Commun.*, **6**, 6419 (2015).

3. Castro Neto, A. H., Guinea, F., Peres, N. M. R., Novoselov, K. S., and Geim, A. K. The electronic properties of graphene. *Rev. Mod. Phys.*, **81**, 109-163 (2009).

4. Zhang, Y., Tang, T.-T., Girit, C., Hao, Z., Martin, M. C., Zettl, A., Crommie, M. F., Ron Shen, Y., and Wang, F. Direct observation of a widely tunable bandgap in bilayer graphene. *Nature*, **459**, 820-823 (2009).

5. Bao, W., Velasco, J. Jr., Zhang, F., Jing, L., Standley, B. Smirnov, D., Bockrath, M., MacDonald, A. H., and Lau, C. N. Evidence for a spontaneous gapped state in ultraclean bilayer graphene. *Proc. Natl. Acad. Sci.*, **109** (27), 10802-10805 (2012).

6. Zhang, F., Sahu, B., Min, H., and MacDonald, A. H. Band structure of ABC-stacked graphene trilayers. *Phys. Rev. B*, **82**, 035409 (2010).

7. Bao, W., Jing, L., Velasco, J. Jr., Lee, Y., Liu, G., Tran, D., Standley, B., Aykol, M., Cronin, S. B., Smirnov, D., Koshino, M., McCann, E., Bockrath, M. and Lau, C. N. Stacking-dependent band gap and quantum transport in trilayer graphene. *Nat. Phys*. **7**, 948-952 (2011).

8. Lee, Y., Tran, D., Myhro, K., Velasco, J. Jr., Gillgren, N., Lau, C. N., Barlas, Y., Poumirol, J. M., Smirnov, D., and Guinea, F. Competition between spontaneous symmetry breaking and single-particle gaps in trilayer graphene. *Nat. Commun.*, **5**, 5656 (2014).

9. Pietronero, L., Strassler, S., Zeller, H. R., and Rice, M. J. Electrical conductivity of a graphite layer. *Phys. Rev. B*, **22**, 904-910 (1980).

10. Stauber, T., Peres, N. M. R., and Guinea, F. Electronic transport in graphene: A semi-classical approach including midgap states. *Phys. Rev. B*, **76**, 205423 (2007).

11. Hwang, E. H. and Das Sarma, S. Acoustic phonon scattering limited carrier mobility in 2D extrinsic graphene. *Phys. Rev. B*, **77**, 115449 (2008).

12. Chen, J.-H., Jang, C., Xiao, S., Ishigami, M., and Fuhrer, M. S. Intrinsic and extrinsic performance limits of graphene devices on SiO_2. *Nat. Nanotechnol.*, **3**, 206-209 (2008).

13. Efetov, D. K. and Kim, P. Controlling electron-phonon interactions in graphene at ultrahigh carrier densities. *Phys. Rev. Lett.*, **105**, 256805 (2010).

14. Li, J., Miranda, H. P. C., Niquet, Y.-M., Genovese, L., Duchemin, I., Wirtz, L., and Delerue, C. Phonon-limited carrier mobility and resistivity from carbon nanotubes to graphene. *Phys. Rev. B*, **92**, 075414 (2015).

15. Weitz, R. T., Allen, M. T., Feldman, B. E., Martin, J., and Yacoby, A. Broken-symmetry states in doubly gated suspended bilayer graphene. *Science*, **330**, 812-816 (2010).

16. Lee, Y., Myhro, K., Tran, D., Gilgren, N., Velasco, J. Jr., Bao, W., Deo, M., and Lau, C. N. Band gap and correlated phenomena in bilayer and trilayer graphene. Proc. of SPIE, 8725, 872506 (2013).

17. Velasco Jr., J., Lee, Y., Zhang, F., Myhro, K., Tran, D., Deo, M., Smirnov, D., MacDonald, A. H., and Lau, C. N. Competing ordered states with filling factor two in bilayer graphene. *Nat. Commun.*, **5**, 4550 (2014).

18. Lee, Y., Tran, D., Myhro, K., Velasco, J. Jr., Gillgren, N., Lau, C. N., Barlas, Y., Poumirol, J. M., Smirnov, D., and Guinea, F. Competition between spontaneous symmetry breaking and single-particle gaps in trilayer graphene. *Nat. Commun.*, **5**, 5656 (2014).

19. Lee, Y., Tran, D., Myhro, K., Velasco Jr., J., Gillgren, N., Poumirol, J. M., Smirnov, D., Barlas, Y., and Lau, C. N. Multicomponent quantum hall ferromagnetism and Landau level crossing in rhombohedral trilayer graphene. *Nano Lett.*, **16**, 227-231 (2016).

Chapter 7: Quantum Hall transport in suspended trilayer graphene

7.1   Introduction

We will begin this chapter by describing background on the quantum Hall effect (QHE) in single layer graphene (SLG) and few-layer graphene (FLG). Next, we will present quantum Hall (QH) transport data of suspended FLG, including Bernal-stacked trilayer graphene (B-TLG). Furthermore, we show QH transport with and without the use of a top gate in rhombohedral-stacked trilayer graphene (r-TLG). Finally, we will show evidence of multicomponent QH ferromagnetism and Landau level (LL) crossings in r-TLG.

7.2   The quantum Hall effect

From the classical Hall effect, for an electrical current flowing through a plane and subject to an out-of-plane magnetic field, a Hall voltage will be generated in the plane, orthogonal to the current. Due to the Lorentz force, electrons will take on cyclotron orbits in the plane, with a cyclotron frequency $\omega_B = eB/m$. From the Drude model, the expected resistivities in the longitudinal and Hall (transverse) directions to the current are $\rho_{xx} = \frac{m}{ne^2\tau}$ and $\rho_{xy} = \frac{B}{ne}$, respectively, where m is mass, n is charge density, e is the elementary charge, τ is the scattering time, and B is the magnetic field. In this classical model, the resistivity in the longitudinal direction scales inversely with charge density and the scattering time, meaning that cleaner samples with longer scattering times

will have larger conductivity, and the Hall resistivity scales linearly and continuously with B.

In the integer quantum Hall effect (IQHE), the Hall resistance becomes quantized, with the values $\rho_{xy} = \left(\frac{h}{e^2}\right)\frac{1}{\nu}$, where h is Planck's constant and ν is an integer indicating the number of filled Landau levels, called the filling factor. Thus ρ_{xy} changes stepwise with B, instead of a continuous, linear function in B. When the Hall resistivity rests on a quantized plateau, the longitudinal resistivity vanishes, $\rho_{xx} = 0$ (figure 7.1). Klaus von Klitzing was awarded the Nobel Prize in physics in 1985 for his 1980 discovery of the QHE in a silicon-based metal-oxide-semiconductor field-effect transistor (MOSFET)[1].
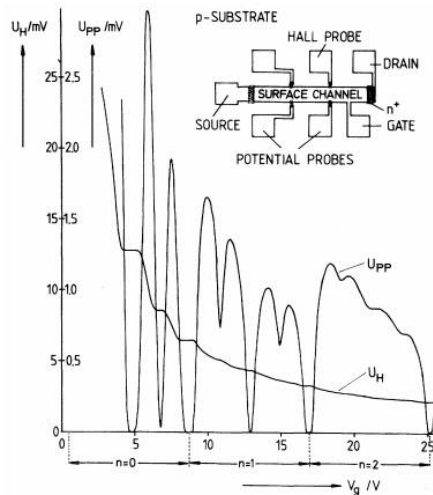
Figure 7.1: QHE in a silicon MOSFET. Longitudinal voltage U_{PP} and Hall voltage U_H plotted vs. gate voltage. The first three Landau levels $N = 0$, 1, and 2 are displayed on the voltage axis. Data taken at magnetic field $B = 18$ T, temperature $T = 1.5$ K, and source-drain current $I_{SD} = 1$ µA. Inset: schematic of the silicon MOSFET device. Image taken from ref. 1.

Since the first discovery of the IQHE in a silicon MOSFET, a staggering number of research papers have been published on both IQHE and fractional quantum Hall effect

(FQHE) in many different systems, including such materials as gallium arsenide heterostructures[2,3], single layer graphene[4,5], few-layer graphene[6-9], black phosphorus[10], transition metal dichalcogenides[11,12] (TMDs) and oxides[13,14].

7.3 The quantum Hall effect in single and few-layer graphene

7.3.1 The quantum Hall effect in single layer graphene

Electrons are confined to two dimensions (2D) in electronic transport measurements of single layer graphene (SLG). The so-called half-integer QHE was first observed in SLG by two separate research groups in 2005[4,5], in which conductivity was quantized in half integers of $4e^2/h$, as shown in figure 7.2a.
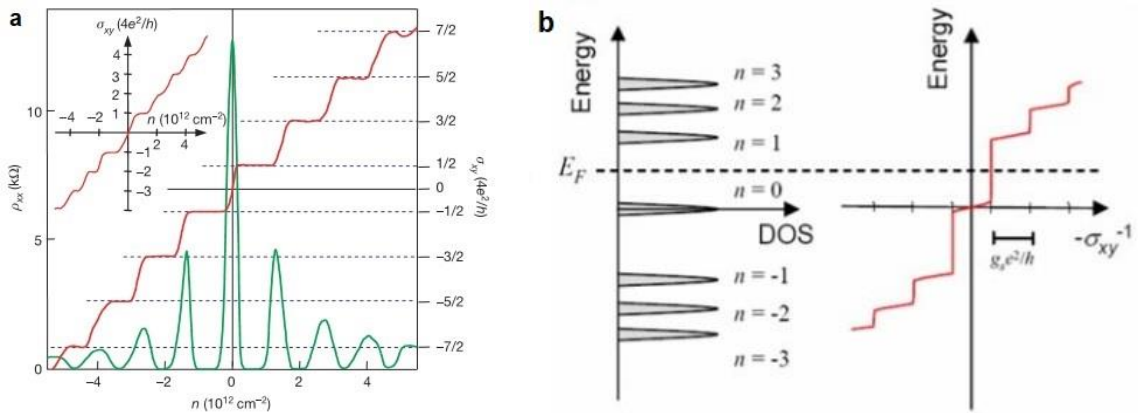
Figure 7.2: QHE in graphene. (a) QHE in SLG. Longitudinal resistivity ρ_{xx} in green and Hall conductivity σ_{xy} in red. $\rho_{xx} = 0$ when plateaus occur in σ_{xy}. Conductivity is quantized in half-integers of e^2/h. Inset: QHE in BLG. Hall conductivity σ_{xy}, quantized in integers of e^2/h. Image taken from ref. 4. (b) LL density of states and QH conductivity as a function of energy in SLG. Image taken from ref. 5.

The Landau level (LL) energy of SLG is given by[4]:

103

$$E_N^{SLG} = \pm v_F\sqrt{2e\hbar BN} \tag{7.1}$$

where $N=0, \pm1, \pm2...$ is the LL index. The lowest LL occurs at $N = 0$ and $E_{N=0} = 0$, shared equally by electrons and holes. Therefore, the QH conductivity in SLG[4] is

$$\sigma_{xy}^{SLG} = \pm 4\frac{e^2}{h}\left(N + \frac{1}{2}\right) \tag{7.2}$$

where the factor of 4 is due to the double-spin and double-valley degeneracy in graphene. The LL density of states (DOS) and the QH conductivity σ_{xy} are plotted as a function of energy for SLG in figure 7.2b. The broadening of the LL DOS is due to disorder in the system.

7.3.2 The quantum Hall effect in bilayer graphene

The QHE in BLG is similar to SLG, with conductivity plateaus occurring at integer values of $4e^2/h$, as shown in the inset in figure 7.2a. Another interesting feature about the BLG QHE is that there is a jump of 8 e^2/h across the charge neutrality point (CNP). The origin of this effect is due to the interlayer coupling γ_1 (shown in figure 2.3) which introduces a mass term into the Hamiltonian with a quadratic energy dispersion, a Berry's phase of 2π, and new energy eigenstates with a doubly-degenerate zero energy LL with $N=0$ and $N=1$[6]:

$$E_N^{BLG} = \pm\frac{\hbar eB}{m}\sqrt{N(N-1)} \tag{7.3}$$

where the mass m is given by equation 2.52. The QH conductivity in BLG is given by[6]:

$$\sigma_{xy}^{SLG} = \pm 4\frac{ve^2}{h} \tag{7.4}$$

Thus, the lowest Landau level (LLL) in BLG has an additional $N=0$ and $N=1$ orbital degeneracy, leading to the jump of 8 e^2/h at the CNP.

7.3.3 The quantum Hall effect in few-layer graphene

The lattice structure of B-TLG and r-TLG are shown in figures 2.5 and 2.6. Since the low energy Hamiltonian of B-TLG consists of a linear SLG branch and two quadratic BLG branches, as shown in equation 2.61, it makes sense that this so-called 2+1 model results in a QHE in B-TLG similar to a superposition of LLs from BLG and SLG[9,15,16]. Conversely, the QH effect is modified in r-TLG, such that charge carriers have a cubic energy dispersion, Berry's phase of 3π, and LL energies[7]:

$$E_N^{r-TLG} = \pm \frac{\left(v_F\hbar\sqrt{\frac{2eB}{hc}}\right)^3}{{\gamma_1}^2}\sqrt{N(N-1)(N-2)} \tag{7.5}$$

Now, r-TLG has a triply-degenerate zero-energy state for $N = 0$, 1, and 2. This results in a step of 12 e^2/h across the CNP, as shown in figure 7.3, with QH plateaus at values of $\pm6e^2/h$, $\pm10e^2/h$, ±14 e^2/h, and so on[7].
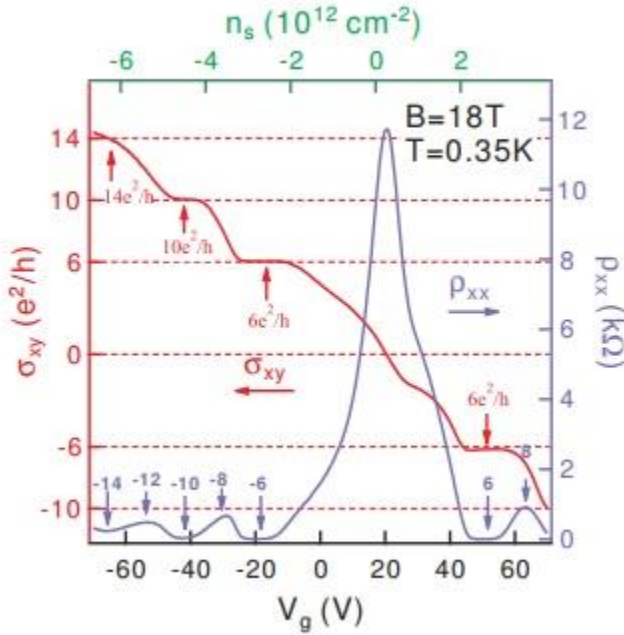
Figure 7.3: QHE in r-TLG. Hall conductivity σ_{xy} and longitudinal resistivity ρ_{xx} are plotted versus back gate voltage V_G and carrier density n_S. ρ_{xx} goes to zero when σ_{xy} platueas. Image taken from ref. 7.

7.4   Quantum Hall transport in suspended trilayer graphene

In this work, QH transport data is reported for both suspended B-TLG and r-TLG. Standard lock-in amplifier techniques are used to measure the two-terminal differential conductance $G = dI/dV_{SD}$, where we use an AC source-drain bias V_{SD}=50 µV, with a low frequency less than 200 Hz. Shubnikov-de Hass oscillations are seen at less than 1 T and QH plateaus are resolved at less than 2 T in most devices.

7.4.1 Quantum Hall transport in Bernal-stacked trilayer graphene

Broken symmetry QH states are observed in doubly-suspended B-TLG in this work. QH transport is measured for high-quality, doubly-suspended B-TLG devices at

liquid helium temperature with large B/T ratios. Similar behavior is seen in several high-quality devices with high mobility (>10,000 cm^2/Vs). Figure 7.4a shows the standard LL 'fan diagram' of the device, that is, G (color scale) as a function of V_{bg} (horizontal axis) and B (vertical axis). The QH plateaus appear as the colored bands that diverge from B=0 and the charge neutrality point (CNP). The small apparent curvature in the fan diagram for small B arises from the smeared crossing between MLG-like and BLG-like bands, which will be discussed further below. From the fan diagram, the back gate's coupling efficiency is estimated to be $\alpha_{BG} \sim 3.8 \times 10^{10}$ cm^{-2}/V, which also agrees with that calculated from device geometry.

To accentuate the evolution of the QH plateaus with V_{bg} and B, we plot $dG/dV_{bg}(V_{bg}, B)$ of the same data set in Figure 7.4b. The filling factor of each plateau, which appears as a white band, $\nu = n\hbar/Be = \alpha_{BG}V_{BG}h/Be$, is calculated from its slope in the $V_{BG}-B$ plane and labeled in Figure 7.4b. The most prominent feature is the very strong $\nu = -2$ plateau in the hole-doped regime, which is resolved at B as small as 0.25 T (here we define hole-doped and electron-doped regime to have negative and positive filling factors, respectively.) Line traces $G(V_{BG})$ at several B values for $B < 4.2$ T are shown in Figure 7.4c. When replotted as a function of ν, the traces nearly collapse into a single curve with properly quantized plateaus at $\nu = -2$, 2, 6, and 10. The appearance of robust $\nu = 6$ and 10 states agrees with equations 7.1 and 7.3 and prior reports[15,17,18]. On the other hand, our observation of the $\nu = 2$ and in particular the exceedingly robust $\nu = -2$ plateaus, is unexpected from equations 7.1 and 7.3. This can however be accounted for by the '2+1' model that takes remote hopping into account instead of MLG-like and
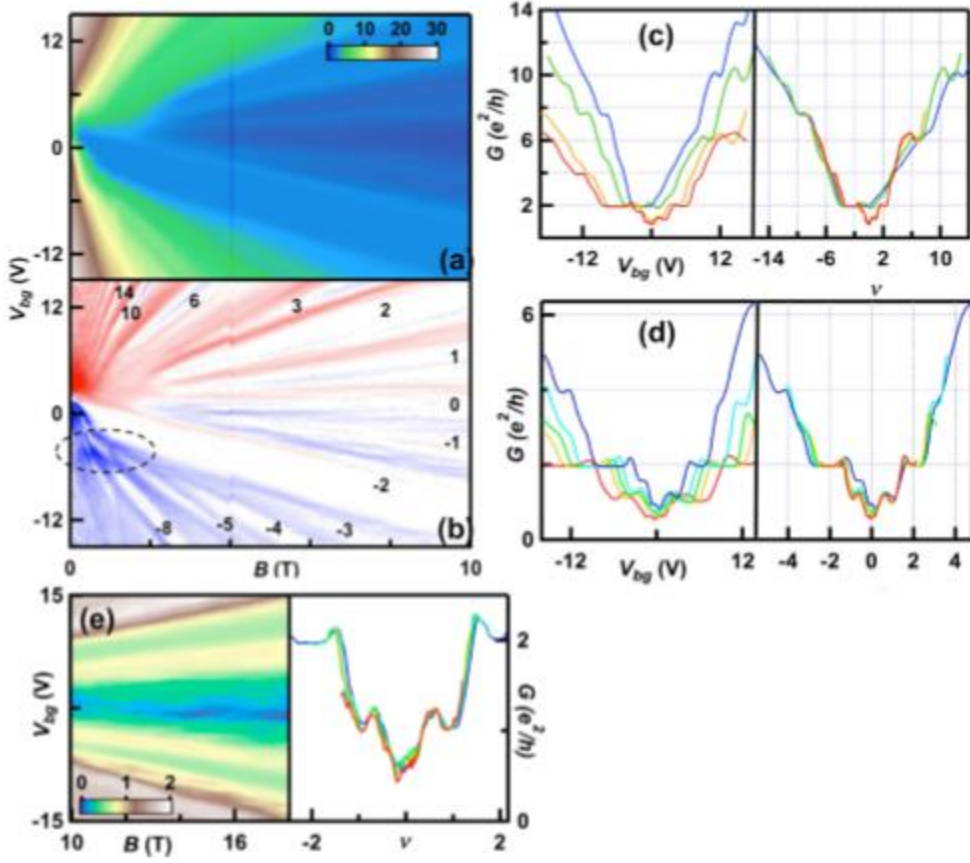
Figure 7.4: Landau fan diagram $G(V_{BG}, B)$ and line traces for B-TLG at low temperature. (a,b) $G(V_{BG}, B)$ and dG/dV_{BG} of a TLG device. Numbers indicate filling factors. The color scale in (a) indicates conductance in units of e2/ℏ. (c) $G(V_{BG})$ and $G(v)$ at B=1.5, 2.2, 3.5, and 4.2 T, respectively (from blue to red). (d) $G(V_{BG})$ and $G(v)$ at B=4.5, 6, 7, 8, and 10 T (from blue to red). (e) $G(V_{BG}, B)$ and $G(v)$ at B=10, 12, 14, 16 and 18 T (from blue to red). Image taken from ref. 16.

BLG-like bands both touching at a single point, including next-nearest hopping

parameters (γ_2 and γ_5) leads to bands that are individually gapped, with a relative vertical

offset between the MLG-like and BLG-like bands, whose tops of valence bands are

located at $-\gamma_2/2$ and $\gamma_2/2$, respectively. Consequently, the LL spectrum of such a band

structure is modified from equations 7.1 and 7.3 as follows: (i) since ABA stacked TLG

obeys mirror symmetry but not inversion symmetry[19], its valley degeneracy is not protected; the broken valley degeneracy of the lowest LL[19] manifests as $v = \pm 2$ plateaus, as observed experimentally; (ii) the spectrum is particle-hole asymmetric; and (iii) LLs originating from the MLG-like and BLG-like bands cross at energy $\sim \pm \gamma_2 / 2$.

All three features are observed in our experimental data. Apart from the robust $v = \pm 2$ plateaus, the particle-hole asymmetry is clearly reflected in the sequence of resolved plateaus; the $v = 6$ and 10 plateaus are observed only in the electron doped regime and $v = -8$ is observed solely in the hole-doped regime. The dark blue feature at $V_{bg} \sim -5$ V, indicated by the dotted circle in Figure 7.4b, corresponds to the crossings between LLs that belong to the MLG and BLG-like spectra[19]. From the data, the crossings occur at $\sim -1.9 \times 10^{11}$ cm^{-2}, corresponding to ~ -8 meV. Thus, our data suggest $\gamma_2 \sim -16$ meV in TLG, in reasonable agreement with the value from bulk graphite[20], -20 meV.

Thus far the $v = -2$, 2, 6, and 10 plateaus are well accounted for by single particle tight binding calculations, using values of hopping parameters obtained from graphite. (The absence of the $v = -6$ state is an experimental surprise and currently not understood). At larger B, we also observe additional plateaus at $v = \pm 1, \pm 3, -4$, and -5, which indicate almost complete lifting of spin, valley and orbital degeneracies in the lowest LL. The $v = 0$ plateau, although resolved, is ~ 0.3 e^2/$\hbar$ at 18 T. This lack of true insulating behavior is likely due to the presence of small amount of residual impurities. Figure 7.4d plots $G(V_{BG})$ and $G(v)$ at B=4.5, 6, 7, 8 and 10 T, respectively, showing satisfactory conductance quantization. The $v = \pm 1$ plateaus are resolved at B as low as 4.5 T and persists to 18 T (figure 7.4e), the highest available field. These additional plateaus,

particularly those at odd filling factors, cannot be accounted for by any tight binding

model or simple breaking of layer symmetry due to the presence of an out-of-plane

electric field. Instead, the plateaus' appearance at high B values in samples with high

mobility ($\geq$10000 cm^2/(Vs)) strongly suggests symmetry breaking arising from electronic

interactions. In fact, they can be qualitatively understood in terms of QH ferromagnetism

and Hund's rule-like filling of the 12-fold degenerate lowest LL[21]. Within this model, the

LLs between $v = -6$ and 6 are filled in the order of maximizing spin, chirality (BLG-like

branch first), valley, and orbital indices. At large B, the $v = -5, -4, -3, -2, 1, 2$, and 3

states belong to the BLG-like branch, while the $v = -1, 0, +4$, and $+5$ states to the MLG-

like branch[22]. (The $v = 4$ and $v = -2$ are marginal cases as they separates a series of

bilayerlike LL's and a series of monolayer-like LL's. For instance, at $v = 4$, for positive

energies the last $N = 0$ bilayer-like LL is filled or the first $N = 0$ MLG-like LL is empty.)

As observed experimentally, all the BLG-like states are fully resolved, whereas only the v

$= -1$ (and to some extent the $v = 0$) state in the SLG-like branches is observed.

7.4.2 Quantum Hall transport in rhombohedral-stacked trilayer graphene with and without the use of a top gate

We turn our attention toward suspended r-TLG with dual gates. Here, we report

transport data[23] of an r-TLG device with a field effect mobility of 42,000 cm^2/Vs at 270

mK in a He^3 cryomagnet. As shown in Figure 7.5a, which plots two terminal conductance

$G(B, v)$ in units of e^2/h with top gate disconnected or grounded, QH plateaus appear as

vertical bands. As B increases, QH plateaus at filling factors $v = -5$ and -3 are resolved

first, followed by −1 and −2. This can be more clearly seen in the line traces $G(v)$: only the $v = -3$ plateau are fully resolved at $B = 4.5$T, whereas additional plateaus at $v = -2$ and −1 are resolved at $B = 5.5$ T (figure 7.5b).
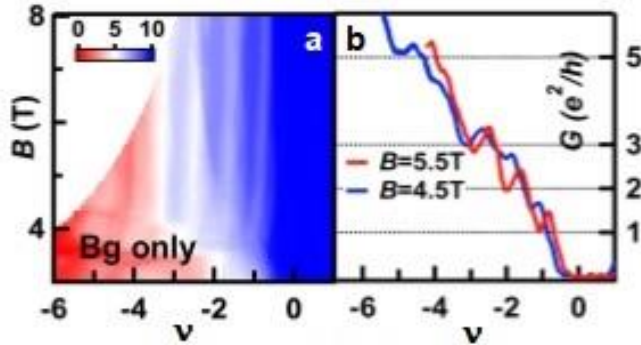
Figure 7.5. Transport data in suspended r-TLG devices with back gate applied voltage only: (a) $G(B, v)$ of an r-TLG device with only back gate engaged. (b) Line traces $G(v)$ at B=4.5 and 5.5 T, respectively. Image taken from ref. 23.

These results are fully consistent with a prior work using singly gated devices[24]. However, in the above measurement with only a single gate, $U_\perp$ is not controlled but scales with n. When we carefully control both $U_\perp$ and n, a qualitatively different picture emerges. Figure 7.6a,b plots $G(B, v)$ at $U_\perp$=0 and −20 mV, respectively, and line traces at $B = 5$ T are shown in Figure 7.6c,d. At $U_\perp$= −20 mV, the $v = -3$ (but not the $v = -2$) state is resolved (figure 7.6b,d) in an apparent agreement with the Hund's rule, again qualitatively similar to data from singly gated studies (figure 7.5a,b and ref 24). However, in the absence of interlayer bias the plateaus at $v = -6$ are first resolved (as expected), followed by (unexpectedly) − 4 and −2 that are fully resolved at $B = 5$ T; the odd integer plateaus $v = -3$ and −1 appear only as small shoulders even at $B = 8$ T.
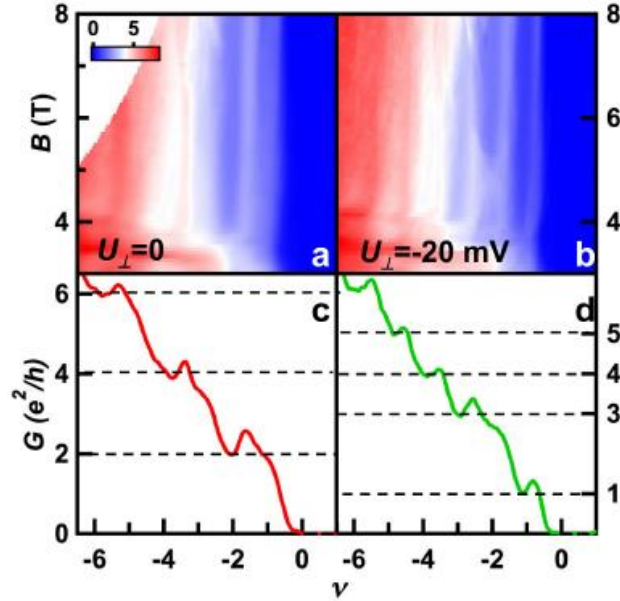
Figure 7.6. Electric transport in a doubly-suspended r-TLG device with top gate used to fix interlayer potential: (a,c). $G(B, v)$ in units of e^2/h at $U_\perp = 0$, and line traces $G(v)$ at $B = 5$ T. (b,d). Similar data at $U_\perp = -20$ mV. Image taken from ref. 23.

7.4.3 Multicomponent quantum Hall ferromagnetism and Landau level crossing in rhombohedral-stacked trilayer graphene

As shown in the previous section, the exact sequence of plateaus depends strongly on $U_\perp$, thus the exact symmetries of QH states cannot be inferred from singly gated devices. In particular, for charge-balanced r-TLG the orbital pseudospin is maximized first, that is, the triple orbital degeneracy is broken prior to that of spin and valley; this suggests that the conventional Hund's rule does not apply in this system. This indicates that either interactions are spin and valley dependent or that single particle hopping terms can influence the broken symmetry sequence. To further investigate the plateaus' dependence on $U_\perp$ we measure $G(U_\perp, v)$ at constant B. The resolved QH plateaus appear

as an array of bands centered at integer values of v with a striking network of staggered 'hexagons' (figure 7.7a,b).
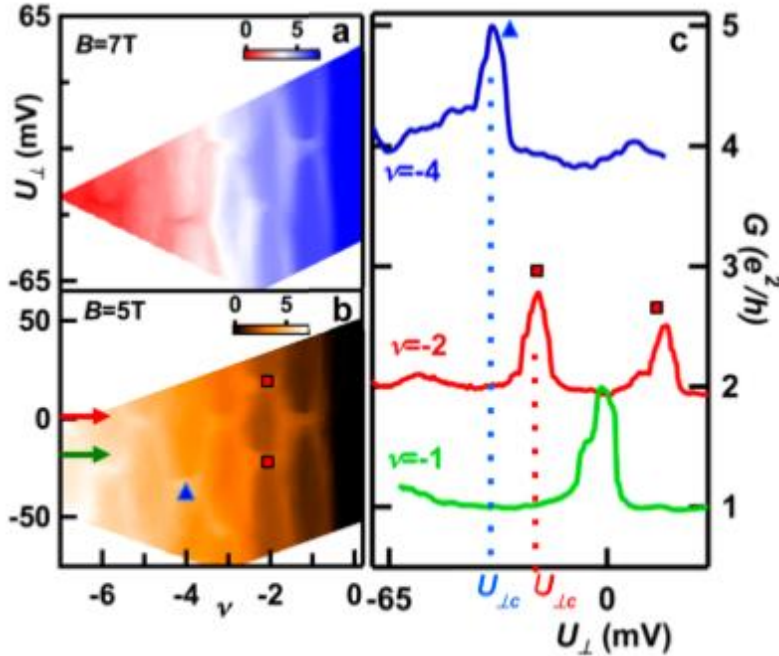
Figure 7.7. Quantum Hall transport data in r-TLG at varying interlayer potential: (a,b). $G(U_\perp, v)$ in units of e^2/h at $B = 7$ and 5 T, respectively. The arrows indicate line traces along which Figure 7.6c,d would be taken. (c). Line traces $G(U_\perp)$ at $B = 5$ T and $v = -1, -2$, and -4. The triangle and squares mark $U_{\perp C}$ values at which G is not quantized. Image taken from ref. 23.

As B increases, the sizes of these hexagons grow accordingly. G is properly quantized at ve^2/h except at certain critical $U_{\perp C}$ values that yield the horizontal 'ridges' of the hexagons. For instance, at $v = -1$, G is quantized at $1e^2/h$ except near $U_\perp = 0$ mV (Figure 7.7c, green curve); at $v = -2$ and $v = -4$ states, quantization is lost at $U_{\perp C} \sim \pm 18$ mV (red curve) and $U_{\perp C} \sim 35$ mV (blue curve), respectively, and the corresponding $U_{\perp C}$ values are indicated by red squares and blue triangles. Consequently, a given plateau is resolved (unresolved) if $G(v)$ is taken at $U_\perp \neq U_{\perp C}$ ($U_\perp = U_{\perp C}$), that is, the line traces in

figure 7.6c,d are effectively taken along the red and green arrows in figure 7.7b, respectively. Our experimental results demonstrate the presence of QH ferromagnetic states in r-TLG and enable us to determine the symmetries of the states at intermediate filling factors. One combination of the spin-valley degrees of freedom is lifted first, leading to the layer antiferromagnetic state at $v = 0$. This is followed by the breaking of the orbital degeneracy and the appearance of the even integer states at $v = -2$ and -4. Finally, in the presence of finite $U_\perp$ that breaks the inversion symmetry, the remaining spin-valley symmetries are broken and the odd integer states are resolved. Schematic of the symmetries of the QH states in the lowest LL is shown in Figure 7.8a.

Within the QH ferromagnetism, the hexagon patterns can be naturally accounted for by a model of crossings between LLs[25-27], whose energies depend on both $U_\perp$ and B. In the zeroth LL of the two-band model, only the A (B) sublattice of the top (bottom) layer are relevant for low-energy considerations. We thus ignore the contribution of the middle layer, and treat layer, valley, and sublattice indices as equivalent. Hence, energies of LLs that are partially localized to the top (bottom) layer increase (decrease) with increasing $U_\perp$; these two sets of LLs cross whenever the difference in LL energies are compensated by the externally applied interlayer potential. At a given v, G is quantized properly except at the crossing points. Using LL spectra similar to that depicted in figure 7.8a, we model the density of states of each LL as a Lorentzian and calculate the total density of states of the system as a function of n and $U_\perp$. The simulation result reproduces the observed 'hexagon' patterns (figure 7.8b), confirming the presence of multiple LL crossings driven by $U_\perp$ in the QH regime.
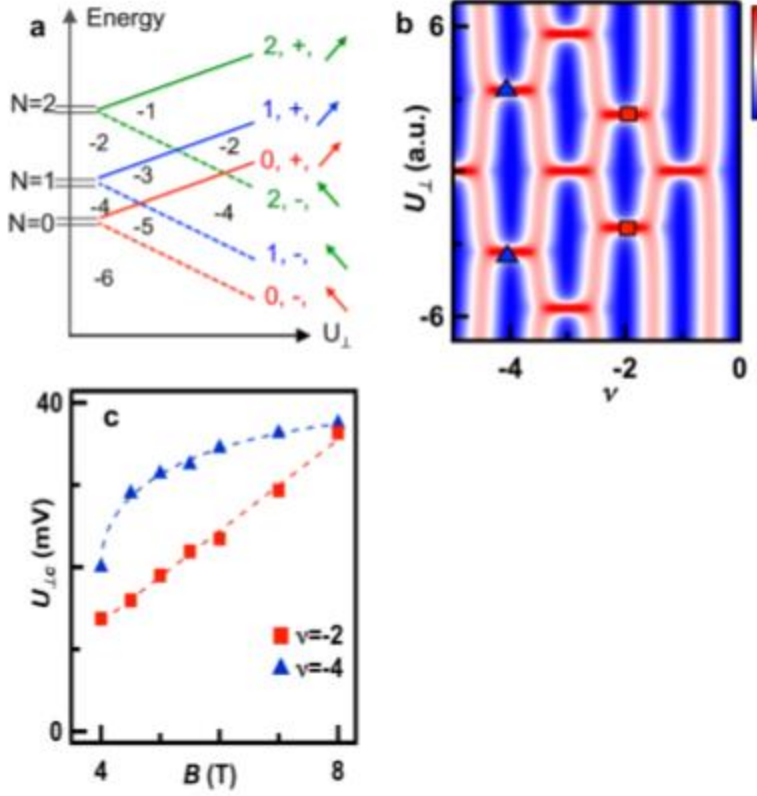
Figure 7.8. LL crossings and the $v = -2, -4$ LL gaps in r-TLG: (a). Schematic diagram of LL evolution with $U_\perp$ and the resultant QH states in the hole-doped regime. Colored numbers, $\pm$, and arrows indicate orbital, valley, and spin indices. (b). Simulated total density of states versus $U_\perp$ and v. Color scale: blue (low), red (high). (c). Measured $U_{\perp C}(B)$ for $v = -2$ and -4 states, respectively. The dotted lines are guides to the eye. Image taken from ref. 23.

In principle, we can determine the LL gaps Δ from $U_{\perp C}$ at the LL crossing points, where the differences in LL energies are compensated by electrostatic energy. However, here $U_\perp$ is the externally imposed potential bias and will be heavily screened[28-30] even in the QH regime. Thus, one expects that $\Delta(B) = U_\perp^S(B) \ll U_\perp$, where $U_\perp^S$ is the screened interlayer potential. Extracting the exact magnitude of Δ from the crossing points is nontrivial and will be the focus of future studies. Nevertheless, we do not expect

screening to significantly alter the functional dependence of $U_\perp(B)$. Hence insight into the nature of the broken-symmetry QH states in the lowest LL can be obtained by examining the dependence of $U_{\perp C}$ on B.

To this end, we plot $U_{\perp C}(B)$ for crossings observed at $v = -2$ and -4 in figure 7.8c. Interestingly, $U_{\perp C}(B)$ is linear in B for $v = -2$ state but markedly sublinear for the $v = -4$ state. Thus, the data in figure 7.8d suggest that the LL gap of the $v = -2$ state scales linearly with B, whereas that of the $v = -4$ state is sublinear in B. The different scaling behaviors in B for the $v = -2$ and $v = -4$ gaps suggest different mechanisms of gap generation. In particular, the remote hopping term γ_4 in r-TLG, which is the interlayer hopping energy between stacked-unstacked sublattices, may also lead to splitting of the orbital degeneracy of the zeroth LL. This effect can be captured in an effective two-band model[31], evaluated in the perturbation theory:

$$H_{\gamma 4} = \left\{ \frac{\sqrt{3} a v_F}{\hbar} \left(\frac{\gamma_4}{\gamma_1} \right) \right\} \begin{bmatrix} \pi^\dagger \pi & 0 \\ 0 & \pi \pi^\dagger \end{bmatrix} \tag{7.6}$$

where $a = 0.246$ nm is the lattice constant, and $\pi = p_x + i p_y$. In the presence of B, $H_{\gamma 4}$ leads to a splitting of the $N = 0$, 1, and 2 LL orbitals. Such splitting of the orbital pseudospin has an energy gap $\Delta_{\gamma 4}$ that scales linearly with B and leads to QH plateaus at $v = \pm 2$, as observed experimentally. In fact, ignoring other remote hopping parameters, reasonable agreement between experimental data and LL spectrum can be obtained by using $\gamma_4 \sim 0.1 \gamma_1$, though this crude estimate may be modified by other hopping terms and by the nonzero potential at the middle layer. On the other hand, the sublinear behavior for

the $v = -4$ state suggests an origin of electronic interactions, which lifts the spin-valley degeneracy and is expected to scale with $B^{1/2}$.

The contrasting behavior of the in the scaling gaps of the $v = -2$ and $v = -4$ states suggest that both the single particle remote hopping terms and electron−electron interactions in the zeroth LL must be included to account for the broken symmetries in the zeroth LL. We also find that the addition of the remote hopping terms can significantly influence the Hund's rules determining the Hall plateau sequence of the broken symmetry states. Taken together, our data suggest that the $v = -2$ and -4 QH states are orbital pseudospin polarized canted antiferromagnetic states, whereas the $v = -1, -3$, and -5 states, resolved only in the presence of finite $U_\perp$, are layer/spin polarized. Further theoretical and experimental studies, such as those using samples with even higher quality, or graphene/hexagonal boron nitride heterostructures[32] for measurements of LL gaps and crossings for large ranges of magnetic field, electric field, and charge densities, are needed to understand the mechanism of gap generation in the orbital pseudospin indices and to help determine the precise values of remote hopping parameters in few-layer graphene.

7.5   Conclusion and references

Few-layer graphene is shown to be an excellent platform to explore QHE. In particular, our QH transport data revealed a trend of strong LL crossings in B-TLG, with a robust $v = -2$ state, indicative of the so-called '2+1' model in B-TLG, which resembles the superposition of both the quadratic bilayer-like and linear monolayer-like sub-bands.

The QH transport data in r-TLG was observed to be remarkably different than B-TLG, with an intrinsic insulating state and evidence of multicomponent QH ferromagnetism. Furthermore, investigations of the QH states in r-TLG as a function of out-of-plane electric field provided information on the order of symmetry-breaking processes, and that both single particle hopping parameters and electron-electron interactions must be included in the zeroth LL to account for the broken symmetries observed.

References

1. Klitzing, K. v., Dorda, G. and Pepper, M. New method for high-accuracy determination of the fine-structure constant based on quantized Hall resistance. *Phys. Rev. Lett*. **45** (6), 494-497 (1980).

2. Willett, R., Stormer, H. L., Tsui, D. C., Gossard, A. C., English, J. H., and Baldwin, K. W. Fractional quantum Hall effect in extremely high mobility GaAs/(AlGa)As heterostructures. *Surf. Sci.*, **196** (1), 257-262 (1988).

3. Arapov, Y. G., Gudina, S. V., Klepikova, A. S., Neverov, V. N., Harus, G. I., Shelushinina, N., and Yakunin, M. V. Quantum Hall plateau-plateau transitions in n-InGaAs/GaAs heterostructures before and after IR illumination. *Low Temp. Phys.*, **4** (2), 106-111 (2015).

4. Novoselov, K. S., Geim, A. K., Morozov, S. V., Jiang, D., Katsnelson, M. I., Grigorieva, I. V., Dubonos, S. V., and Firsov, A. A. Two-dimensional gas of massless Dirac fermions in graphene. *Nature*, **438** (10), 197-200 (2005).

5. Zhang, Y., Tan, Y.-W., Stormer, H. L., and Kim, P. Experimental observation of the quantum Hall effect and Berry's phase in graphene. *Nature*, **438** (10), 201-204 (2005).

6. Novoselov, K. S., McCann, E., Morozov, S. V., Fal'ko, V. I, Katsnelson, M. I., Zeitler, U., Jiang, D., Schedin, F., and Geim, A. K. Unconventional quantum Hall effect and Bery's phase of 2π in bilayer graphene. *Nat. Phys.*, **2**, 177-180 (2006).

7. Zhang, L., Zhang, Y., Camacho, J., Khodas, M., and Zaliznyak, I. The experimental observation of quantum Hall effect of *l=3* chiral quasiparticles in trilayer graphene. *Nat. Phys.*, **7**, 953-957 (2011).

8. Grushina, A. L., Ki, D.-K., Koshino, M., Nicolet, A. A. L., Faugeras, C., McCann, E., Potemski, M., and Morpurgo, A. Insulating state in tetralayers reveals an even-odd interaction effect in multilayer graphene. *Nat. Commun.*, **6**, 6419 (2015).

9. Stepanov, P., Barlas, Y., Espiritu, T., Che, S., Watanabe, K., Taniguchi, T., Smirnov, D., and Lau, C. N. Tunable symmetries of integer and fractional quantum Hall phases in heterostructures with multiple Dirac bands. Phys. Rev. Lett., 117, 076807 (2016).

10. Li., L., Yang, F., Ye, G. J., Zhang, Z., Zhu, Z., Lou, W., Zhou, X., Watanabe, K., Taniguchi, T., Chang, K., Wang, Y., Chen, X. H. and Zhang, Y. Quantum Hall effect in black phosphorus two-dimensional electron system. *Nat. Nanotechnol.*, **11**, 593-597 (2016).

11. Li, X., Zhang, F., and Niu, Q. Unconventional quantum Hall effect and tunable spin hall effect in Dirac materials: Application to an isolated MoS_2 trilayer. *Phys. Rev. Lett.*, **110**, 066803 (2013).

12. Xu, S., Shen, J., Long, G., Wu, Z., Bao, Z., Liu, C.-C., Xiao, X., Han, T., Lin, J., Wu, Y., Lu, H., Hou, J., An, L., Wang, Y., Cai, Y., Ho, K. M., He, Y., Lortz, R., Zhang, F., and Wang, N. Odd-integer quantum Hall states and giant spin susceptibility in *p*-type few-layer WSe_2. *Phys. Rev. Lett.*, **118**, 067702 (2017).

13. Tsukazaki, A., Ohtomo, A., Kita, T., Ohno, Y., Ohno, H., and Kawasaki, M. Quantum Hall effect in polar oxide heterostructures. *Science*, **315** (5817), 1388-1391 (2007).

14. Tsukazaki, A., Akasaka, S., Nakahara, K., Ohno, Y., Ohno, H., Maryenko, D., Ohtomo, A., and Kawasaki, M. Observation of the fractional quantum Hall effect in an oxide. *Nat. Mater.*, **9**, 889-893 (2010).

15. Taychatanapat, T., Watanabe, K., Taniguchi, T., and Jarillo-Herrero, P. Quantum Hall effect and Landau level crossing of Dirac fermions in trilayer graphene. *Nat. Phys.*, **7**, 621-625 (2011).

16. Lee, Y., Velasco Jr., J., Tran, D., Zhang, F., Bao, W., Jing, L., Myhro, K., Smirnov, D., and Lau, C. N. Broken symmetry quantum Hall states in dual-gated ABA trilayer graphene. *Nano Lett.*, **13**, 1627-1631 (2013).

17. Henriksen, E. A., Nandi, D., and Eisenstein, J. P. Quantum Hall effect and semimetallic behavior of dual-gated ABA-stacked trilayer graphene. *Phys. Rev. X*, **2**, 011004 (2012).

18. Khodkov, T., Withers, F., Hudson, D. C., Craciun, M. F., and Russo, S. Electrical transport in suspended and double gated trilayer graphene. *Appl. Phys. Lett.*, **100**, 013114 (2012).

19. Koshino, M. and McCann, E. Landau level spectra and the quantum Hall effect of multilayer graphene. *Phys. Rev. B*, **83**, 165443 (2011).

20. Dresselhaus, M. S. and Dresselhaus, G. Intercalation compounds of graphite. *Adv. Phys.*, **51**, 1-186 (2002).

21. Zhang, F., Tilahun, D., and MacDonald, A. H. Hund's rules for the N=0 Landau levels in trilayer graphene. *Phys. Rev. B*, **85**, 165139 (2012).

22. Ezawa, M. J. Intrinsic Zeeman effect in graphene. *Phys. Soc. Jpn.*, **76**, 094701 (2007).

23. Lee, Y., Tran, D., Myhro, K., Velasco Jr., J., Gillgren, N., Poumirol, J. M., Smirnov, D., Barlas, Y., and Lau, C. N. Multicomponent quantum hall ferromagnetism and Landau level crossing in rhombohedral trilayer graphene. *Nano Lett.*, **16**, 227-231 (2016).

24. van Elferen, H. J., Veligura, A., Tombros, N., Kurganova, E. V., van Wees, B. J., Maan, J. C., and Zeitler, U. Fine structure of the lowest Landau level in suspended trilayer graphene. *Phys. Rev. B*., **88** (12), 121302 (2013).

25. Zhang, X. C., Faulhaber, D. R., and Jiang, H. W. Multiple phases with the same quantized Hall conductance in a two-subband system. *Phys. Rev. Lett.*, **95**, 216801 (2005).

26. Sanchez-Yamagishi, J. D., Taychatanapat, T., Watanabe, K., Taniguchi, T., Yacoby, A., and Jarillo-Herrero, P. Quantum Hall effect, screening, and layer-polarized insulating states in twisted bilayer graphene. *Phys. Rev. Lett.*, **108**, 076601 (2012).

27. Lee, K., Fallahazad, B., Xue, J., Taniguchi, T., Watanabe, K., and Tutuc, E. Bilayer graphene. Chemical potential and quantum Hall ferromagnetism in bilayer graphene. *Science*, **345**, 58-61 (2014).

28. Van Gelderen, R., Olsen, R., and Smith, C. M. Screening in multilayer graphene. *Phys. Rev. B*, **88**, 115414 (2013).

29. Koshino, M. Interlayer screening effect in graphene multilayers with ABA and ABC stacking. *Phys. Rev. B*, **81**, 125304 (2010).

30. Min, H., Hwang, E. H., and Das Sarma, S. Polarizability and screening in chiral multilayer graphene. *Phys. Rev. B*, **86**, 081402(R) (2012).

31. Zhang, F., Sahu, B., Min, H., and MacDonald, A. H. Band structure of ABC-stacked graphene trilayers. *Phys. Rev. B*, **82**, 035409 (2010).

32. Dean, C. R., Young, A. F., Meric, I., Lee, C., Wang, L., Sorgenfrei, S., Watanabe, K., Taniguchi, T., Kim, P., Shepard, K. L., and Hone, J. Boron nitride substrates for high-quality graphene electronics. *Nat. Nanotechnol.*, **5**, 722-726 (2010).

Chapter 8: Conclusion and outlook

8.1　Conclusion

In this thesis, we have investigated the electronic and mechanical properties of suspended few-layer graphene (FLG) membranes through *in situ* scanning electron microscope (SEM) imaging and low temperature electronic transport measurements. In situ SEM imaging of graphene membranes suspended over pre-defined trenches revealed that electrostatically-induced deflection is reversible and elastic with minimal hysteresis, up until the point at which graphene irreversibly collapses, and that this parabolic deformation causes inhomogeneous strain and charge carrier density n. Also, due to its negative thermal expansion coefficient, graphene expands at low temperature, creating ripples in the bulk and butterfly features on the free-standing edges.

The electrical studies of rhombohedral-stacked few-layer graphene (r-FLG) samples are motivated by their peculiar energy dispersions that, at low energies, scale as k^N for N number of layers. Fabricated by a multi-level electron beam lithography process and wet etching in HF, the FLG membranes are suspended between electrons, below an "air-bridge" top gate and above a Si back gate. This dual-gated geometry allows us to decouple the out-of-plane electric field $E_\perp$ and n. High mobility r-FLG devices are intrinsically insulating in the absence of external fields, with gap sizes of 2, 40, and 80 meV in BLG, rhombohedral-stacked tri- (r-TLG) and tetralayer graphene (r-4LG), respectively. This insulating state is consistent with a layer antiferromagnetic (LAF) phase which breaks time reversal symmetry, which transitions or crosses over to quantum valley Hall and ferromagnetic states under sufficiently-large $U_\perp$ and $B_{/\!/}$, respectively.

These results underscore the strong electronic interactions and rich physics in high quality FLG devices in the low density limit.

8.2   Outlook

Despite progress made in this thesis, several questions remain unanswered. For instance, will the trend of increasing gap size with number of layers terminate; if so, at which thickness? Is LAF the ground state in r-FLG? Can other phases be achieved? Further experimental and theoretical studies are necessary to address these questions.

Since the discovery of graphene, the field has expanded to include other monolayer or few-layer two dimensional (2D) materials, such as transition metal dichalcogenides or black phosphorus. The procedures described in chapter three to fabricate suspended graphene devices can be extended to other 2D materials as well. New, suspended device structures may be adopted from these fabrication recipes, such as *p-n* junctions through split top gates, electronic Vaselago lenses, quantum dots, and photo-thermoelectric devices. Our *in situ* SEM imaging techniques can be adopted for similar studies and electrical, mechanical, thermal and strain engineering in similar devices. Another development in the field is the use of hexagonal boron nitride (hBN) as substrates or encapsulating layers, for fabricating robust and high mobility samples. A number of interesting phenomena has been observed, including Coulomb drag[1-3], electron tunneling through thin hBN tunnel barriers[4], gate-tunable negative differential resistance in hBN-encapsulated single- and bilayer graphene[5,6], and Shubnikov-de Haas oscillations

in TMDs[7] and fractional quantum Hall effect in graphene[8] encapsulated in hBN. Many

new materials and heterostructures await exploration.

8.3   References of the conclusion

1. Kim, S., Jo, I., Nah, J., Yao, Z., Banerjee, S. K., and Tutuc, E. Coulomb drag of massless fermions in graphene. *Phys. Rev. B*, **83**, 161401(R), (2011).

2. Titov, M., Gorbachev, R. V., Narozhny, B. N., Tudorovskiy, T., Schutt, M., Ostrovsky, P. M., Gornyi, I. V., Mirlin, A. D., Katsnelson, M. I., Novoselov, K. S., Geim, A. K., and Ponomarenko, L. A. Giant magnetodrag in graphene at charge neutrality. *Phys. Rev. Lett.*, **111**, 166601 (2013).

3. Li, J. I. A., Taniguchi, T., Watanabe, K., Hone, J., Levchenko, A., and Dean, C. R. Negative Coulomb drag in double bilayer graphene. *Phys. Rev. Lett.*, **117**, 046802 (2016).

4. Britnell, L., Gorbachev, R. V., Jalil, R., Belle, B. D., Schedin, F., Katsnelson, M. I., Eaves, L, Morozov, S. V., Mayorov, A. S., Peres, N. M. R., Castro Neto, A. H, Leist, J., Geim, A. K., Ponomarenko, L. A., and Novoselov, K. S. Electron tunneling through ultrathin boron nitride crystalline barriers. *Nano Lett.*, **12**, 1707-1710 (2012).

5. Wu, Y., Farmer, D. B., Zhu, W., Han, S.-J., Dimitrakopoulos, C. D., Bol, A. A., Avouris, P., and Lin, Y.-M. Three-terminal graphene negative differential resistance devices. *ACS Nano*, **6**, 2610-2616 (2012).

6. Burg, G. W., Prasad, N., Fallahazad, B., Valsaraj, A., Kim, K., Taniguchi, T., Watanabe, K., Wang, Q., Kim, M. J., Register, L. F., and Tutuc, E. Coherent interlayer tunneling and negative differential resistance with high current density in double bilayer graphene-WSe$_2$ heterostructures. *Nano Lett.*, **17**, 3919-3925 (2017).

7. Cui, X., Lee, G.-H., Kim, Y. D., Arefe, G., Huang, P. Y., Lee, C.-H., Chenet, D. A., Zhang, X., Wang, L., Ye, F., Pizzocchero, F., Jessen, B. S., Watanabe, K., Taniguchi, T., Muller, D. A., Low, T., Kim, P., and Hone, J. Multi-terminal transport measurements of MoS2 using a van der Waals heterostructure device platform. *Nat. Nanotechnol.*, **10**, 534-540 (2015).

8. Dean, C. R., Young, A. F., Cadden-Zimansky, P., Wang, L., Ren, H., Watanabe, K., Taniguchi, T., Kim, P., Hone, J., and Shepard, K. L. Multicomponent fractional quantum Hall effect in graphene. *Nat. Phys.*, **7**, 693-696 (2011).

Appendix A: RGS value of hexagonal boron nitride and transport statistics

A.1 Thickness dependence of the RGS value of hexagonal boron nitride

In chapter three, a correlation was found between the relative green shift (*RGS*) value and the number of layers of graphene, as shown in equation 3.1 and table 3.1. This correlation was readily observed using optical contrast under an optical microscope. Similarly, a correlation has been discovered in measuring the thickness of several layers of hexagonal boron nitride (hBN). Figure A.1 plots the thickness of hBN measured with an atomic force microscope (AFM) versus the *RGS* value of the hBN flakes measured with a standard optical microscope, using equation 3.1.
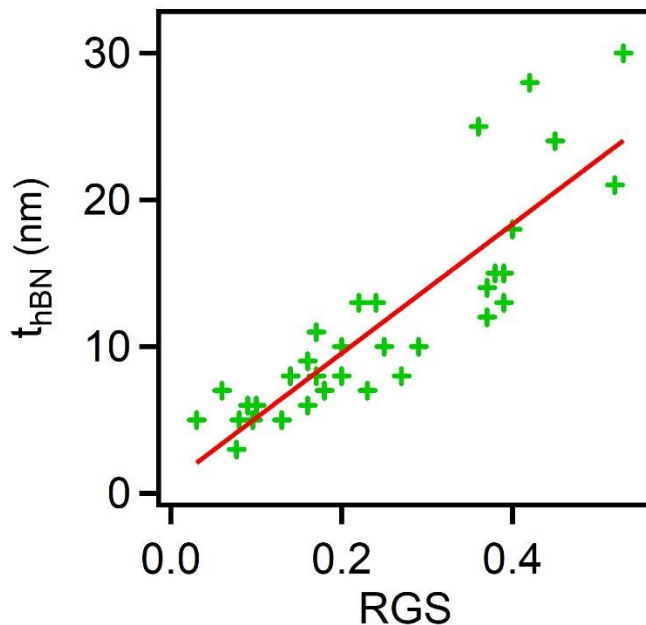

Figure A.1. *RGS* dependence on the thickness of hBN: Thickness of hBN measured with an AFM v. *RGS* value. A linear fit, $y = mx + b$, is made using 38 data points, with fitting parameters m = 43.92 ±3.99 and b = 0.75 ±1.07.

Performing a best linear fit on the scatter plot of 38 data points in figure A.1, a relation is determined to estimate the thickness of exfoliated hBN:

$$t_{hBN} = RGS \; x \; 44 \; (nm) \qquad\qquad\qquad (A.1)$$

where t_{hBN} is the thickness of hBN, measured in nm. Note that this relation is expected to be most accurate at low thicknesses (<50 nm), because thicker flakes were not measured and the *RGS* value is expected to be periodic at larger thicknesses. Also, the slope of the *RGS*-dependence will vary with different optical filters and substrates used. Here, hBN was mechanically-exfoliated with scotch tape onto Si/SiO$_2$ wafers with a 300-nm surface oxide layer. The relation found in equation A.1 is useful to crudely estimate the thickness of hBN, and thus bypass the necessity of an AFM when the knowledge of the precise thicknesses of hBN flakes is not required.

A.2 Statistics of few-layer graphene transport data

In this section, statistics of few-layer graphene transport data at low temperature are shown. In these data, we measure the two-terminal differential conductance $G = dI_D/dV_{SD}^{AC}$, where we apply a 50 μV signal across the source (S) and drain (D) terminals. We measure G at low AC frequencies on the order of 100 Hz. Data are gathered from suspended trilayer- (TLG), tetralayer- (4LG) and pentalayer graphene (5LG) devices, and plotted versus various parameters. We categorize our statistics in two groups: Annealing current density statistics, and bias spectroscopy statistics.

A.2.1 Annealing current density statistics

Current annealing is performed post-fabrication to improve device quality by burning off impurities through Joule heating. We perform current annealing at typical sample temperatures of $T = 1.6$K in a vacuum-pumped cryomagnet. Before and after every annealing cycle, we investigate the back gate response $G(V_{BG})$ by sweeping the back gate voltage V_{BG} by $\sim \pm 6$V, recording the position of the Dirac point in back gate voltage V_{BG}^D, and the electron μ_n and hole μ_p moblities. If the device is insulating or near insulating, we also check the features of $G(V_{SD})$, by measuring G and sweeping a DC source-drain bias voltage V_{SD}, to investigate the presence of an interaction-induced gap at low temperature in the absence of external fields.

In figure A.2, we plot the annealing current density J_A, measured as current per cross-sectional width W in units of mA/μm, versus minimum conductance G_{min} (figure A.2a), half the peak-to-peak distance in $G(V_{SD})$, here, denoted as Δ (figure A.2b), and electron (figure A.2c) and hole mobility (A.2d), respectively. In these plots, red, green, and blue data points correspond to TLG, 4LG and 5LG, respectively. Also, square (triangle) data points have a U- (V-) shaped curve in $G(V_{SD})$, meaning that the square data points have well-defined side-peaks in bias measurements, implying a well-resolved gapped state. As discussed in chapter three, optimal current densities of 0.2-0.4 mA/μm/layer tend to provide the best annealing results.
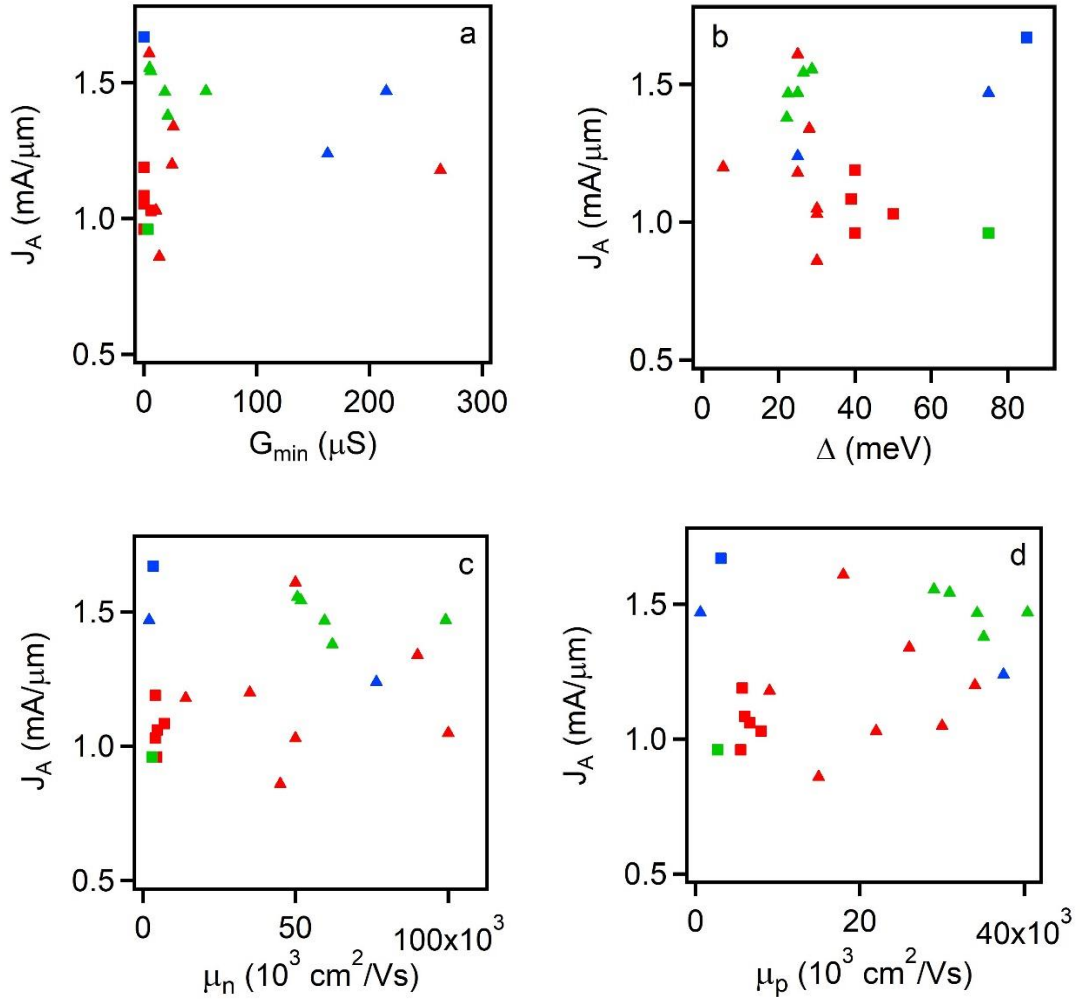
Figure A.2. Annealing current density statistics in suspended few-layer graphene devices: (a) Current density versus minimum conductance, $J_A(G_{min})$. (b) Current density versus peak-to-peak distance in $G(V_{SD})$, $J_A(\Delta)$. (c) Current density versus electron mobility, $J_A(\mu_n)$. (d) Current density versus hole mobility, $J_A(\mu_p)$. Red, green, and blue data points correspond to TLG, 4LG and 5LG, respectively. Square (triangle) data points have U- (V-) shaped curve in $G(V_{SD})$.

In the plots in figure A.2, we note little to no correlation between J_A and G_{min}, Δ, μ_n, and μ_p. In figure A.2a, most of the samples have low minimum conductance, while only a few have $G_{min} > 100$ mS. Although only three 5LG devices were measured, they tend to have high G_{min} and low mobility, indicating that current annealing was not as

successful for them as in TLG and 4LG devices. Also, J_A, in mA/μm, tends to be the largest for 5LG and the smallest for TLG, which is expected, as more layers of graphene can carry a larger annealing current.

A.2.2 Bias spectroscopy statistics

Here, we plot bias spectroscopy results of a large sample of few-layer graphene (FLG) devices in figure A.3, with the same color and shape scheme for the data points as figure A.2. $G_{min}(\Delta)$ is plotted in figure A.3a, and we note that samples with low (high) G_{min} tend to have U- (V-) shaped $G(V_{SD})$ curves. In other words, samples with well-defined side peaks and well-resolved gapped states also have low conductance or are insulating. We observe no clear dependence of G_{min} or Δ with number of layers.

We also observe a trend in the field effect mobility versus half the peak-to-peak distance in bias spectroscopy measurements. In figure A.3b (A.3c), we plot μ_n (μ_p) versus Δ. In both cases for carriers of either negative or positive charge, we observe a trend where devices with lower (higher) mobility have a larger (smaller) peak-to-peak distance in bias spectroscopy measurements. Moreover, we see a resonance peak in the triangular data points with $\Delta \sim 25$ meV, whereas the square data points have $\Delta \sim > 40$ meV. Thus, devices with larger peak-to-peak distances in $G(V_{SD})$ have a well-defined gap and lower mobility. We note that $\mu_n > \mu_p$ for a given device in most cases. The origin of this ambipolar effect is unclear, but it may be somehow related to device fabrication or

current annealing. Again, we do not see any clear dependence of μ_n, μ_p, or Δ with number of layers.
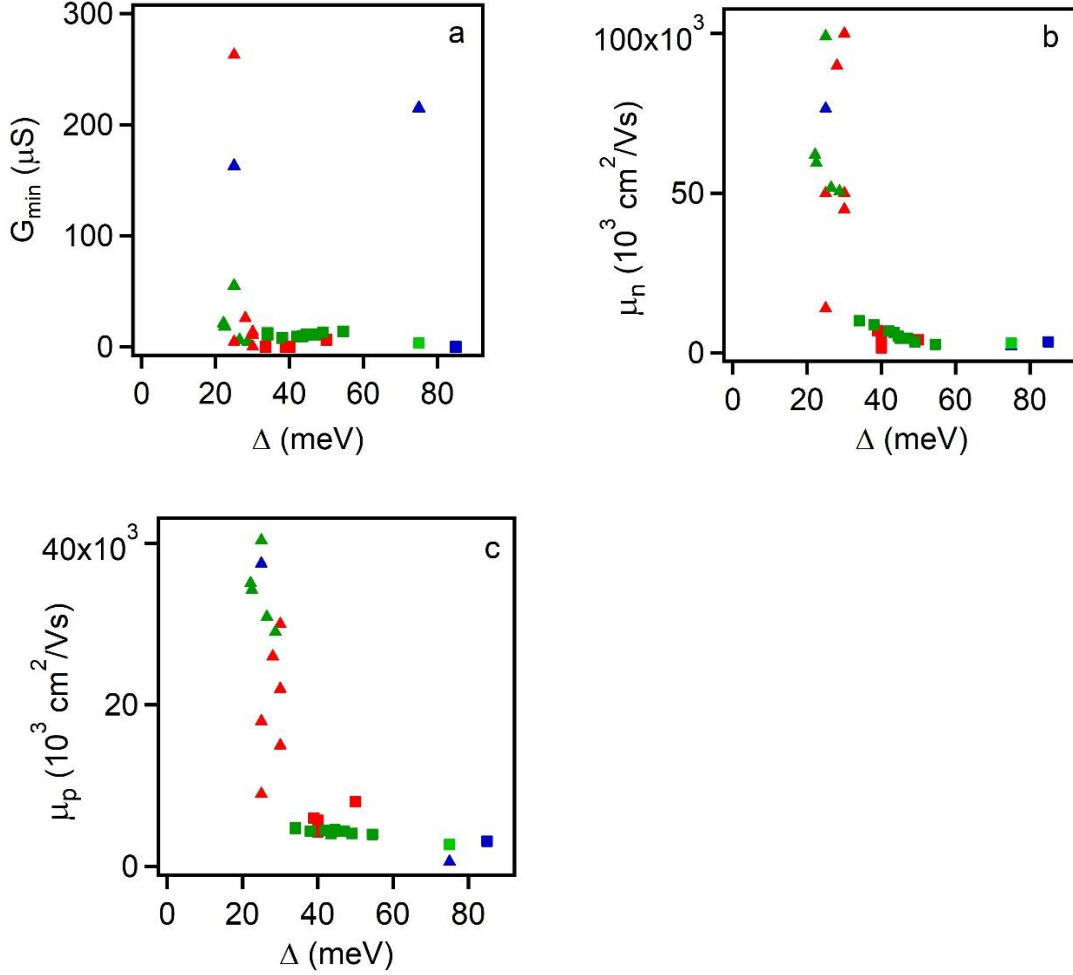

Figure A.3. Bias spectroscopy statistics in suspended few-layer graphene: (a) Minimum conductance versus half the peak-to-peak distance in $G(V_{SD})$, $G_{min}(\Delta)$. (b) Electron mobility versus half the peak-to-peak distance in $G(V_{SD})$, $\mu_n(\Delta)$. (c) Hole mobility versus half the peak-to-peak distance in $G(V_{SD})$, $\mu_p(\Delta)$. Red, green, and blue data points correspond to TLG, 4LG and 5LG, respectively. Square (triangle) data points have U- (V-) shaped curve in $G(V_{SD})$.